EXPERIMENTAL STUDY OF GAS TURBINE BLADE FILM COOLING AND HEAT TRANSFER

A Dissertation

by

DIGANTA PRAKASH NARZARY

Submitted to the Office of Graduate Studies of
Texas A&M University
in partial fulfillment of the requirements for the degree of

DOCTOR OF PHILOSOPHY

August 2009

Major Subject: Mechanical Engineering

EXPERIMENTAL STUDY OF GAS TURBINE BLADE FILM COOLING AND HEAT TRANSFER

A Dissertation

by

DIGANTA PRAKASH NARZARY

Submitted to the Office of Graduate Studies of
Texas A&M University
in partial fulfillment of the requirements for the degree of

DOCTOR OF PHILOSOPHY

Approved by:

Chair of Committee,	Je-Chin Han
Committee Members,	Sai C. Lau
	Gerald L. Morrison
	Hamn Ching Chen
Head of Department,	Dennis O'Neal

August 2009

Major Subject: Mechanical Engineering

ABSTRACT

Experimental Study of Gas Turbine Blade Film Cooling
and Heat Transfer. (August 2009)
Diganta Prakash Narzary, B.Tech., IIT Mumbai, India;
M.S., Arizona State University
Chair of Advisory Committee: Dr. Je-Chin Han

Modern gas turbine engines require higher turbine-entry gas temperature to improve their thermal efficiency and thereby their performance. A major accompanying concern is the heat-up of the turbine components which are already subject to high thermal and mechanical stresses. This heat-up can be reduced by: (i) applying thermal barrier coating (TBC) on the surface, and (ii) providing coolant to the surface by injecting secondary air discharged from the compressor. However, as the bleeding off of compressor discharge air exacts a penalty on engine performance, the cooling functions must be accomplished with the smallest possible secondary air injection. This necessitates a detailed and systematic study of the various flow and geometrical parameters that may have a bearing on the cooling pattern.

In the present study, experiments were performed in three regions of a non-rotating gas turbine blade cascade: blade platform, blade span, and blade tip. The blade platform and blade span studies were carried out on a high pressure turbine rotor blade cascade in medium flow conditions. Film-cooling effectiveness or degree of cooling was assessed in terms of cooling hole geometry, blowing ratio, freestream turbulence, coolant-to-mainstream density ratio, purge flow rate, upstream vortex for blade platform cooling and blowing ratio, and upstream vortex for blade span cooling. The blade tip study was performed in a blow-down flow loop in a transonic flow environment. The degree of cooling was assessed in terms of blowing ratio and tip clearance. Limited heat transfer coefficient measurements were also carried out. Mainstream pressure loss was also measured for blade platform and blade tip film-cooling with the help of pitot-static probes. The pressure sensitive paint (PSP) and temperature sensitive paint (TSP) techniques were used for measuring film-cooling effectiveness whereas for heat transfer coefficient measurement, temperature sensitive paint (TSP) technique was employed.

Results indicated that the blade platform cooling requires a combination of upstream purge flow and downstream discrete film-cooling holes to cool the entire platform. The shaped cooling holes provided wider film coverage and higher film-cooling effectiveness than the cylindrical holes while also creating lesser mainstream pressure losses. Higher coolant-to-mainstream density ratio resulted in higher effectiveness levels from the cooling holes. On the blade span, at any given blowing ratio, the suction side showed better coolant coverage than the pressure side even though the former had two fewer rows of holes. Film-cooling effectiveness increased with blowing ratio on both sides of the blade. Whereas the pressure side effectiveness continued to increase with blowing ratio, the increase in suction side effectiveness slowed down at higher blowing ratios (M=0.9 and 1.2). Upstream wake had a detrimental effect on film coverage. 0% and 25% wake phase positions significantly decreased film-cooling effectiveness magnitude. Comparison between the compound shaped hole and the compound cylindrical hole design showed higher effectiveness values for shaped holes on the suction side. The cylindrical holes performed marginally better in the curved portion of the pressure side. Finally, the concept tip proved to be better than the baseline tip in terms of reducing mainstream flow leakage and mainstream pressure loss. The film-cooling effectiveness on the concept blade increased with increasing blowing ratio and tip gap. However, the film-coverage on the leading tip portion was almost negligible.

ACKNOWLEDGMENTS

I wish to express my gratitude to Dr. J. C. Han for his constant guidance and support throughout the course of my graduate study. I thank Dr. S. C. Lau, Dr. G. L. Morrison, and Dr. H. C. Chen, for having agreed to be on my committee. Their advice and suggestions are greatly appreciated. I also would like to thank my colleagues at Turbine Heat Transfer Laboratory and TURBOLAB for their help and suggestions. My thanks also extend to Mr. Eddie Denk for his help in the machine shop.

Finally, I want to thank my parents, Sri Rameswar Narzary and Smt. Kamini Narzary, my brother Somendu Bikash Narzary, and my sister Tara Narzary, for their continued support and patience.

NOMENCLATURE

C	oxygen concentration
C_D	discharge coefficient
C_x	axial chord length of the rotor blade (8.13 cm)
d	diameter of film cooling hole (mm)
H	cascade height (12.7cm)
I	pixel intensity of an image or momentum ratio of coolant (=M^2/DR)
$\dot{m}_c$	coolant mass flow rate for purge flow (kg/s)
DR	coolant-to-mainstream density ratio
MFR	mass flow ratio of slot purge flow (percentage of mainstream mass flow rate)
M	average blowing ratio for discrete film holes
l	length of the film cooling hole
d	diameter of film cooling hole
Tu	freestream turbulence intensity
u_{RMS}	root mean square velocity
u	averaged local velocity
B	turbulence grid bar width
P	local static pressure (Pa)
PS	abbreviation for “pressure side”
P_t	total pressure (Pa)
P_{O_2}	partial pressure of oxygen (Pa)
S	blade pitch (cm) or Distance between adjacent holes in a hole row (=5.3mm)
SS	abbreviation for “suction side”
SH	showerhead film cooling hole row
ST	stagnation
T	temperature (K)
x	axial distance measured from blade leading edge(cm)
y	pitchwise distance measured from suction side (cm) or distance along blade span measured from hub
z	spanwise distance measure from platform (cm)

V_c	average coolant velocity (m/s)
V_m	mainstream velocity (m/s)
W	molecular weight of gas
η	local film cooling effectiveness
$\overline{\eta}$	laterally averaged film cooling effectiveness
π	total pressure ratio (=$P_{t, ex}/P_{t, in}$)
ρ_c	density of coolant (kg/m^3)
ρ_m	density of mainstream air (kg/m^3)

Subscript

air	mainstream air with air as coolant
blk	image without illumination (black)
c	coolant
f	local film
b	black image
ex	exit of cascade
in	inlet of cascade
m	mainstream
mix	mainstream air with nitrogen as coolant
ref	reference image with no mainstream and coolant flow
r	coolant hole row

TABLE OF CONTENTS

LIST OF FIGURES

Page

LIST OF TABLES

1. INTRODUCTION

1.1 Background

Since the introduction of gas turbine engines in the 1940s, turbine-entry gas temperature has increased from around 900 K to over 1800 K. This increase has improved the turbine efficiency, resulting in improved performance and reduced fuel consumption. While some of the increase in temperature has been made possible through the development of new materials, most has occurred because of improvements in cooling technology. Figure 1.1 shows a typical turbine section cross-section in a gas turbine with cooling and sealing arrangement. As shown, the mainstream gas flows over the turbine vanes and blades, the temperature of the gas usually being well above the melting point of the materials from which the airfoils are made. To keep the

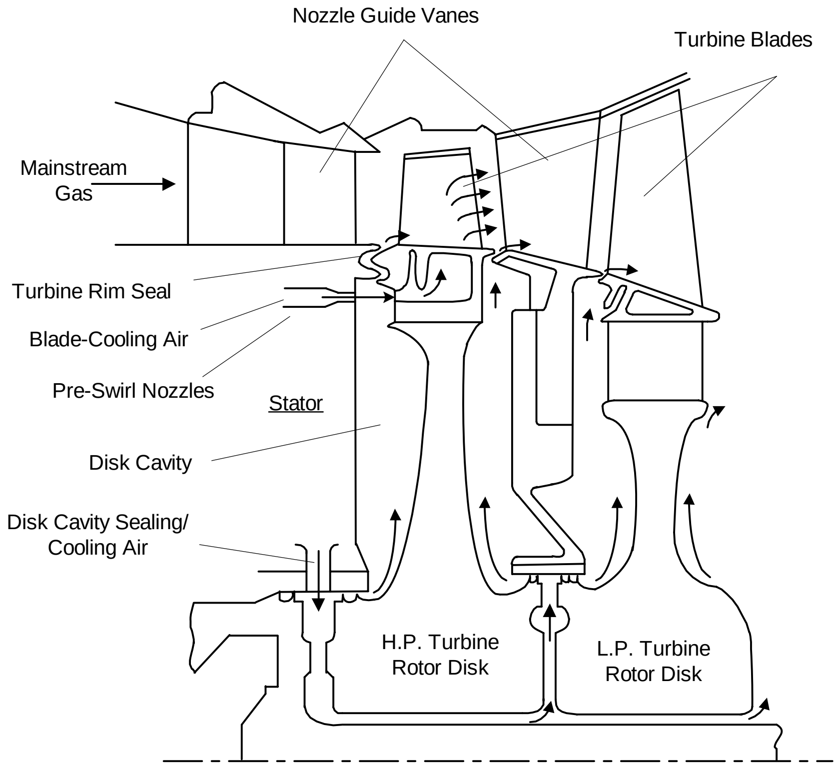

Fig. 1.1 A typical turbine cross-section with sealing and cooling system (by courtesy of Wilson et al., 1995)

This dissertation follows the style of ASME Journal of Turbomachinery.

airfoils safe in such an extreme environment, cooler, high pressure air is injected into the airfoil. The injected coolant travels through a serpentine passage, absorbs heat from the inner walls as it travels, and finally exits from tiny discrete holes and 2-D slots. The discharged coolant, when adequately supplied, forms a thin layer of relatively cooler air on the surface that keeps the hot mainstream air from coming in direct contact with the airfoil body. Between the vane and the blade row is the rim seal that prevents or limits entry of hot mainstream into the cavity formed between the rotor and stator disks. Any transport of the mainstream gas, through the clearance between the rim seals, will lead to overheating of the disks with a consequent reduction in rotor disk life. As such, cooler air is also injected into the cavities, a part or all of this air is ejected back into the mainstream gas path through the clearance between disk rim seals.

A key objective in turbine design is to accomplish the disk cavity sealing and metal cooling functions using the smallest possible amount of cooling air. This is because the bleed-off of compressor air and its subsequent mixing with the mainstream gas flow exact penalties on turbine performance. Attaining the objective requires sound cooling system design as well as optimization of coolant flow supply based on a comprehensive study of the mainstream and coolant flow parameters that are likely to affect the cooling process.

1.2 Overview of the Work

This work is divided into three parts: i) film-cooling effectiveness study on the blade platform, ii) film-cooling effectiveness study on the blade span, and iii) film-cooling effectiveness and heat transfer coefficient study on the blade tip.

In the first part, platform cooling by a combination of purge flow from a stator-rotor seal and discrete-holes was studied. Two different film hole configurations and two different layouts formed a total of four platform designs. The upstream double-toothed stator-rotor seal design remained unchanged througout. The four cooling hole designs were evaluated in terms of film-cooling effectiveness and total mainstream pressure loss. In the first layout, the film cooling holes were lined up in the streamwise direction in two rows and clustered on the pressure side half of the passage. In the second layout, the same number of film holes were divided into four rows and spread out on the platform. The detailed film-cooling effectiveness distributions on the platform were obtained using the conduction-free pressure sensitive paint (PSP) technique. Additional film-cooling effectiveness study was carried out on the platform using temperature sensitive paint (TSP) technique. The parameters chosen were – freestream turbulence intensity, upstream stator-rotor purge flow rate, discrete-hole film-cooling blowing ratio, and coolant-to-mainstream density ratio. Two turbulence intensities of 4.2% and 10.5%; three purge flows between the range of 0.25% and 0.75% of mainstream flow rate; three blowing ratios between 1.0 and 2.0; and three density ratios between 1.1 and 2.1 were investigated. The range of these parameters was chosen to create an engine-like flow environment. The purge flow was supplied via the same stator-rotor seal, whereas the discrete-hole film cooling was accomplished via one of the four platform designs mentioned above. The inlet and the exit Mach numbers were 0.27 and 0.44, respectively. Reynolds number of the mainstream flow was $7.5*10^5$ based on the exit velocity and chord length of the blade.

In the same blade cascade, the effect of laidback, fan-shaped, compound angle cooling holes on film cooling effectiveness was studied on a heavily film-cooled high pressure turbine blade using the PSP technique. This study formed the second of the three part study. The test blade featured four rows of shaped holes on the pressure side and two rows on the suction side. In addition, three rows of cylindrical holes on the leading edge captured the effect of showerhead coolant ejection. Four average blowing ratios ranging from 0.3 to 1.2 formed the key parameter in this study. The presence of wake due to upstream vane trailing edge was studied by placing a set of equally spaced metal rods in front of the blades. To simulate a progressing wake in the cascade, the wake rod set was shifted and stationed at four different positions with respect to the blade pitch in the pitch-wise direction. The free stream Reynolds number based on the axial chord length and the exit velocity was 750,000 and the inlet and the exit Mach numbers were 0.27 and 0.44, respectively. Freestream turbulence intensity level measured upstream of the blade was 4.2%.

The third and final part of this thesis deals with the study of film-cooling effectiveness, heat transfer coefficient, and total pressure loss measurements of a high pressure gas turbine blade tip in transonic flow conditions. Two blade tip designs- one with a typical cut-back squealer rim and another with a suction side rail (concept blade) - were compared side-by-side for their mainstream total pressure loss and tip leakage characteristics at three different tip clearances of 0.9%, 1.6%, and 2.3% of the blade span. For the mainstream pressure loss measurements, the exit total pressure was measured in a 2-dimensional plane by vertically traversing a series of eight pitot-static probes stationed at $0.75C_{ax}$ distance downstream of the blade trailing edges. The tip leakage was estimated based on a simple orifice flow model wherein an assumed value of discharge coefficient was used. The film-cooling effectiveness measurements were performed for the concept blade tip only. The concept blade tip featured 30 holes on the tip, 24 on the pressure side near tip, 6 on the suction side, and 3 on the leading edge. The heat transfer measurements were performed without any coolant supply. PSP method was used for film-cooling effectiveness whereas TSP technique was used for heat transfer coefficient measurements. The tests were carried out in a 3-blade blow-down cascade that maintains steady flow for about 30 seconds. The inlet and the exit mainstream flow Mach numbers were 0.29 and 0.75, respectively. The inlet total pressure to exit static pressure ratio was 1.49 and the inlet mainstream average turbulent intensity was 13.5%.

2. TURBINE BLADE PLATFORM FILM-COOLING

2.1 Introduction

Higher turbine inlet temperatures and flatter temperature profiles have made platform cooling a crucial aspect of the overall turbine cooling design. Platform cooling makes use of a combination of stator-rotor purge flow and discrete hole film-cooling. Among the variety of cooling hole configurations available today, the four most commonly used configurations are: cylindrical holes, laterally-diffused (or fan-shaped) holes, forward-diffused (or laidback) holes, and laterally- and forward-diffused holes. Figure 2.1 shows the schematic of the four cooling hole configurations. The latter three designs, termed as ‘shaped holes’, have expanded or diffused exit to help reduce jet momentum and therefore prevent lift-off.

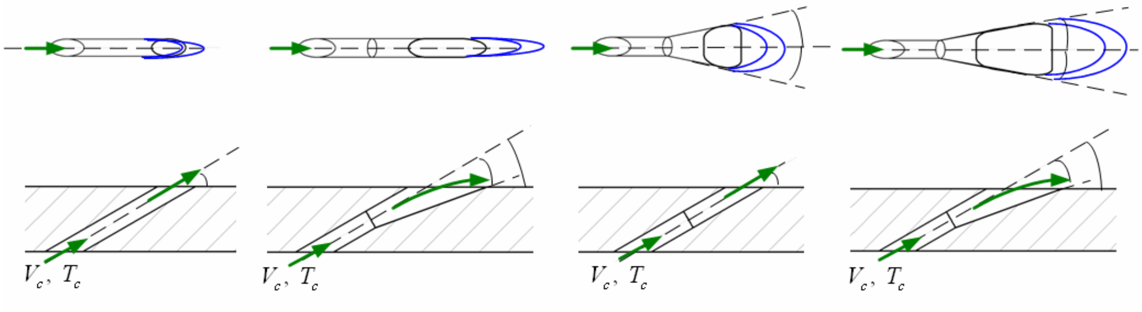

Cylindrical hole Laidback hole Fanshape hole Laidback fanshape hole

Fig. 2.1 Various film-cooling hole configurations

The cooling process on the platform is rather difficult because of the presence of 3-dimensional flow structures in the blade passage. The flow structures and their effects on heat transfer and film-cooling are described in the works of Langston [1, 2, 3], Chyu [4], and Simon and Piggush [5]. Their works show the development of the small scale horseshoe vortex into a much larger passage vortex as it migrates from the blade leading edge to the suction side of the neighboring blade. Several small scale corner vortices are also formed near the intersection of the blade surface and the platform.

A common way of cooling the platform surface is by discharging coolant through discrete holes. Many researchers have investigated film-cooling on endwalls with discrete cylindrical holes. Takieshi et al. [6] obtained heat transfer and film-effectiveness distributions on a vane endwall with film holes placed at three locations in the passage. Harasgama and Burton [7] used film-cooling near the leading edge, just inside the passage, with the film-cooling holes located along an iso-Mach line. The film-cooling configuration used by Jabbari et al. [8] consisted of discrete holes placed on the downstream half of the passage. Friedrichs et al. [9, 10, 11] studied film-cooling effectiveness and aerodynamic loss on a fully film-cooled endwall. The above studies found that the film-cooling was strongly affected by endwall secondary flows. The cross-flow transported the coolant from the pressure side to the suction side of the passage. Coolant was prone to "lift-off" when film holes were located on the separation line of the secondary flow. It was difficult to cool the leading portion of the endwall by discrete holes because of the roll-up of the horseshoe vortex.

Coolant is also supplied through the gap between the vane and the blade row. The coolant supplied in this fashion prevents hot mainstream gas from entering the disk cavity and provides some cooling to the front platform region in the process. An early study by Blair [12] showed that the film-cooling effectiveness for upstream slot ejection varied greatly through the passage due to the secondary flows. Many researchers, including Granser and Schulenberg [13], Roy et al. [14], Burd et al. [15] and Oke et al. [16, 17], Zhang and Jaiswal [18], and Zhang and Moon [19] have documented the characteristic of slot cooling on endwalls. These studies showed that besides cooling the hard to cool areas such as the blade leading edge, upstream slot coolant reduced the strength of secondary flows in the passage by increasing the momentum of the boundary layer of the incoming mainstream flow. Wright et al. [20] on a low-speed cascade and Gao et al. [21] on a high-speed cascade used delta-wings to study the effect of upstream vane passage vortex on purge flow cooling. Both studies showed the highly detrimental effect of the delta-wing generated vortex on purge flow cooling. Suryanarayanan et al. [22] investigated platform slot purge flow cooling in a three-stage turbine rotating facility. They found that the stator-rotor interaction also had a significant impact on the platform film-cooling effectiveness.

In real practice, the platform is cooled by both upstream slot and discrete-hole film-cooling. Nicklas [23] used three rows of film-cooling holes in the front third of the endwall in addition to a slot. He found that the downstream passage and the pressure side corner were hard to cool with such an arrangement as the passage vortex sweeps away the coolant. In the design of Wright et al. [24], the film holes were placed close to the throat region of the blade platform. The entire platform was cooled but at the expense of a large amount of coolant. Gao et al. [25] used the combined cooling method to investigate four different discrete-hole layouts: two and four rows of cylindrical and shaped holes. Shaped holes displayed the best film-cooling and aerodynamic performance. The two and four row layouts did not show significant difference in the laterally-averaged effectiveness. Suryanarayanan et al. [26] studied combined film cooling in the same rotating facility as used in [22]. They found that the film-cooling effectiveness increased with increasing purge flow rate and rotation speed. For the downstream discrete-hole film-cooling, the local blowing ratio of 1.0 offered the best film coverage and effectiveness level.

Majority of the work on film-cooling has been implemented with coolant-to-mainstream density ratio close to 1.0. This is far from the actual density ratio of nearly 2.0 that is witnessed in real turbines by virtue of the temperature difference between the coolant and the hot mainstream. Many early studies were carried out on flat plates with simple-angled holes. Pederson et al. [27] demonstrated the strong dependence of film effectiveness when the density ratio was varied from 0.75 to 4.17 on a flat plate with 35 deg inclined holes. Sinha et al. [28] used a similar cooling hole geometry and a density ratio ranging between 1.2 and 2.0. They concluded that at low blowing rates, effectiveness scales well with the mass flux ratio and at higher blowing rates, the effectiveness scales well with the momentum flux ratio. In both the above studies, it was found that the maximum adiabatic effectiveness increased with increasing density ratio. Ethridge et al. [29] conducted experiments on a vane suction side using a low and a high density ratio coolant. They concluded that the effectiveness from holes located on a strong curvature suction side was much higher than holes with a similar injection angle on a flat plate. Over a blade surface, Ekkad et al. [30] found optimum blowing ratios of 0.8 and 1.2 with air and CO_2 as coolants, respectively.

Platform cooling is also influenced by the level of turbulence in the incoming mainstream flow, which could vary depending on combustor geometry. Numerous studies have been conducted on flat plates to establish this. Kadotani and Goldstein [31], Jumper et al. [32], and Bons et al. [33] found that the film effectiveness reduces under elevated turbulence levels at low and moderate blowing ratios but improves at high blowing ratios due to coolant dispersion. In all of the above studies, the turbulence intensity was within a range of 0.3%-20.6% and coolant-to-mainstream density ratio was around 1.0. Schmidt and Bogard [34] also made similar observation with high coolant-to-mainstream density ratio of 2.0. The degree of influence of turbulence intensity on effectiveness varies with the cooling hole geometry. This has been verified by Burd et al. [35] who concluded that holes with smaller L/D ratios are more prone to turbulence levels than those with larger L/D ratios. Saumweber et al. [36] found that unlike cylindrical holes, shaped holes do not show improved effectiveness at elevated turbulence levels.

In the present study, a high pressure turbine rotor blade platform was used to investigate film-cooling effectiveness by independently varying four critical parameters – freestream turbulence level, purge flow rate, blowing ratio, and coolant-to-mainstream density ratio; each within a range that is typical of real engine operating condition. Past studies on this cascade involved film-cooling studies using pressure sensitive paint (PSP) technique with density ratio close to 1.0 and low freestream turbulence intensity of 4.2%. PSP technique is, however, limited to film-cooling effectiveness measurements only. Temperature sensitive paint (TSP) technique, on the other hand, is applicable to both film-cooling and heat transfer measurements. Since the current work is part of a two stage study of film-cooling and heat transfer coefficient, TSP technique was adopted over PSP. Before employing this technique, a sample test (Tu=4.2%, MFR=0.75%, M=0, and DR=1.0) was performed to determine its suitability as a tool for measuring adiabatic film-cooling effectiveness. The data was compared with the PSP test data carried out under the same experimental conditions. Both results showed reasonable agreement with each other.

2.2 Experimental Setup

A five-blade linear cascade was used for this study. Figure 2.2(a) shows the experimental facility consisting of the cascade, coolant loop, and the data acquisition system. A schematic of the cascade in Fig. 2.2(b) shows the test platform with cooling holes and the location of the purge slot with respect to the platform. The mainstream flow was supplied by a centrifugal compressor, powered by a 450hp electric motor. The compressor is rated for a maximum pressure differential of 55kPa and a volume flow rate of 6.2m^3/s. The volume flow rate was regulated by a frequency controller with an operational range of 0 to 60Hz. A honeycomb mesh, of length, 7.62cm and cell size, 1.27cm, was placed 1.78m (or 22*C_x) upstream of the blades to ensure uniform inlet flow condition. Downstream flow periodicity within 2% was achieved by adjusting the cascade tailboards.

For mainstream flow with elevated turbulence level, the upstream cascade flange was replaced by a turbulence grid that also duplicated as a flange.

A labyrinth-like seal, typical of a stator-rotor seal found in gas turbine engines**,** was used for upstream platform cooling. The seal was grown from Accura 55 resin by stereo-lithography (SLA) process. SLA process allows complex geometries to be created in real quick time and at a much lower price. Typical SLA resins have a thermal conductivity of around 0.2W/m ^{o}K. Two individual saw-toothed SLA pieces were placed side-by-side to give the seal its zigzag shape, fig. 2.3. The downstream half of the seal met the platform at an angle of 20^o. The seal covered two passages of the cascade. A coolant plenum was constructed underneath the seal. Coolant entered the plenum from the two narrow sides and exited the seal after traveling through a metal screen. Additional platform film-cooling was provided by discrete holes. Figure 2.4 shows the hole

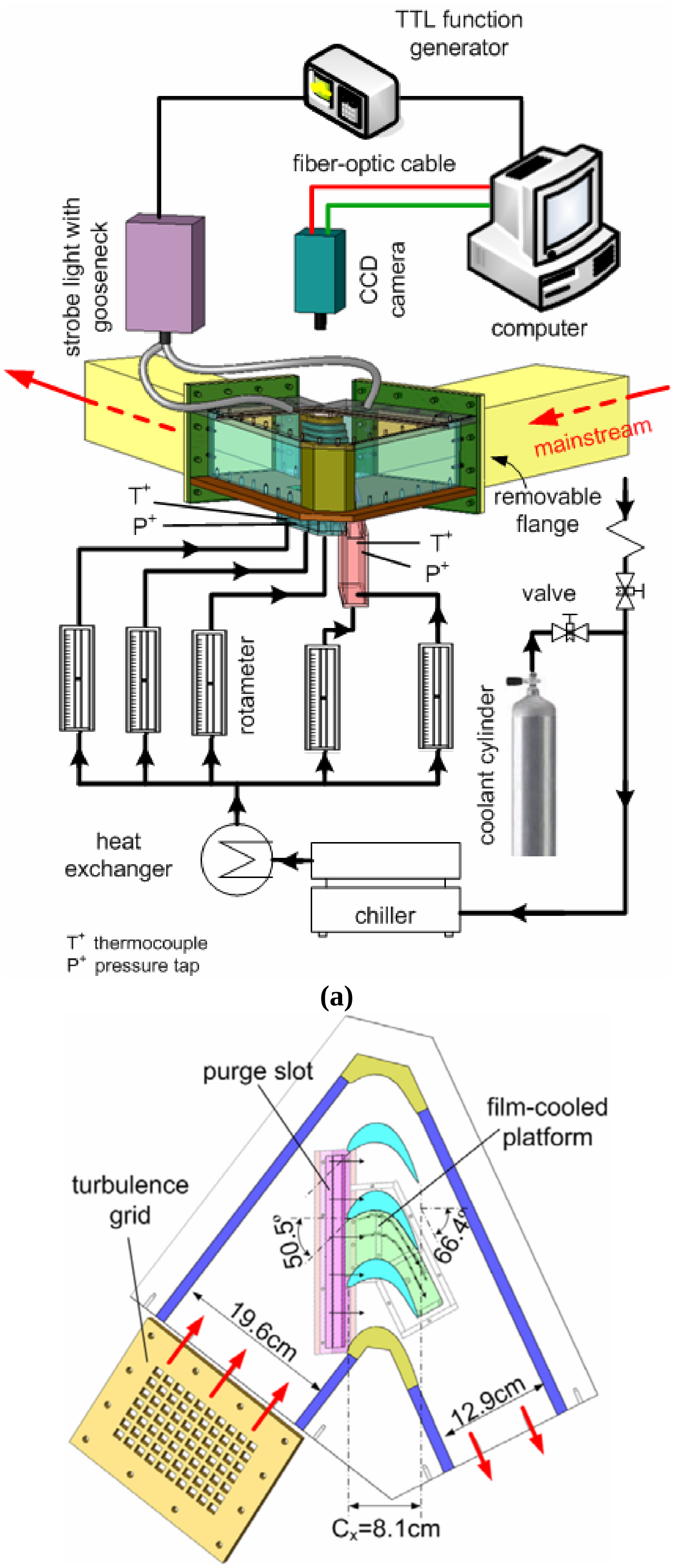

(a)

(b)

Fig. 2.2 Schematic of (a) Experimental facility (b) Linear cascade

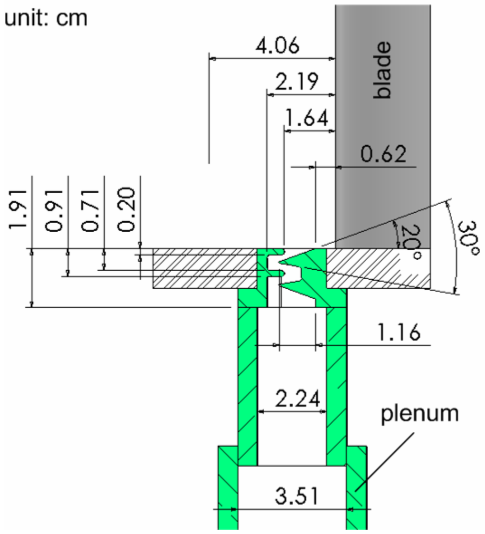

Fig. 2.3 Schematic of purge slot

configurations. The film cooling holes were lined up in the streamwise direction (inline design). Past studies have confirmed that the passage cross flow sweeps the film coolant from pressure side to suction side. Studies on the flat plates show that coolant from compound angle holes covers wider area due to jet deflection. The inline design was however preferred because the passage cross flow would assist in turning the coolant jet to a certain extent. The film-cooling holes were arranged on the platform with two layouts. In one layout, the film cooling holes were divided into two rows and clustered on the pressure side half of the passage. In the second layout, the film-cooling holes were divided into fours rows and loosely distributed on the entire platform. With the two film-hole shapes and two layouts, four film-hole configurations were studied. Among the four configurations, Configs. A and B had cylindrical holes, whereas C and D had laidback fan-shaped holes. Configs. A and C were arranged in two rows, whereas B and D were arranged in four rows. Sixteen film holes, inclined 30º to the platform surface, were used in all configurations. The cylindrical holes had a diameter (d) of 1.588mm with a hole length of 8d. The laidback fan-shaped holes featured a lateral expansion of 10º from the hole axis and forward expansion of 5º into the platform surface. The hole diameter in metering part (cylindrical part) of the shaped holes was the same as that for the cylindrical holes. The expansion started at 4d, resulting in a cross-sectional area ratio of 3.85 between the hole exit and hole inlet. For the two-row designs (Config. A and C), one row was located along the mid-passage line and the other row was located along a curve 6.35mm offset from the pressure side of the blade surface. There were 8 holes in each row. The first hole in each row was located at an axial location of x/C_x=0.36. The

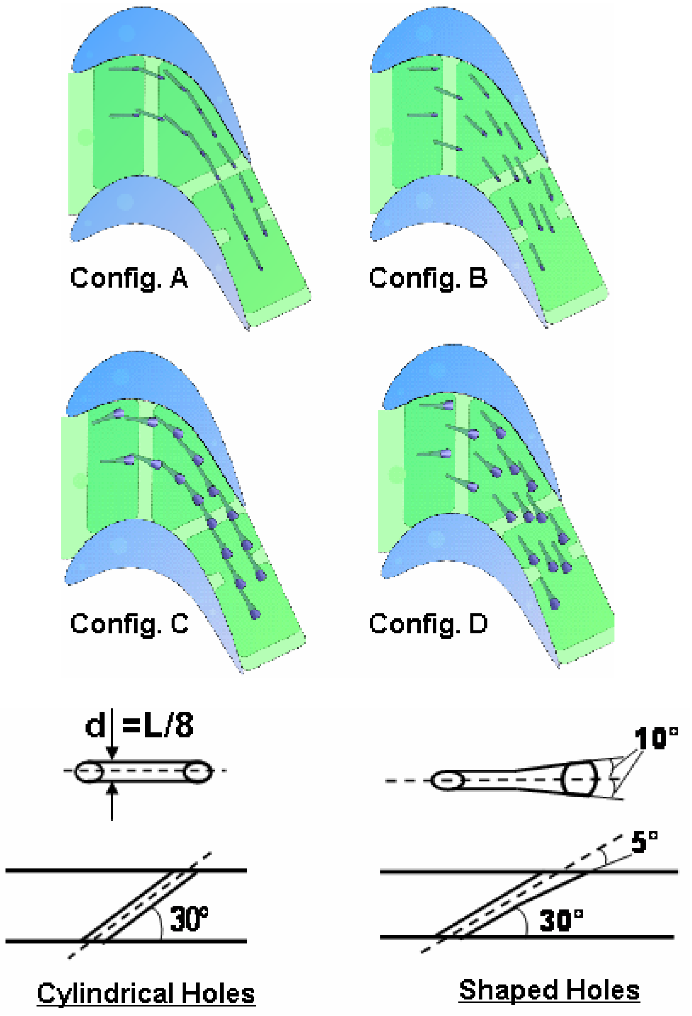

Fig. 2.4 Discrete cooling hole configurations

hole to hole spacing along the curve was around 4d. The four-row designs, Config. B and D, were achieved by shifting the alternative holes in Config. A and C, respectively, in the transverse direction towards the suction side of the passage.

Since the platform surface static pressure varies in the streamwise as well as the transverse direction, the coolant delivery is likely to vary from hole-to-hole if a single large plenum is used. In order to minimize this variation, three separate plenums were fitted underneath the platform in the streamwise direction. The upstream-most plenum supplied coolant to the first four holes, middle plenum to the next seven holes, and the downstream plenum to the remaining five holes. Metal screens were installed in each plenum for uniform coolant flow distribution. For film-cooling studies using TSP method, the coolant was cooled to the desired temperature by a

NESLAB Merlin recirculating chiller. The operating temperature range of the chiller is 258K to 308K with a temperature stability of ±273.15K.

As shown in Table 2.1, a total of 8 experiments were performed to study the parametric effects of freestream turbulence (Tu), purge flow rate (MFR), blowing ratio (M), and density ratio (DR) on platform effectiveness. The freestream turbulence intensity was measured at a distance 0.5C_x upstream of the blade row by traversing a hot-film probe from the center to the top of the channel. The turbulence intensity ($Tu = u_{RMS}/u$) measured at the centerline was 1.75% and the average turbulence intensity over the half-channel height was 4.2%. This turbulence intensity served as the low turbulence case in this study. To achieve higher freestream turbulence, a grid was installed 2.5C_{ax} distance upstream of the blade row. The grid had porosity of 50% and bar width (B) of 0.635cm. The centerline turbulence intensity was 8.8% and the average over the half-channel height was 10.5%. The distance between the grid and the hot-film probe was, x=26*B. Using the correlation (Tu=1.12*(x/B)$^{-5/7}$) proposed by Baines and Peterson [39] for a square grid, the intensity decay was calculated to be 10.9%, which is nearly equal to the measured average value. The comparison between the two turbulence intensity profiles is presented in Fig. 2.5(a). The average length scales ($\square_x$), calculated based on the autocorrelation of the fluctuating component of velocity, were 5.85cm and 0.56cm for the low and high turbulence level cases, respectively. The velocity profile with and without grid was also measured at the same upstream distance from the blade using a pitot-static probe. The comparison is shown in Fig. 2.5(b).

Table 2.1 Summary of experimental conditions

Expt.	M [I]	Tu	DR	MFR [I]
1	1.0 [0.526]	4.2%	1.8	0.50% [0.023]
2	1.0 [0.526]	10.5%	1.8	0.50% [0.023]
3	1.0 [0.526]	10.5%	1.8	0.25% [0.006]
4	1.0 [0.526]	10.5%	1.8	0.75% [0.052]
5	1.5 [1.180]	10.5%	1.8	0.50% [0.023]
6	2.0 [2.100]	10.5%	1.8	0.50% [0.023]
7	1.0 [0.877]	10.5%	1.1	0.50% [0.039]
8	1.0 [0.478]	10.5%	2.1	0.50% [0.021]

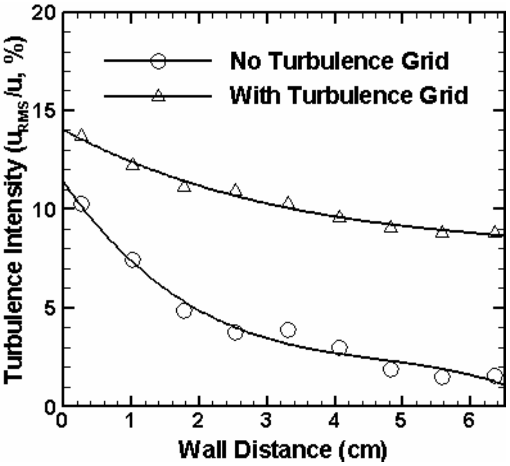

(a)

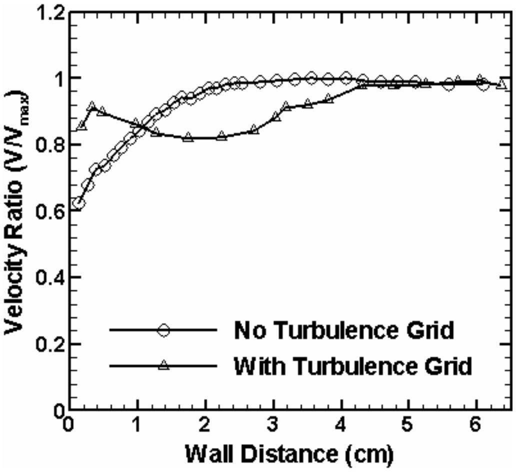

(b)

Fig. 2.5 (a) Turbulence intensity and (b) velocity profiles at the inlet of the cascade with and without the turbulence grid

Three purge flow rates were selected for this study – 0.25%, 0.5%, and 0.75% of the mainstream flow. The velocity of the mainstream flow averaged over the complete span was used to calculate the mainstream mass flow rate.

Three average blowing ratios (M) were examined for the film holes–1.0, 1.5 and 2.0. The average blowing ratio is defined as $M=(\rho_c V_c)/(\rho_m V_m)$. The local mainstream velocity at the film hole location is used for V_m. V_m is obtained from the pressure ratio, P/P_t, where P is the local static pressure (previously measured by PSP) and P_t is the inlet total pressure (measured by Pitot-static probe). V_c is easily calculated from the knowledge of coolant flow rate and number of holes.

To investigate the density ratio (DR) effect, chilled air and two foreign gases– industrial grade CO_2, and a mixture of SF6 (20% by wt.) and argon (80% by wt.) served as coolants. With mainstream air density of 1.05 kg/m^3 (at 333K and 1.3 psig), coolant-to-mainstream density ratios of 1.1, 1.8, and 2.1 were obtained with the above coolants. A constant temperature difference between the mainstream and the coolant was maintained as far as possible to keep the errors due to conduction to a minimum.

2.3 Pressure Measurement on Platform and Local Blowing Ratio Distributions

The pressure and Mach number distributions on the platform are shown in Fig. 2.6. The pressure distribution is represented by the ratio of local static pressure and inlet total pressure. The local static pressure was measured by PSP while the inlet total pressure was measured by a Pitot tube placed upstream of the blade. Eleven wall pressure taps were machined on the platform

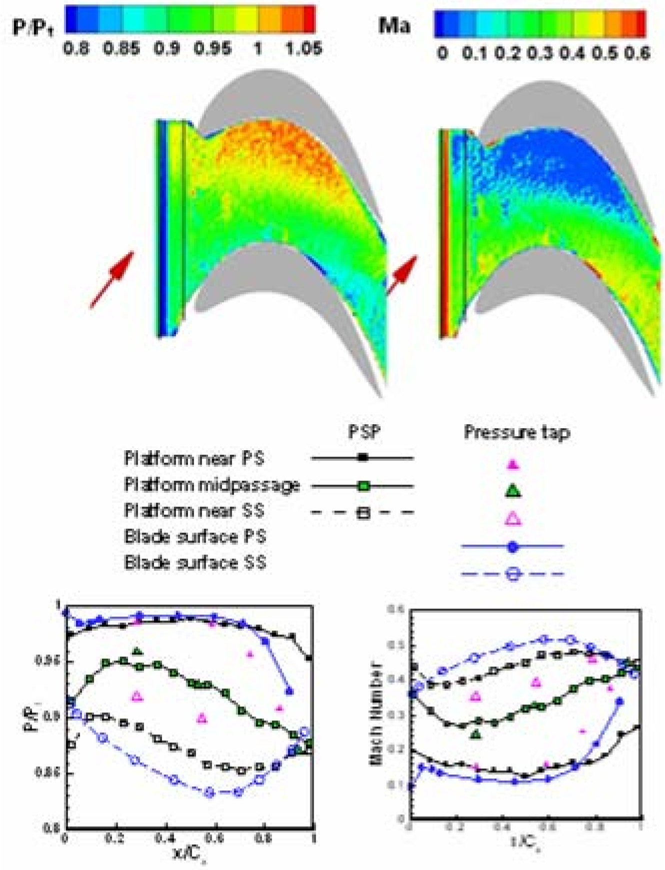

(a) Pressure Distribution (b) Mach number distribution

Fig. 2.6 Pressure and Mach number distribution without coolant injection roughly lined up along three equally spaced streamlines to verify the PSP data. One streamline was offset from the blade pressure side by 10% of pitch distance; the other was offset from the suction side by 10%. The third streamline followed the mid-passage. The pressure and Mach number data obtained from PSP measurement were extracted from the three streamlines and compared with the pressure tap data. Pressure distribution along the midspan of the blade surface, measured by pressure taps, is also presented for comparison. There was no surprise in the contour plot which showed higher static pressure near the pressure side than near the suction side. This pressure differential is the driving force for turbine work as well as the passage cross flow migration. The pressure gradually decreased from the leading to the trailing edge as the mainstream flow accelerated. It can be seen from the line plots that the PSP data matched well with pressure tap data; the maximum deviation between PSP data and pressure tap data was less than 6%. Near the pressure side, the pressure on the platform was very close to the pressure on the blade midspan. However, near the suction side, the pressure on platform was higher than that on the blade midspan. This results in a reduced driving force near the platform. It can be seen from Fig. 2.6 (b) that the velocity on the platform near the suction side was lower than the freestream velocity. The non-uniform platform pressure distribution determines to a large extent the coolant discharge from the slot and the discrete holes. The local coolant flow was determined based on the pressure differential between the plenum total pressure and the platform surface static pressure.

The purge flow distribution, discussed by Gao et al. [21], is shown in Fig. 2.7. The static pressure over the purge slot is higher on the pressure side of the passage compared to that on the suction side. The higher pressure near the pressure side of the passage makes it difficult for the coolant to exit from this side. Detailed discussion on the purge flow distribution can be found in ref. [21]. The local blowing ratio for the discrete holes is defined as $M_{local} = \rho_c V_{c,local}/\rho_m V_m$. Same as in the definition of M, V_m is the local mainstream velocity over the film cooling holes, whereas $V_{c,local}$ is the actual coolant velocity from the film cooling hole. To obtain the actual coolant mass flow rate from each hole, the discharge coefficients C_D was calculated using the following equation:

$$C_D = \dot{m}_{hole} \Bigg/ \left(\frac{\pi}{4}d^2\right)\left(P_{t,cav}\left(\frac{P}{P_{t,cav}}\right)^{\frac{(\gamma+1)}{2\gamma}}\right)\sqrt{\frac{2\gamma}{(\gamma-1)RT_c}\left(\left(\frac{P_{t,cav}}{P}\right)^{\frac{(\gamma-1)}{\gamma}}-1\right)} \tag{1}$$

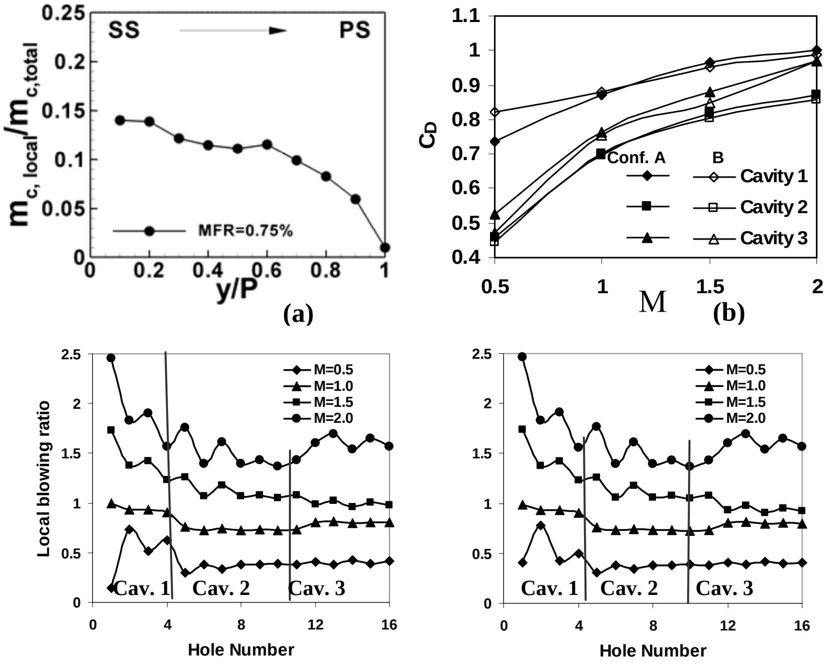

(a) (b)

(c) (d)

Fig. 2.7 (a) Local coolant mass flow rate distribution along the purge slot [29] (b) discharge coefficient distribution (c) Local blowing ratio distribution for Config. A, (d) Local blowing ratio distribution for Config. B

The total pressure inside the coolant plenum $P_{t,cav}$ was measured with pressure taps instrumented on the plenum walls. The discharge coefficient C_D was assumed to be constant for all holes in the cavity for a given average blowing ratio *M*. It should be noted that the constant assumption of C_D may not be true as C_D depends on not only the geometry but also external and internal flow conditions. It was assumed that the deviation in the discharge coefficients from hole to hole was not significant and hence an average value could be used without introducing a significant error. Once C_D for a given *M* was determined, the coolant velocity from each hole was calculated and the local blowing ratio for the hole was computed. It can be seen from Fig. 2.7 (b) that the discharge coefficients increased with M, but the gradient gradually reduced. The values of C_D were about the same for Config. A and B at a given M. As shown in Fig. 2.7(c) and 2.7(d), the local blowing ratio distribution in the first cavity had larger variation than the other two. The local blowing ratios for the holes fed from plenums 2 or cavity 3 were less dispersed. It was also found that the difference in local blowing ratios between Config. A and Config. B was small.

2.4 Film-Cooling Effectiveness Results using PSP

Film-cooling effectiveness measurements were performed for the four platform designs. As stated earlier, a typical coolant mass flow ratio (MFR=0.75%) was chosen for the slot purge flow, while the average blowing ratios for the downstream discrete holes varied from M=0.5~2.0. Before considering the realistic cooling schemes of combined purge flow cooling and discrete-hole film cooling, the isolated effects from discrete holes are shown first. Figure 2.8 shows the film-cooling effectiveness distribution for Config. A and C. Some common features of platform film-cooling were observed irrespective of hole shape. It is clear that the coolant is deflected to the suction side of passage by the cross flow within the passage. At higher blowing ratios, the jet momentum increased, resulting in less jet deflection. Due to this deflection, the corner region between the holes and the blade root on the pressure side remained unprotected. The coolant accumulation from upstream holes near the trailing edge was evident as well. At M=0.5, the pressure inside the plenum chamber was lower than the external mainstream pressure around holes 1, 3 and 5, thereby making it impossible for coolant to escape out of these holes. In fact, the ingestion of mainstream air could have occurred through these holes. On the other hand, more coolant ejected from holes 2 and 4 that resulted in higher local blowing ratios for these two holes.

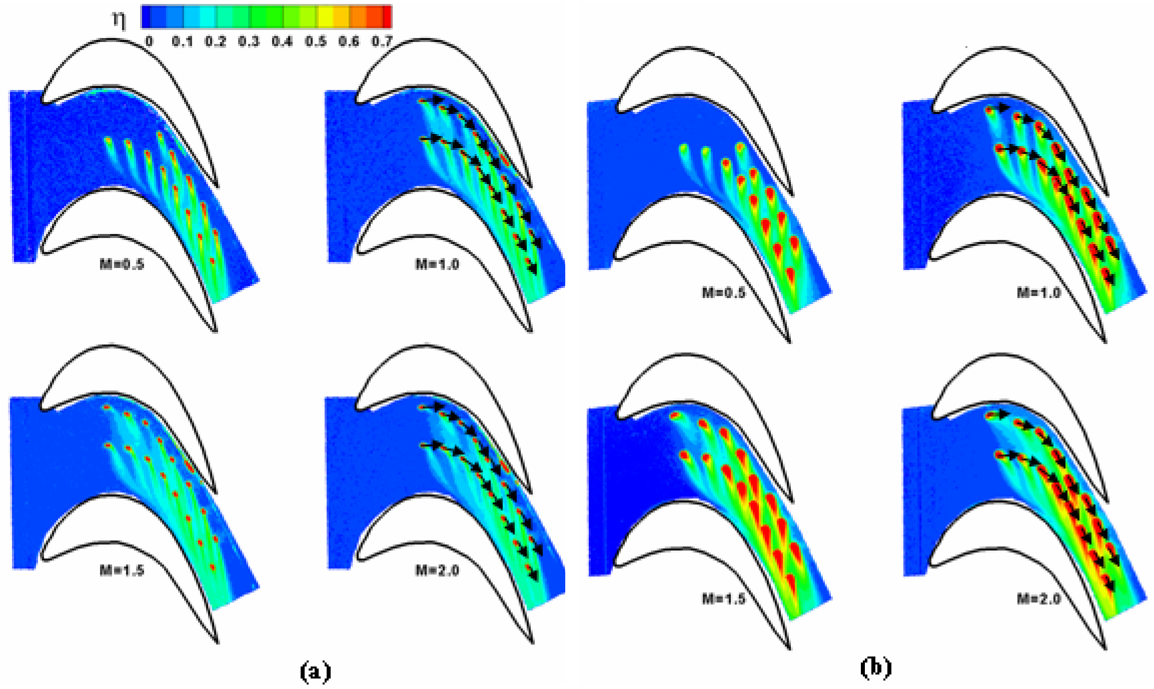

Fig. 2.8 Film cooling effectiveness distribution on platform with discrete holes (a) Config. A , (b) Config. C

Increased amount of coolant from holes 2 and 4 might result in jet lift-off and mixing with the mainstream. It should be noted that the effectiveness reduction from holes 2 and 4 could be caused by the mixing between ingested air (from holes 1, 3, 5) and coolant inside the cavity. Comparing Fig. 2.8(a) and (b), it can be seen that the shaped holes offered larger film coverage and higher effectiveness level. The best film-cooling effectiveness for cylindrical holes was obtained at M=1.0. Further increase of M (M=1.5 and 2.0) resulted in jet penetration into the mainstream and reduction in effectiveness level. For the shaped holes, the film effectiveness increased with average blowing ratio. The enlarged hole breakout area of shaped holes helped reduce jet momentum and so the coolant stayed attached to the surface. In addition, shaped holes produced wider trace and thereby better coolant coverage.

The previous study, ref. [29], showed a large area of the passage that was left unprotected when the platform was cooled by upstream purge flow cooling only. By having discrete cooling holes placed strategically in the passage, majority of the remaining area could be cooled as well. Figures 2.9-2.12 shows the detailed film cooling distributions for the cases of combined purge flow cooling with discrete-hole film cooling.

Figure 2.9 shows the film effectiveness contour for Config. A. It appears that because of the sweeping of purge flow by the passage vortex almost immediately as it emerged from the slot, the upstream and downstream cooling schemes behave independent of the other, although in reality the downstream cooling to a certain extent is a function of the upstream flow. Nevertheless, it is worth investigating if the isolated effect from the purge flow and discrete hole film cooling could simply be superimposed to achieve film effectiveness similar to the combined film-cooling scheme. As with the discrete hole film cooling case, the best effectiveness for this configuration was obtained at M=1.0. Further increase in M led to jet lift-off. The accumulation of coolant from upstream holes resulted in better film-cooling effectiveness in the downstream region. A much better film coverage could have been obtained if one additional hole was added upstream of holes 1 and 2.

Figure 2.10 shows the film effectiveness contours for Config. B. The film-cooling holes were widely distributed over the platform surface with this configuration. In terms of film coverage, Config. B had slightly less coverage than A. Because half the number of holes in Config. A were shifted to the suction side, the jet deflection caused a slightly larger uncovered area near the pressure side half of the passage. Due to this re-arrangement of the holes, the local blowing ratio of each hole was also different and so was the effectiveness. On the whole, the film-cooling effectiveness levels for the two configurations (A and B) were very comparable. The effect of blowing ratio on film-cooling effectiveness also followed the same line.

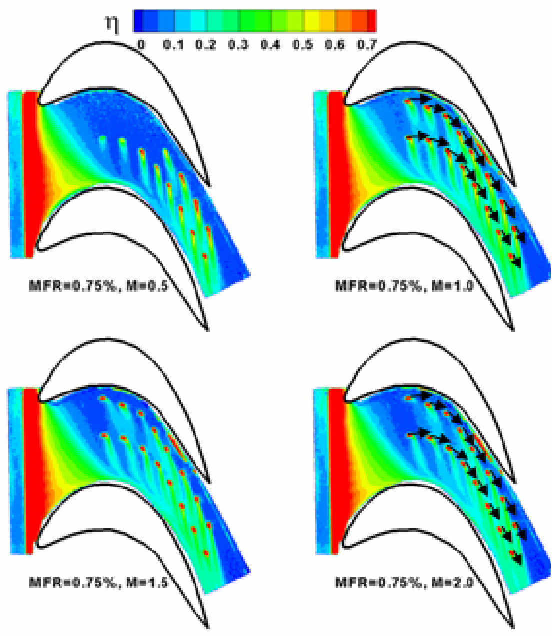

Fig. 2.9 Film cooling effectiveness on platform with combined slot film cooling and discrete-hole film cooling (Config. A)

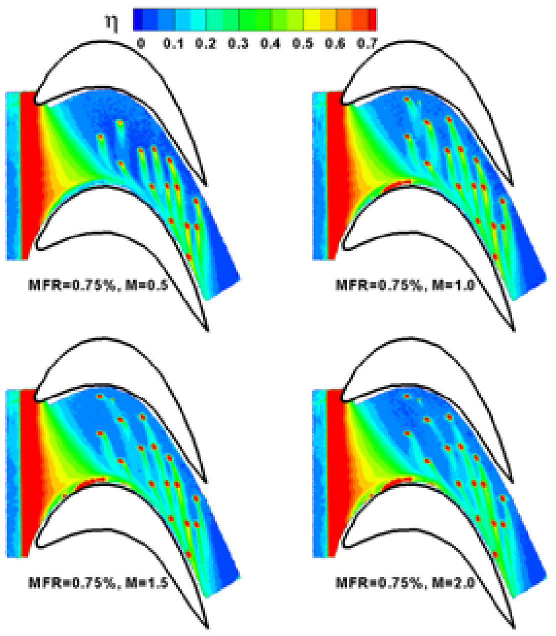

Fig. 2.10 Film cooling effectiveness on platform with combined slot film cooling and discrete-hole film cooling (Config. B)

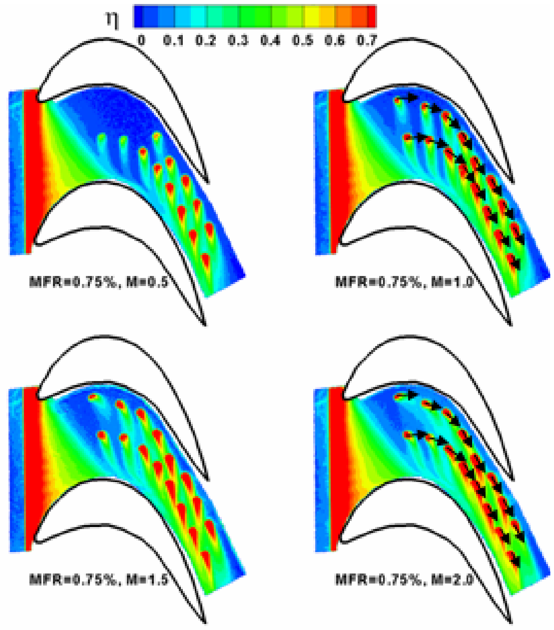

Fig. 2.11 Film cooling effectiveness on platform with combined slot film cooling and discrete-hole film cooling (Config. C)

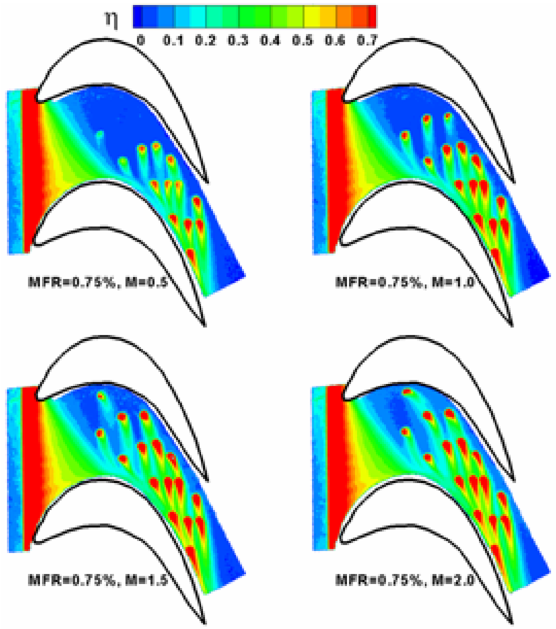

Fig. 2.12 Film cooling effectiveness on platform with combined slot film cooling and discrete-hole film cooling (Config. D)

Figure 2.11 shows the film cooling effectiveness for Config. C. The film coverage and film effectiveness level for Config. C showed improvement over A, particularly at higher average blowing ratios. The film-cooling characteristics seen in Fig. 22(b) were again observed in this figure as well. The film-cooling effectiveness increased with blowing ratio.

Figure 2.12 shows the film effectiveness for Config. D. The film coverage showed slight reduction from C. Close to the suction surface of the passage, the local effectiveness increased. The film effectiveness from the four rows of film holes were not as evenly distributed on the platform as was in Config. C. From the effectiveness contours, it is perceived that the varying arrangement of the film holes may result in completely different effectiveness distribution. Due to the complex three dimensional nature of the platform secondary flow, it is of importance to strategically lay out the film cooling holes on the platform.

Figure 2.13 shows the effect of blowing ratio on the laterally-averaged film-cooling effectiveness. The laterally-averaged film-cooling effectiveness for the case of purge flow cooling only (ref [29]) is also presented (in black solid lines) as reference. The data repeatability is proven from the overlap of the effectiveness results from upstream purge flow. The film coverage from

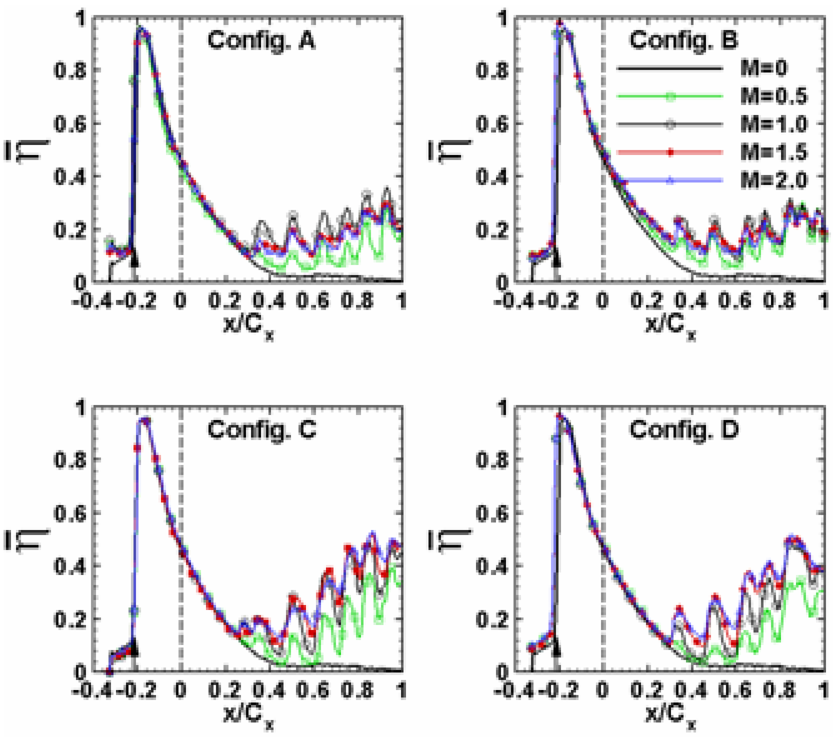

Fig. 2.13 Laterally averaged film cooling effectiveness (effect of blowing ratio)

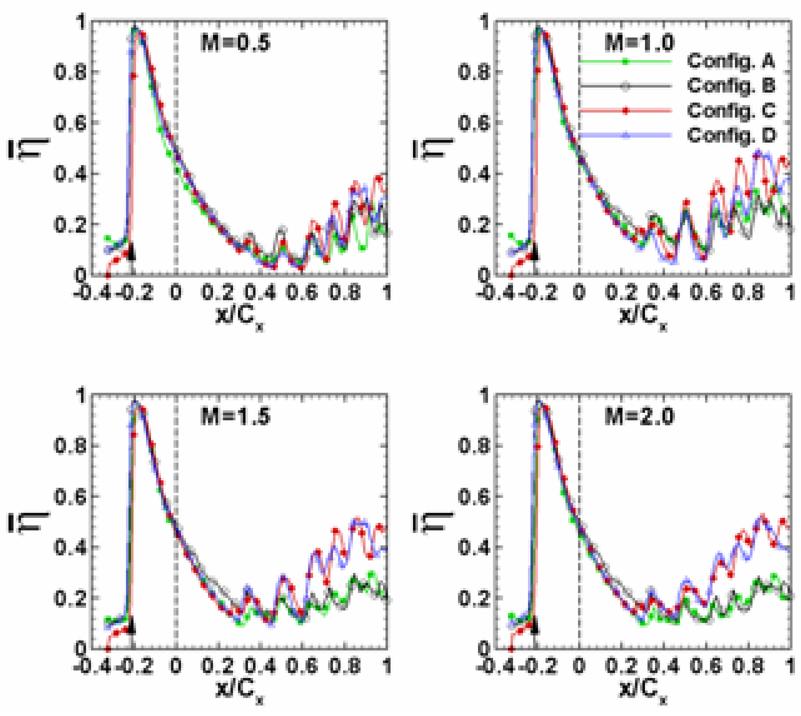

Fig. 2.14 Laterally averaged film cooling effectiveness (effect of hole configuration)

the purge flow alone on the downstream region of the platform was negligible. With the discrete hole film-cooling, the film-cooling effectiveness in the downstream region increased significantly. For the cylindrical holes (Config. A and B), the best film-cooling effectiveness was obtained at M=1.0. The effectiveness levels for M=1.5 and M=2.0, which were slightly lower than M=1.0, were comparable. For the shaped holes (Config. C and D), the film-cooling effectiveness increased with average blowing ratio. From M=1.5 to M=2.0, the increment was not significant.

Figure 2.14 shows the effect of hole configurations on laterally-averaged film-cooling effectiveness. At low blowing ratio, M=0.5, the film-cooling effectiveness from the four hole configurations were comparable. The advantage of shaped holes became evident when the average blowing ratio increased. At M=1.5 and 2.0, the laterally-averaged film-cooling effectiveness from the shaped holes was substantially higher than that from the cylindrical holes. The difference in laterally-averaged effectiveness resulting from the different layouts was subtle. The two-row layout presented slightly better averaged effectiveness than the four-row.

2.5 Total Pressure Loss Measurement

To evaluate the mainstream total pressure loss, the exit total pressure was normalized with the inlet total pressure ($\pi = P_{t,ex}/P_{t,in}$). The inlet total pressure was measured upstream of the purge slot by a pitot-static probe. The exit total pressure was measured along a 2-D plane located at an axial distance of $0.5C_x$ downstream of the trailing edge. An array of eight (diameter=2.38mm) pitot tubes was spaced out equally spanning 1.5 pitches. Figure 2.15 shows the 2-D plane with the measurement points. The plane shows two blade passages with the passage containing the film-cooling holes located on the left half of the plane. The eight pitot tubes traversed 10 locations in the vertical direction that covered 40% of the span from the hub. The pressures were recorded by a 48-channel Scanivalve System interfaced to a LabView software. The total pressure on the exit plane was measured for both cooled and un-cooled platforms.

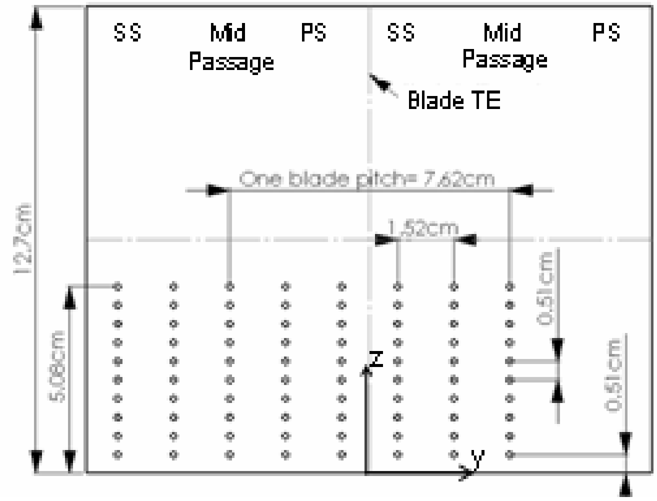

Fig. 2.15 Traversing plane for total pressure measurement

It can be seen from Fig. 2.16 that the dominant loss was introduced by the passage vortex. The loss core located approximately 30% of span from the platform for the uncooled case raised slightly when purge flow was introduced. The purge slot ejection (MFR=0.75%) produced greater and wider losses. Near-wall region, however, did not show any significant change. Since the cooling hole layouts did not show significant impact on the laterally-averaged film-cooling effectiveness, it was conjectured that the alteration of flow field from the hole layout would be little. Therefore, only Config. A (cylindrical holes) and Config. C (shaped holes) were assessed

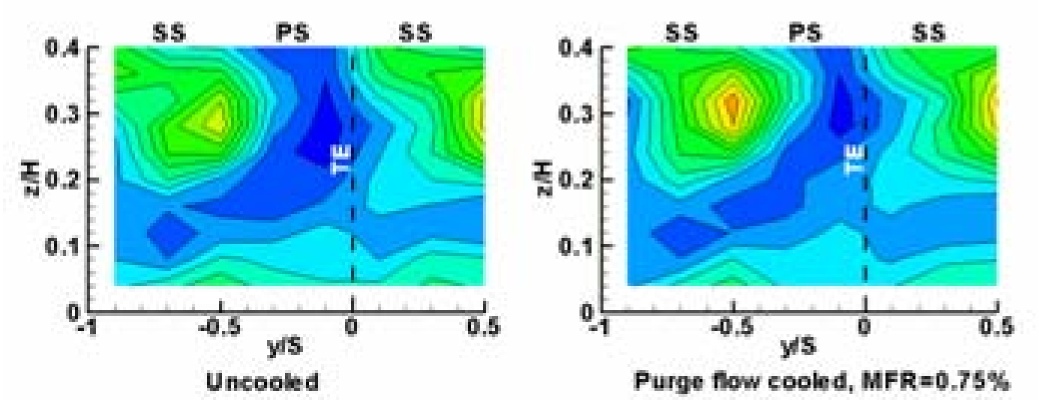

Fig. 2.16 Total pressure distribution at the cascade exit. (a) No coolant ejection. (b) Coolant ejection from purge slot.

for the total pressure loss with the combined film-cooling scheme. Figure 2.17(a) shows the total pressure loss maps with the platforms cooled by both purge flow and discrete-hole ejection (Config. A). In comparison to Fig. 2.17(b), the loss area broadened with the addition of coolant ejection from cylindrical holes. Moreover, the total pressure loss was also higher. This is because after leaving the film holes, the coolant interacted with the mainstream creating mixing losses. Figure 2.17(b) shows the total pressure loss maps for Config. C. With this configuration, the size and strength of the passage vortex became comparable to that in Fig. 2.16(b) (purge flow ejection only). Due to the diminished jet momentum, the coolant from the shaped holes remained attached to the platform surface. The coolant infused momentum into the boundary layer thus raising its total pressure and lowering losses. The coolant exiting from discrete cylindrical holes did not stay closer to the surface to help lower the losses in a similar fashion.

2.6 Film-Cooling Effectiveness on the Blade Platform using TSP

PSP technique is limited to film-cooling effectiveness measurements only. Temperature sensitive paint (TSP) technique, on the other hand, is applicable to both film-cooling and heat transfer measurements. Since the current work is part of a two stage study of film-cooling and heat transfer coefficient, TSP technique was adopted over PSP. Before employing this technique, a sample test (Tu=4.2%, MFR=0.75%, M=0, and DR=1.0) was performed to determine its suitability as a tool to measure adiabatic film-cooling effectiveness. The data was compared with the PSP test data carried out under the same experimental conditions. Both results showed reasonable agreement with each other.

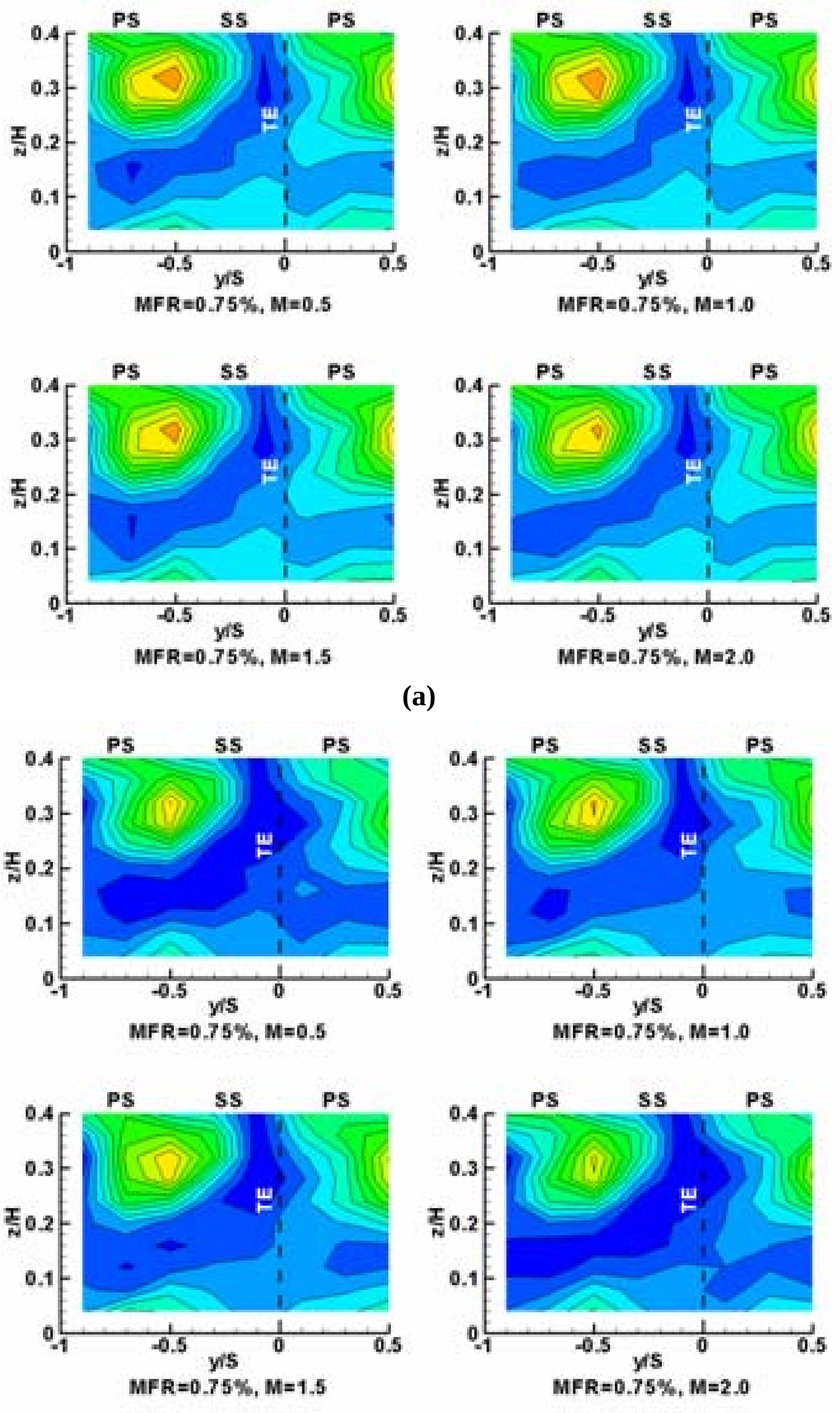

(a)

(b)

Fig. 2.17 Total pressure distribution at the cascade exit for coolant ejection with purge flow combined with discrete holes (a) Config. A (b) Config. C

The temperature distribution on the platform surface is mainly a function of the flow characteristics in the passage. The secondary flow vortices and the flow acceleration in the passage create local temperature footprints. The uneven surfaces created by the upstream slot and the cooling holes alter the mainstream flow and temperature locally. A typical platform surface temperature map without cooling is shown in Fig. 2.18(a). The pressure side corner and the trailing edge region generally experienced the highest temperature. When coolant was introduced, the area downstream of the coolant source was cooled as shown in Fig. 2.18(b), except for the pressure side corner where higher mainstream air pressure suppressed coolant exit from the holes. The nature and extent of overall cooling depend on various factors, four of which are discussed below.

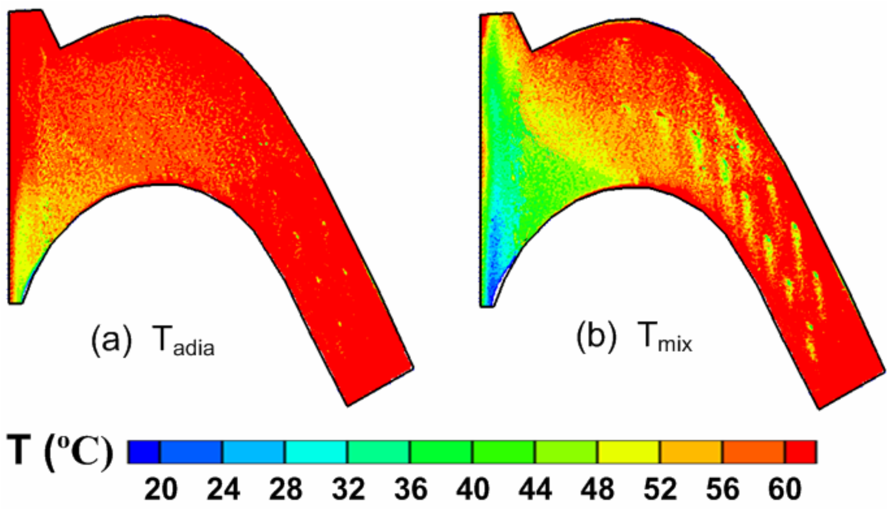

Fig. 2.18 Sample temperature maps on the platform surface

Effects of Freestream Turbulence

The PSP results from the same cascade and cooling geometry but at low density ratio of 1.0 and low freestream turbulence of 4.2% established that the best effectiveness from film holes is obtained at an optimum blowing ratio of 1.0. Another study, ref [21], found that a purge flow rate of 0.5% offered very good coolant coverage compared to 0.25%. At 0.75% and beyond, the coverage was only slightly better than 0.5%. With these two studies serving as a guide, the effect of freestream turbulence was investigated at a blowing ratio of 1.0 and a purge flow of 0.5%. However, the density ratio was raised to 1.8 to allow for tests that were closer to engine conditions. Figure 2.19 shows the effectiveness distributions at the low and high freestream turbulence levels. Irrespective of the freestream turbulence level, one can immediately observe that the purge flow was swept aside by the passage cross-flow. The passage vortex (conceptually shown by a helix) that originates at the blade leading edge and gains in strength as it travels downstream, formed a barrier that prevented coolant from traveling downstream. The vortex left an area near the blade pressure side completely uncovered. The farthest the coolant traveled was a distance roughly 40% of the axial chord from the blade leading edge. Higher turbulence level in the mainstream created more mixing between the coolant and mainstream and produced lower effectiveness levels. This can be clearly observed from the distribution around film holes. The

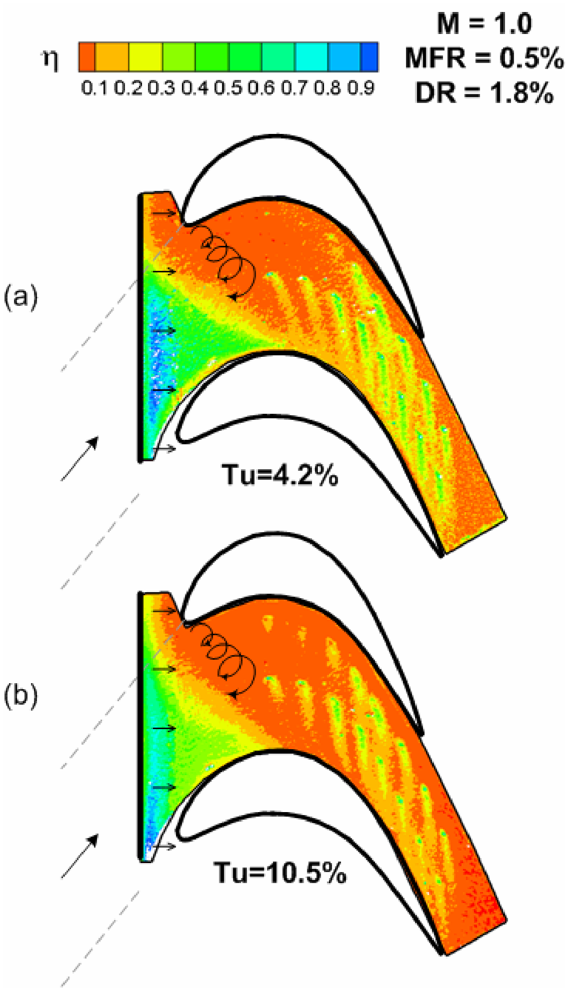

Fig. 2.19 Adiabatic effectiveness distribution at two different freestream turbulence intensities

coolant traces in the case of low turbulence were longer and distinct. At the elevated turbulence level, the coolant traces decayed very rapidly. Additionally, in the former case, the coolant coverage in between the holes was better. The purge flow distribution was also highly affected by the level of freestream turbulence. Unlike the high turbulence case, coolant barely emerged from the pressure side end of the slot at low freestream turbulence. However, the concentration of the coolant or the effectiveness level was higher for the latter case. The asymmetric nature of coolant distribution for the low turbulence case points towards stronger horseshoe vortex influence. This can be explained if we consider the approach flow boundary layer for the two cases (Fig. 2.15(b)). At the elevated turbulence flow, the velocity profile was flatter near the platform thus generating a less intense horseshoe vortex. At the low turbulence flow, the velocity gradient normal to the platform was higher, producing a stronger horseshoe vortex and reducing effectiveness levels on the pressure side end of the slot.

Effects of Purge Flow

To examine whether the cooling trends observed in ref. [21] with low density coolant also holds well with high density (DR=1.8) coolant and high freestream turbulence (Tu=10.5%), three purge flow rates- 0.25%, 0.5%, and 0.75% of mainstream flow were tested. These were equivalent to blowing ratios of 0.11, 0.22 and 0.33, respectively. A representative blowing ratio of 1.0 for film holes was used. The effectiveness contour plots are shown in Fig. 2.20. The coolant traces from film holes were nearly identical. Some improvement in downstream film-hole effectiveness is normally expected with increasing purge flow, since the purge flow acts to diminish the strength of the horseshoe vortex and therefore its influence on cooling holes. However, in the present design, the cooling holes were located downstream of the vortex separation line, which explains why the cooling holes largely remain unaffected by alteration of the purge flow. The effectiveness distribution from the variation of purge flow was rather straightforward. The coolant coverage improved with increasing purge flow. At the lowest purge flow rate of 0.25%, coolant appeared from only half the slot width as the low momentum ratio (I=0.006) coolant was swept aside easily by the horseshoe vortex. In fact, in the region where coolant was absent, ingestion of mainstream air cannot be ruled out. At MFR=0.5% (I=0.023), the coolant on account of its relatively higher momentum ratio, emerged from the other half of the slot as well. However, the distribution was asymmetric as the horseshoe vortex lifted some coolant off and left a bow-like trace. The asymmetry lessened at MFR=0.75% (I=0.052) as more coolant exited from the pressure side end of the slot.

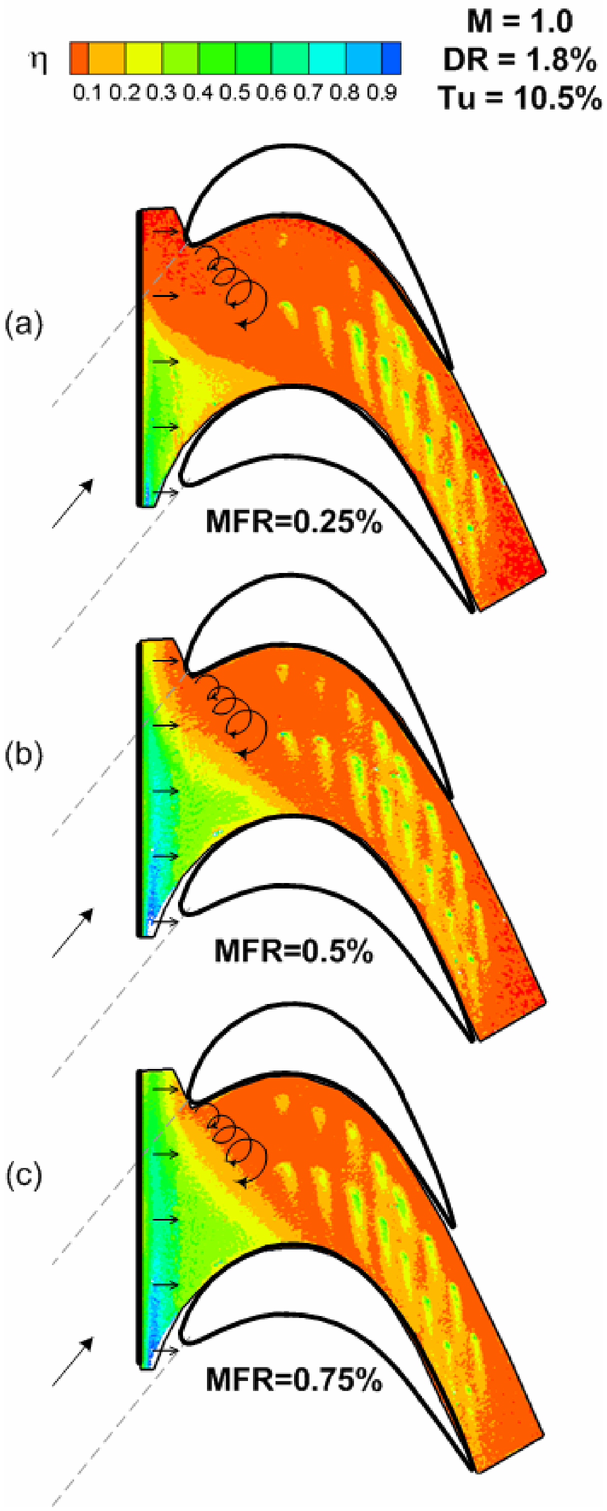

Fig. 2.20 Adiabatic effectiveness distribution at three different purge flow rates

Effects of Blowing Ratio

Film effectiveness distributions for a range of blowing ratio are shown in Fig. 2.21. Representative values of purge flow rate (MFR=0.5%), density ratio (DR=1.8), and freestream turbulence (Tu=10.5%) were selected to simulate engine-like flow conditions. As expected, the same purge flow delivery in all the three cases produced identical coolant distribution downstream of the slot. Raising the blowing ratio from 1.0 (I=0.526) to 1.5 (I=1.18) resulted in increased effectiveness as seen from the longer, distinct coolant traces and the even distribution of coolant in between the holes. Raising the blowing ratio further to 2.0 (I=2.1) produced sharp drop in effectiveness with much thinner and shorter coolant traces. This could be attributed to the coolant lift-off and mixing with the mainstream facilitated by a two-fold increase in coolant momentum ratio for a blowing ratio increase from 1.5 to 2.0. Baring a small area in the mid-passage region, coolant coverage was limited. Comparing with the study done earlier using PSP, one conclusion that can be drawn immediately is that the effect of increasing the density ratio is to raise the optimum blowing ratio value when other parameters are kept constant ($M_{optimum}$=1.0 for DR=1.0, and $M_{optimum}$ =1.5 for DR=1.8).

Effects of Density Ratio

The effectiveness contour plots for a range of density ratio are presented in Fig. 2.22. Freestream turbulence, purge flow, and blowing ratio were fixed at 10.5%, 0.5%, and 1.0, respectively. The coolant distribution immediately downstream of the slot showed distinct variation with density ratio. For low density ratio of DR=1.1, the coolant distribution was almost uniform across the slot. At DR=1.8, the distribution was skewed with more coolant appearing from the end close to the blade suction side, indicating strong horseshoe vortex influence. At DR=2.1, the distribution was skewed as well but the coolant concentration shifted towards the center of the slot. It may be noted that for the same blowing ratio, the coolant momentum ratio (I) decrease with increasing density ratio. Higher momentum coolant stands a better chance of warding off strong vortex effects than low momentum coolant, which may explain the skewness observed at high density ratios. When the passage vortex traveled downstream, the coolant traces from film holes, particularly those upfront in the mid-passage row, were redirected towards the streamwise direction. The holes on the pressure-side row were largely unaffected by the vortex. At DR=1.1, the coolant dispersed immediately as it emerged from the holes. The maximum effectiveness values were found above the holes, with an average value of around 0.35. When

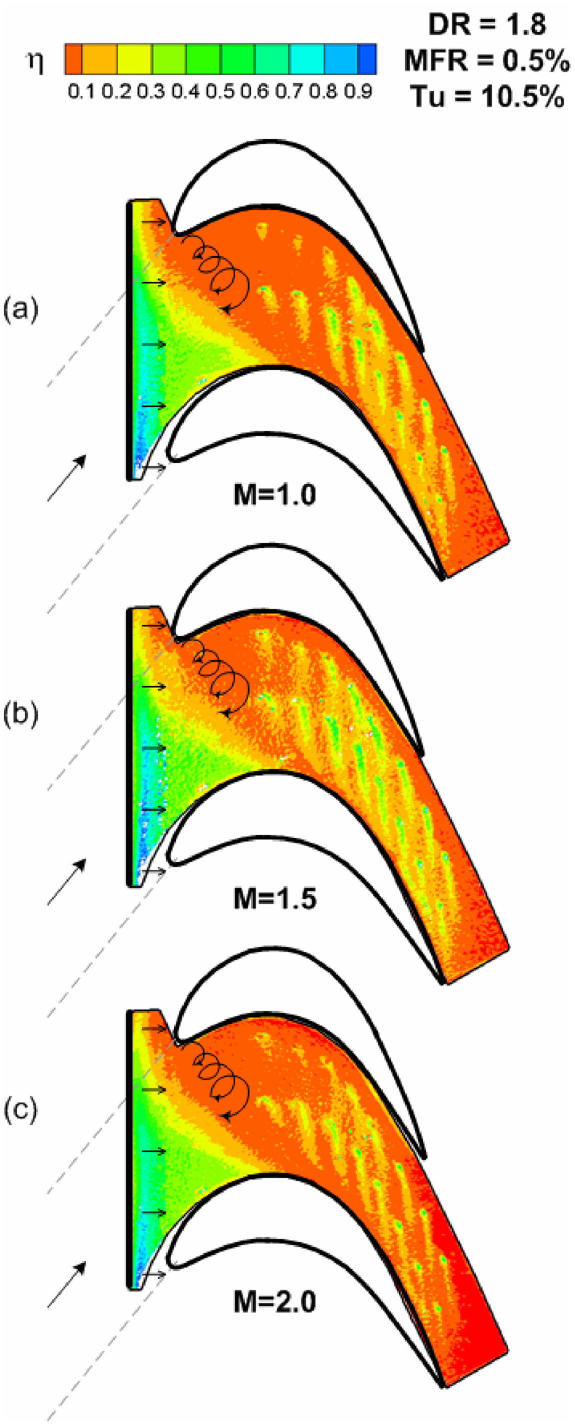

Fig. 2.21 Adiabatic effectiveness distribution at three different blowing ratios

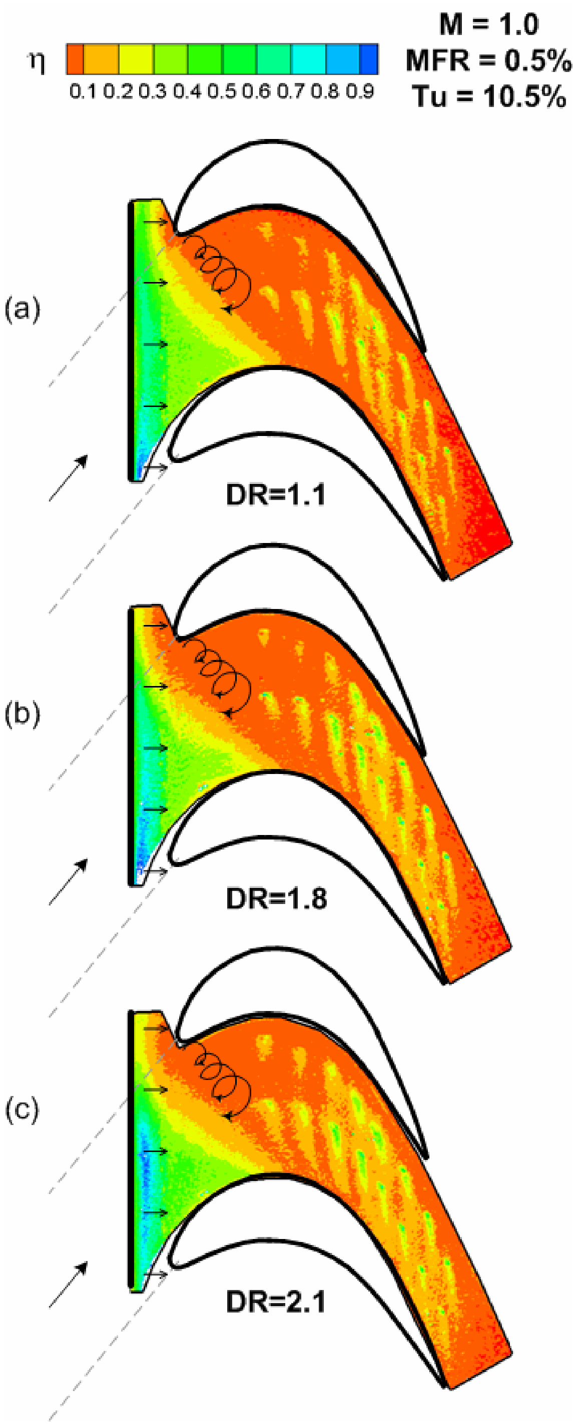

Fig. 2.22 Adiabatic effectiveness distribution at three different density ratios

density ratio increased to 1.8, the coolant traces were distinct and longer with effectiveness values reaching close to 0.6 above the holes. The higher coolant momentum (I=0.877) in the case of low density coolant facilitated jet detachment from the platform resulting in lower film-effectiveness whereas lower coolant momentum (I=0.526) for high density coolant kept the jet attached to the platform surface producing longer and distinct coolant traces. When the density ratio was increased to 2.1, there was only a small improvement in effectiveness compared to the DR=1.8 case.

Laterally-Averaged Effectiveness

The results of laterally-averaged effectiveness are presented in Figs. 2.23(a) through (d).The point x/C_x=0 and 1.0 corresponds to the blade leading and trailing edge. The purge flow exits the slot at x/C_x=-0.2. It may be observed that the two cooling sources are clearly depicted on the plots –a set of curves from purge flow cooling peaking at around x/C_x=-0.15, then falling off steadily and a set of much smaller peaks after $x/C_x>0.4$ resulting from jets issued out from discrete holes. The six tiny peaks between x/C_x=0.4 and 1.0 arise from the six pairs of holes between the blade leading and trailing edges. The rest of the four holes out of a total of sixteen holes fall outside the range of the blade axial chord length and hence excluded from averaging.

As seen earlier from the contour plots, lower freestream turbulence led to higher effectiveness levels throughout the platform, except immediately near the slot where the high turbulence flow case displayed slightly higher effectiveness, Fig. 2.23(a). Close to the blade trailing edge, the effectiveness levels were twice as high for the low turbulence level case. Increase in purge flow showed clear gain in effectiveness that extended to a downstream distance of x/C_x=0.5, at which point the effectiveness levels began to collapse into a single curve, Fig. 2.23(b). Same hole blowing ratio for all the three cases gave rise to similar downstream cooling pattern. The peak effectiveness registered a 75% increase when the purge flow was increased from 0.25% to 0.5% but produced a meager 12% increase when raised from 0.5% to 0.75%. If one has to extrapolate this trend, a further increase in purge flow should bring forth even lesser benefit in terms of percentage increase in effectiveness. Gao et al. [21] reported a similar finding with purge flow ranging between 0.25% and 1.0% at low coolant-to-mainstream density ratio of 1.0. The effectiveness levels from film-holes increased by around 40% when blowing ratio was increased from 1.0 to 1.5, Fig. 2.23(c). With further increase to 2.0, the effectiveness levels dropped sharply, even dropping below the level at M=1.0 by an average of 16%. The same upstream purge flow rate produced nearly identical effectiveness levels downstream of the slot in all the three cases.

Finally, from Fig. 2.23(d), it appears that the cooling process associated with purge flow follow a different pattern than the discrete hole cooling. While the film holes showed increased effectiveness levels with increasing density ratio (or decreasing momentum ratio), the same was

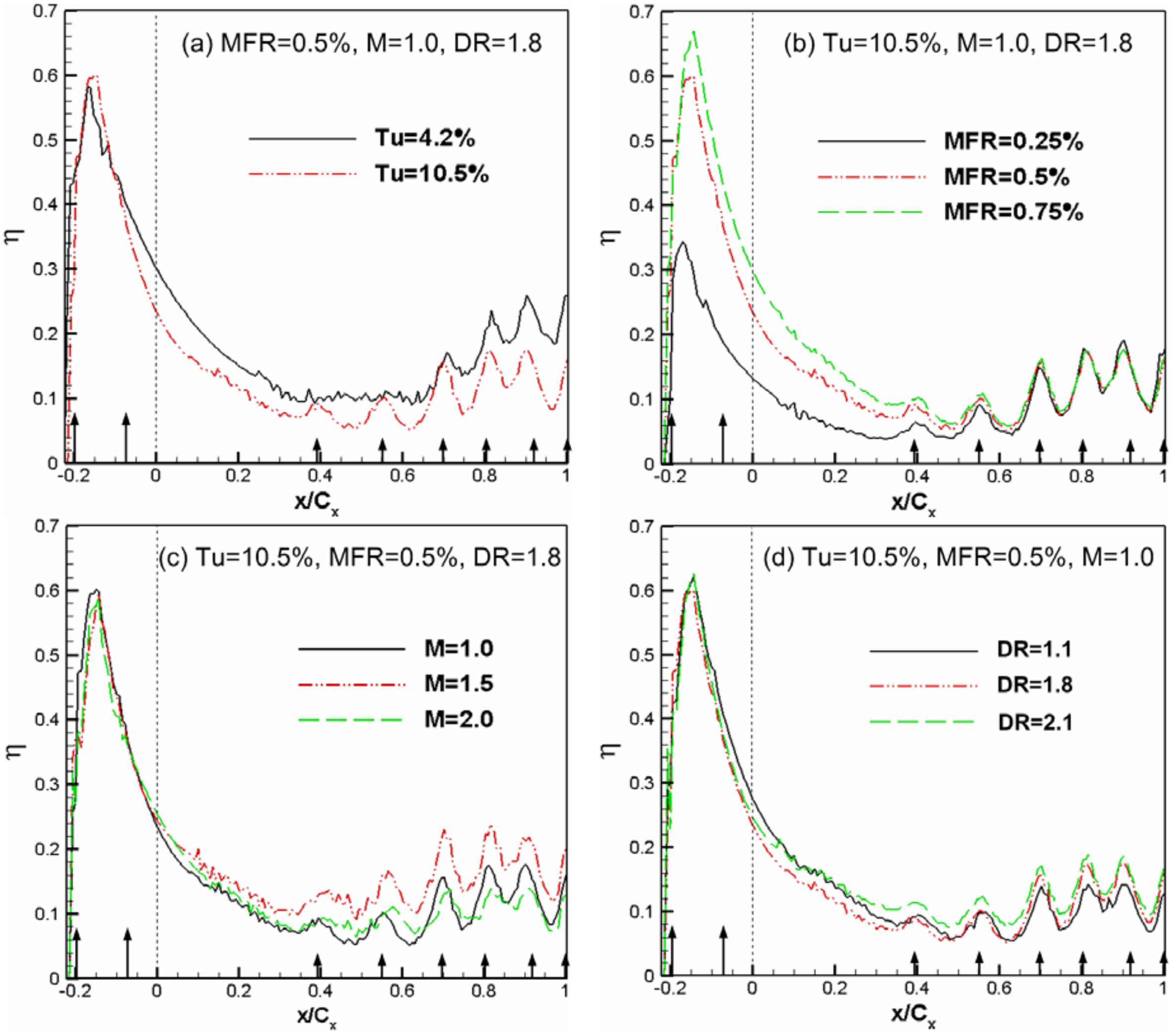

Fig. 2.23 Laterally averaged adiabatic effectiveness as a function of (a) turbulence intensity (b) purge flow rate (c) blowing ratio, and (d) density ratio

not true for the purge cooling. Since secondary vortices plays a dominant role in determining the near-slot cooling, higher momentum coolant stands a better chance at warding off strong vortex flows. Therefore, in the region between the slot and the blade leading edge, the lower density ratio coolant (I=0.039) produced slightly higher level of effectiveness than the other two (I=0.023 for DR= 1.8; I=0.021 for DR=2.1). With increasing axial distance, effectiveness levels increased on account of coolant accumulation.

3. TURBINE BLADE SPAN FILM COOLING

3.1 Introduction

The extent of literature available in this area is really vast with majority of the recent work focusing on some form of comparative assessment of two or more hole configurations from among the four mentioned earlier. Goldstein et al. [37] is credited as the first to show the benefits of film-cooling with shaped holes. Their study compared film-cooling effectiveness for straight round holes and axial shaped holes with lateral diffusion of 10^o. The axis of both the hole geometries were inclined at 35^o from the test surface. They reported a significant increase in the film-cooling effectiveness immediately downstream of the shaped holes as well as increased lateral coolant displacement. They attributed this effect primarily on the reduced mean velocity of the coolant at the hole exit causing the jet to stay closer to the surface. Thole et al. [38] carried out flow field measurements using LDV at the exit of three different hole geometries. The hole geometries included: a round hole, a hole with a laterally expanded exit, and a hole with a forward-laterally expanded exit; all inclined at an angle of 30^o from the surface. Their findings showed that both the shaped holes had less shear mixing of the injection jet with the mainstream and greater lateral spreading of the coolant compared to that of the round hole. Additionally, the forward-laterally shaped hole had relatively lower film effectiveness than the laterally expanded hole shape due to excessive diffusion of the coolant and subsequent mainstream interaction. Gritsch et al. [39] studied the same cooling hole configurations and orientations as [2] with a density ratio of 1.85. Their film-cooling effectiveness measurements were confined to $x/D < 10$ in order to focus near the cooling hole. Compared to the cylindrical hole, both expanded holes showed significantly improved thermal protection of the surface downstream of the ejection location, particularly at high blowing ratios. Along similar lines, Yu et al. [40] studied film-effectiveness and heat transfer distributions on a flat plate with straight circular hole, 10^o forward diffusion shaped hole, and another type of hole with an additional 10^o lateral diffusion. In each case, the axis of the hole was inclined 30^o relative to the mainstream direction. The last mentioned hole provided the highest film-cooling performance as well as overall heat transfer reduction. All of the above studies were performed on a flat plate with axially oriented holes.

Schmidt et al. [41] examined film-cooling performance of 60^o compound angled holes on a flat plate surface, with and without forward expanded shaped exit, and compared that with cylindrical holes aligned with the mainstream. The round and shaped exit holes with compound angle had significantly greater effectiveness at larger momentum flux ratios. The compound angle holes with expanded exits had a much improved lateral distribution of coolant near the hole for all momentum flux ratios. Dittmar et al. [42], in a slight deviation, conducted measurements on a model of a suction side of an actual turbine guide vane inside a wind tunnel. Four different cooling hole configurations- a double row of cylindrical holes, a double row of discrete slots, a single row of straight fan-shaped holes, and a single row of compound angle fan-shaped holes were chosen to study adiabatic film-cooling effectiveness and heat transfer coefficient. Both the shaped holes featured expansion only in the lateral direction. The streamwise injection angle was 45^o for all cases with an additional lateral angle of 35^o from the mainstream direction for compound shaped holes. According to their study, fan-shaped holes provided good effectiveness values at moderate and high blowing ratios unlike the cylindrical holes which suffered from jet separation. In another study involving pressure and suction side models inside a wind tunnel, Chen et al. [43] investigated both axial and compound shaped holes with forward diffusion. The compound angle in their study was 45^o. On the concave surface, improvement in laterally-averaged effectiveness due to the addition of compound angle was found at high blowing ratio of 2. On the convex surface, significant improvement in effectiveness was seen at both low and high blowing ratios.

Hole shape study in linear cascades are fewer in comparison to those in flat plate and model airfoils. Teng and Han [44] studied one row of film holes near the gill-hole portion of the suction side. The hole geometries considered in their study were same as those of [37] and [38] but with a slightly higher inclined angle of 45^o. They reported that spanwise-averaged film effectiveness of shaped holes could be about two times higher than that of cylindrical holes. In addition, fan-shaped holes performed better than laidback fan-shaped holes. More recently, Mhetras et al. [45] observed the excellent coolant coverage offered by compound shaped holes near the tip region of the pressure side. Their study showed that the shaped holes on the pressure side of the blade could be utilized in cooling the cut-back region of the tip cavity floor. Garg [46] used a three-dimensional Navier-Stokes code to perform a detailed heat transfer coefficient and film-cooling effectiveness analysis on a rotating high-pressure turbine blade with 172 film-cooling holes in eight rows. The effectiveness is shown to be lowest in the tip region and in the leading edge region between the hub and blade mid-span.

Effect of a rotating, unsteady wake on film cooling effectiveness and coolant jet temperature profiles on the suction side of a turbine blade were investigated by Teng et al. [47] in a low speed cascade. A spoked-wheel mechanism was used to generate the upstream wakes. They found that unsteady wake reduced the effectiveness magnitudes. Local heat transfer immediately downstream of the holes was found to increase by as much as 60% due to film injection. Ou et al.

[48] simulated unsteady wake conditions using the same mechanism as [47] over a linear turbine blade cascade with film cooling. They tested no-wake case and wake Strouhal numbers of 0.1 and 0.3. Air and CO_2 were used to study effect of density ratio. It was found that increasing wake passing frequency increases local Nusselt numbers for all blowing ratios, but this effect is reduced at higher blowing ratios. It was concluded that the additional increases in Nusselt numbers due to unsteady wake, blowing ratio, and density ratio were only secondary when compared to the dramatic increases in Nusselt numbers only due to film injection over the no film holes case. They concluded that heat transfer coefficients increased and film-cooling effectiveness values decreased with an increase in unsteady wake strength. Further, Mehendale et al. [49], in the same test facility and for the same experimental conditions, found that an increase in wake Strouhal number led to a decrease in film effectiveness over most of the blade surface for both density ratio injectants and at all blowing ratios. Du et al. [50] performed a similar experiment with the addition of trailing edge coolant ejection from the wake-producing bars. The addition of wake coolant had a relatively small effect on downstream blade heat transfer coefficient, but reduced leading edge film effectiveness below the wake case with no coolant ejection. Detailed heat transfer measurements on transonic film-cooled blade with and without NGV shock waves and wakes were made by Rigby et al. [51]. It was found that there was a significant change of film-cooling behavior on the suction surface when simulated NGV unsteady effects were introduced. Heidmann et al. [52] studied the effect of wake passing on showerhead film-cooling performance in an annular cascade with an upstream rotating row of cylindrical rods. A high wake Strouhal number was found to decrease effectiveness but it was also found to divert the coolant towards the pressure side resulting in slightly better cooling on the pressure side.

Detailed investigation of film-cooling effectiveness for a turbine blade with cylindrical holes on the pressure and suction side along with showerhead injection at the leading edge was carried out by Mhetras et al. [53] in a 5-blade linear cascade. The parameters involved in their study include upstream stationary wake rods and blowing ratio. Two wake rod diameters were used to replicate typical trailing edge geometry. The blowing ratio range was from 0.3 to 1.2. From their study, the highest effectiveness was seen at M=0.9 and wake phase positions 0% and 25% with respect to the blade pitch exerted the greatest influence on effectiveness, particularly on the suction side. This study was an extension of this, the chief difference were the exit shape of the cooling holes on the pressure and suction surface. The cooling hole arrangement and the internal coolant supply passages were modeled similar to typical blade designs used in commercial gas turbines. Experiments were performed with relatively high freestream inlet and exit Mach numbers of 0.27 and 0.44, respectively. The primary variables in the study were – location of upstream stationary wake rods, and blowing ratio. Results are presented in the form of film-cooling effectiveness contour plots obtained using Pressure Sensitive Paint (PSP) technique [54] and spanwise-averaged effectiveness derived from these contour plots. Past studies have not captured detailed local film-cooling effectiveness distribution on an entire blade surface with fan-shaped, laidback compound angled holes and under the influence of upstream wakes.

The PSP technique used for measuring film cooling effectiveness is based on heat and mass transfer analogy and is free from heat conduction related errors frequently encountered with other heat transfer measurement techniques measuring adiabatic effectiveness. PSP works by sensing the partial pressure of oxygen on the test surface. By displacing the oxygen on the platform via nitrogen injection from the film holes and by measuring the relative difference between air and nitrogen injection, the film cooling effectiveness can be calculated. Since no heating is involved, errors resulting from lateral heat conduction in the test surface are avoided resulting in a clean and well-defined coolant trace. Other advantages of this technique are the non-intrusive nature of measurement, and higher spatial resolution. The results from this technique have been calibrated with other measurement techniques by Wright et al. [55] on a flat plate and Gao et al. [56] on a film-cooled cylindrical leading edge model in low speed wind tunnels. Gao et al. [56] compared results obtained from a steady state PSP technique and a transient IR measurement technique. This technique has also been successfully applied to film-cooling effectiveness measurements on hub endwall by Wright et al. [55] and blade tip study by Ahn et al. [57].

3.2 Experimental Facility

Figure 3.1 shows the stereo lithography (SLA) test blade with the internal coolant supply passage and the film cooling holes. The test blade had a squealer tip with a recess of 2.4% of blade span (2.84mm) while the two adjacent blades had a flat tip. The tip clearance for the test blade and the two adjacent guide blades was 1% of the blade span. Three rows of showerhead film cooling holes with a diameter of 0.65mm were provided along the leading edge of the test blade. The middle row was aligned with the stagnation line while the other two rows were placed $\pm 15^{o}$ from the stagnation line. Each showerhead row had 22 holes with a hole-to-hole spacing of 5.3mm ($s/d = 8.2$). The length to diameter ratio (L/d) for all the showerhead holes was 12.7. Four rows of laidback, fan-shaped holes were provided on the pressure side at axial locations of 1.24cm (PS1, 23 holes), 3.62cm (PS2, 22 holes), 5.01cm (PS3, 23 holes) and 6.1cm (PS4, 22 holes). Two more such rows were provided on the suction side at axial locations of 0.38cm (SS1, 23 holes) and 3.56cm (SS2, 22 holes). All pressure and suction side holes were inclined 45^{o} away

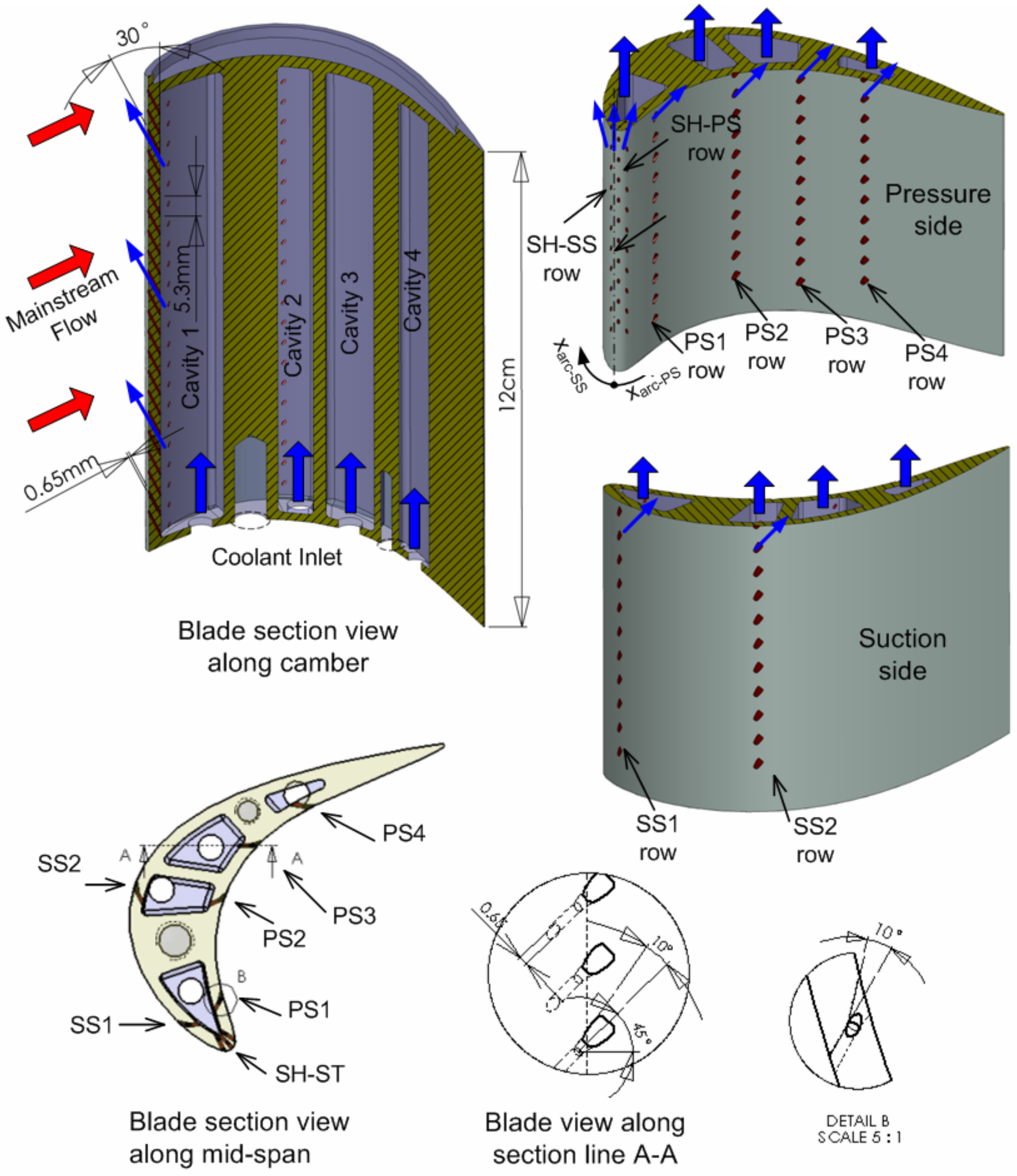

Fig. 3.1 Film cooled blade with compound shaped holes

from the blade surface in the mainstream flow direction as well as 45° away from the blade span. The lateral diffusion angle of the holes was 10° from the hole centerline and the forward expansion angle was 10°. The metering section of the hole had a diameter of 0.65mm, producing L/d ratio equal to 4.75. The total L/d of the hole was 9 and the expansion ratio (ratio of the exit break-out area to the inlet cross-section area) was equal to 11. The holes in nearby rows were staggered with respect to each other. Due to the staggered arrangement, rows PS2, PS4 and SS2 had one hole less. The s/d ratio was, however, maintained at 8.2. Coolant was supplied via 4 cavities, each cavity flow controlled by a rotameter. The first cavity near the leading edge was designed to supply coolant to the showerhead film cooling holes as well as rows PS1 and SS1. The second cavity was designed to supply coolant to rows PS2 and SS2. The remaining two cavities supplied coolant to rows PS3 and PS4, respectively. The cavity cross-sections were modeled similar to the internal cooling passages in turbine blades with coolant injection from the blade hub.

A set of four metal rods was stationed upstream of the blade row to simulate stationary, upstream wakes. The upstream distance was equal to 50% of axial chord from the blade leading edge. A rod diameter of 4.8mm was selected to replicate typical vane trailing edge thickness. The ratio of blade leading edge diameter (4.8 mm) to that of the vane trailing edge thickness modeled by wake rods is, therefore, 1. The distance between adjacent rods was equal to the blade pitch. The position when the rods were directly upstream of the blade leading edges was labeled as the 0% phase position with respect to the blade pitch. Phase positions 25%, 50%, and 75% were progressively located along the blade pitch as indicated in Fig. 3.2.

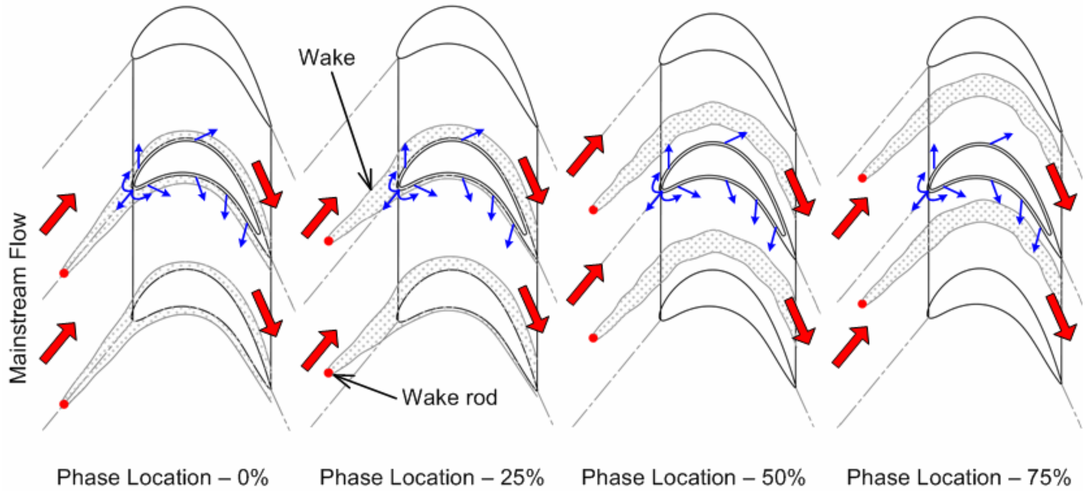

Fig. 3.2 Wake rod phase positions and conceptual view of wake path

The various phases represented what would be a progressing wake in a real turbine. Four sets of experiments were conducted to cover all phase locations. Four different average blowing ratios were selected – 0.3, 0.6, 0.9 and 1.2. The upper range was fixed by the structural limitation of the blade material. The amount of coolant supplied to each of the four cavities to attain a desired average blowing ratio was calculated using the equation

$$\dot{m}_c = \sum_{r=1}^{n} M\left[m''_m\right]_r \left[A_c\right]_r \tag{2}$$

where M is the average blowing ratio, r is the coolant hole row in a cavity, n is the number of rows in a cavity, m_m'' is the mainstream mass flux at row r, and A_c is the total area of all the coolant holes at row r. The mainstream mass flux at a given row location was calculated from the total pressure measured upstream of the test blade and static pressure obtained via surface taps at 50% blade span height. The total and static pressure measurements were performed without wake rods and film cooling. To obtain a first-hand knowledge of the back-flow pressure margin, the local pressure ratio between the coolant and the mainstream ($P_{t,cavity}/P_{blade}$) was calculated and the resultant plot is shown in Fig. 3.3. While calculating the pressure ratio, the total pressure inside the cavity ($P_{t,cavity}$) was assumed equal to the static pressure at the cavity entrance – this assumption made on the basis that the cavity cross-sectional area was far greater than that of the cooling holes. The surface static pressure (P_{blade}) was obtained by taking the average of the static pressures at three span locations – 50%, 75%, and 94%. As expected, pressure ratio on the suction side is higher than the pressure side. Particularly interesting are the near unity pressure ratio values at M=0.3 for the showerhead and pressure side holes in cavity 1 and the pressure side holes in cavity 2. Coolant ejection from these holes is expected to be almost negligible, therefore making such low average blowing ratio rather impractical.

It may be recalled that cavity 1 feeds coolant to five rows (SH-ST, SH-PS, SH-SS, PS1, SS1) and cavity 2 to two rows (PS2 and SS2) of holes. Because multiple rows share the same cavity, the blowing ratio from each individual row is expected to be different from the average blowing ratio. The actual or local blowing ratio for a given row can therefore be defined as the ratio of coolant mass flux to the mainstream mass flux at that particular row location. The coolant row mass flow rate is a function of the pressure differential across the row and was calculated using the equation

$$\dot{m}_{hole} = C_D\left(\frac{\pi}{4}d^2\right)\left(P_{t,cavity}\left(\frac{P_{blade}}{P_{t,cavity}}\right)^{(\gamma+1)/2\gamma}\right)\sqrt{\frac{2\gamma}{(\gamma-1)RT_c}\left(\left(\frac{P_{t,cavity}}{P_{blade}}\right)^{(\gamma-1)/\gamma}-1\right)} \tag{3}$$

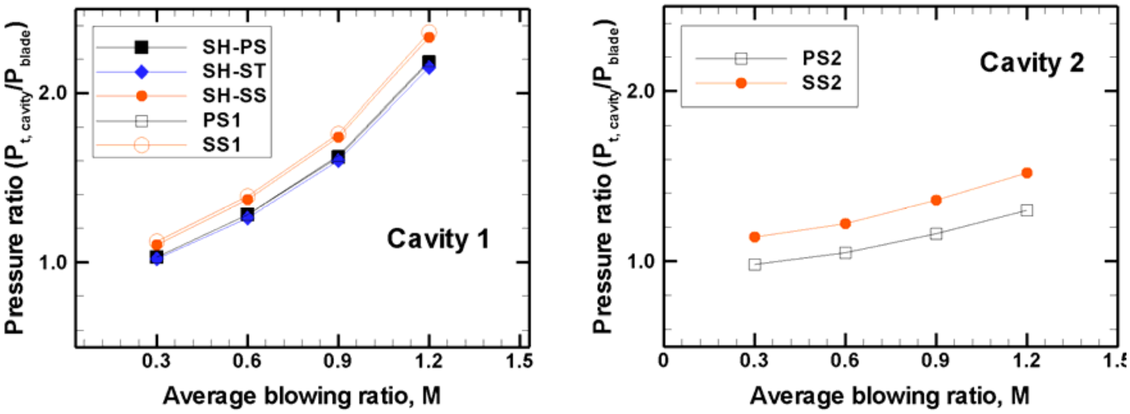

Fig. 3.3 Coolant-to-mainstream pressure ratio for coolant hole rows around cavities 1 and 2

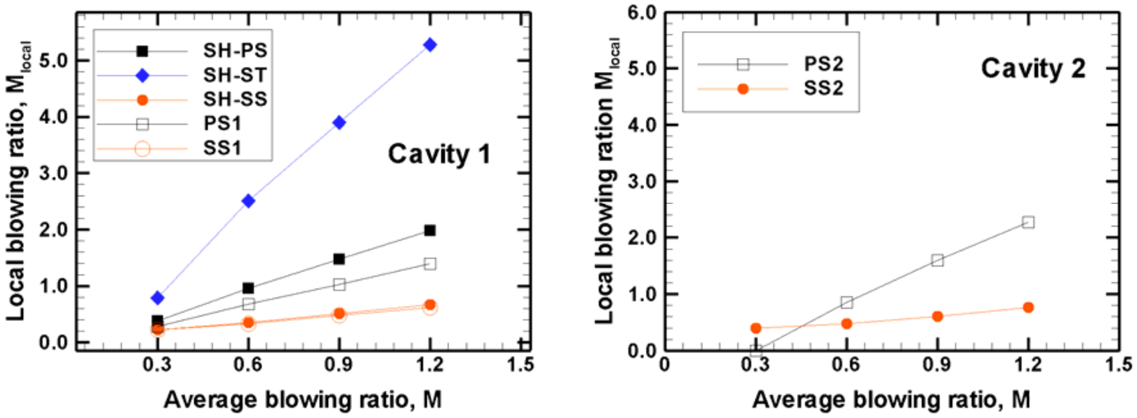

Fig. 3.4 Row based local (or actual) blowing ratio for film-cooling holes around cavities 1 and 2

where C_D is the discharge coefficient and was assumed constant for all the holes in a given cavity and for a given average blowing ratio. The coolant hole diameter use in the equation was that of the metering section of the hole. Figure 3.4 shows the actual blowing ratio for each row in cavities 1 and 2. The cooling holes along the stagnation line (SH-ST) display very high local blowing ratios due to low mainstream mass flux along that line. A notable observation from Fig. 8 is the higher local blowing ratio values than the average for pressure side hole rows (SH-PS and PS), and lower local blowing ratio values than the average for suction side hole rows (SH-SS and SS). This is especially true for the three highest average blowing ratios.

3.3 Flow Distribution on the Blade Surface

Figure 3.5 shows the Mach number distributions at three locations – 50%, 75% and 94% of total blade span, evaluated based on the knowledge of wall static pressures and inlet total pressure. Pressures were recorded with a 48-channel Scanivalve System driven by LabView software. LabView discarded all data that fell outside the initial mean ±1.5 standard deviation. It then recorded the mean value of the screened data. Every pressure measurement was repeated at least three times to reduce data uncertainty and verify data repeatability.The pressure side Mach number distribution for all the three span locations was nearly identical. A gradual decrease was observed up to $x/C_x \approx 0.6$, followed by a sharp rise. On the suction side, a steady increase up to $x/C_x \approx 0.65$ was accompanied by a gradual fall. The point of inflection on the suction side corresponded to the throat region where the mainstream attained its maximum velocity. The interaction of the mainstream boundary layer and tip leakage vortex could also be clearly observed from this plot, with an appreciable change in the pressure distribution in the first half of the blade axial chord for the 94% span case.

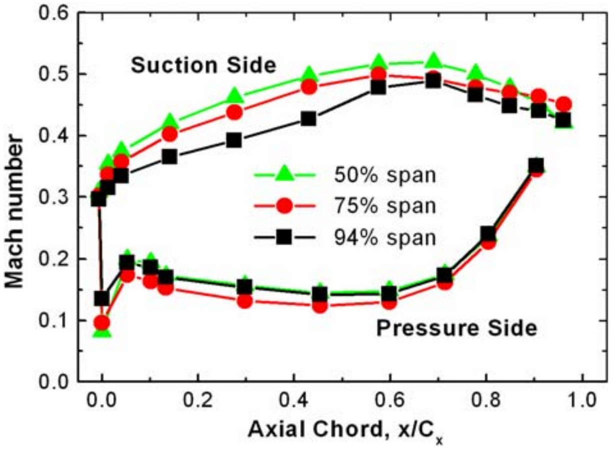

Fig. 3.5 Mach number distributions

Figure 3.6 show the pressure ratio distribution under the influence of stationary wakes at all phase locations and compares it with that of the no-wake case. Data is shown for the same three blade span locations. The pressure ratio was obtained by normalizing the blade inlet total pressure with the local static pressure on the blade surface. It is interesting to observe that the midspan

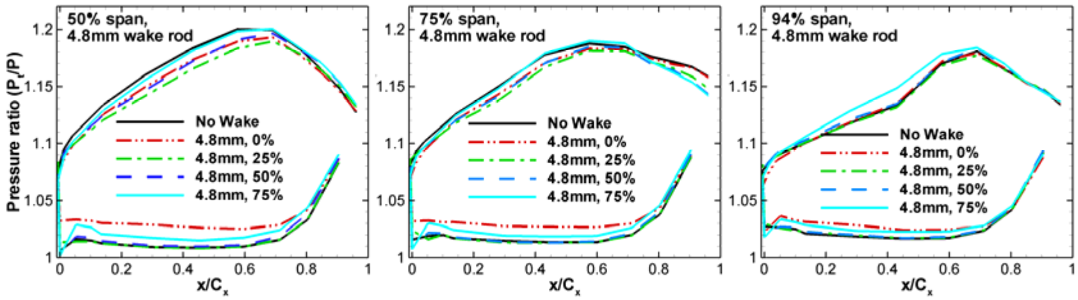

Fig. 3.6 Pressure ratio distributions on blade span under the influence of upstream wake rods

region (50% span) was most affected by the upstream rods followed by 75% and 94% span locations, which is indicative of the fact that strong endwall vortices prevailed over the small disturbances created by wake rods. The effects due to wake rods became apparent close to the midspan region where the influence of endwall vortices was almost negligible. It has to be noted that the pressure measurements were carried out on a blade without cooling holes. In the presence of cooling holes, however, the blade surface boundary layer experiences additional disturbance from coolant ejection, especially in the blade aft portion. In general, on the pressure side, the 0% phase location showed the maximum influence followed by the 75% case. The other two wake locations showed little or no effect. On the suction side, except for the 94% span case, the other two span locations also exhibited a definitive trend in the pressure ratio distributions. The phase positions in the decreasing order of influence on the suction side were – 25%, 0%, 50%, and 75%. This trend was as expected from the conceptual wake paths depicted in Fig. 4.2.

3.4 Film-Cooling Effectiveness Results

Data for film-cooling effectiveness were obtained by using the PSP technique. Film-cooling effectiveness distributions were obtained on the blade surface at different average blowing ratios and wake rod phase positions. Fig. 3.7 shows the film-cooling effectiveness distribution on the blade surface for the case without wake rods. The four maps correspond to four different average blowing ratios. The effectiveness map obtained at each individual camera position was projected onto a radial plane passing through the axial chord of the blade. The individual maps were then spliced to form a complete map of the pressure and suction side. The abscissa and the ordinate were normalized with the axial chord length and the blade height respectively.

The driving force behind coolant ejection is the coolant-to-mainstream pressure ratio ($P_{t,cavity}/P_{blade}$) across the holes. Thus, for coolant ejection, the pressure inside the cavity must be greater than the pressure outside the blade. The coolant after entering the cavity stagnates near the tip (*y/H* = 1) setting up a pressure gradient from the hub to the tip, with higher pressure near the tip. The higher cavity pressure may result in higher coolant mass flow from holes close to the tip. Further, for film cooling rows on the pressure and suction sides that share the same coolant supply cavity, bulk of the coolant is discharged from the suction side holes on account of higher pressure ratio. The uneven coolant distribution on two sides of the blade could be observed at M = 0.3 for cavities 1 and 2. The higher pressure ratio on the pressure side made it nearly impossible for coolant to appear from the showerhead, PS1, and PS2 rows at such low average blowing ratios. At higher average blowing ratio, the increased cavity pressure enabled the coolant

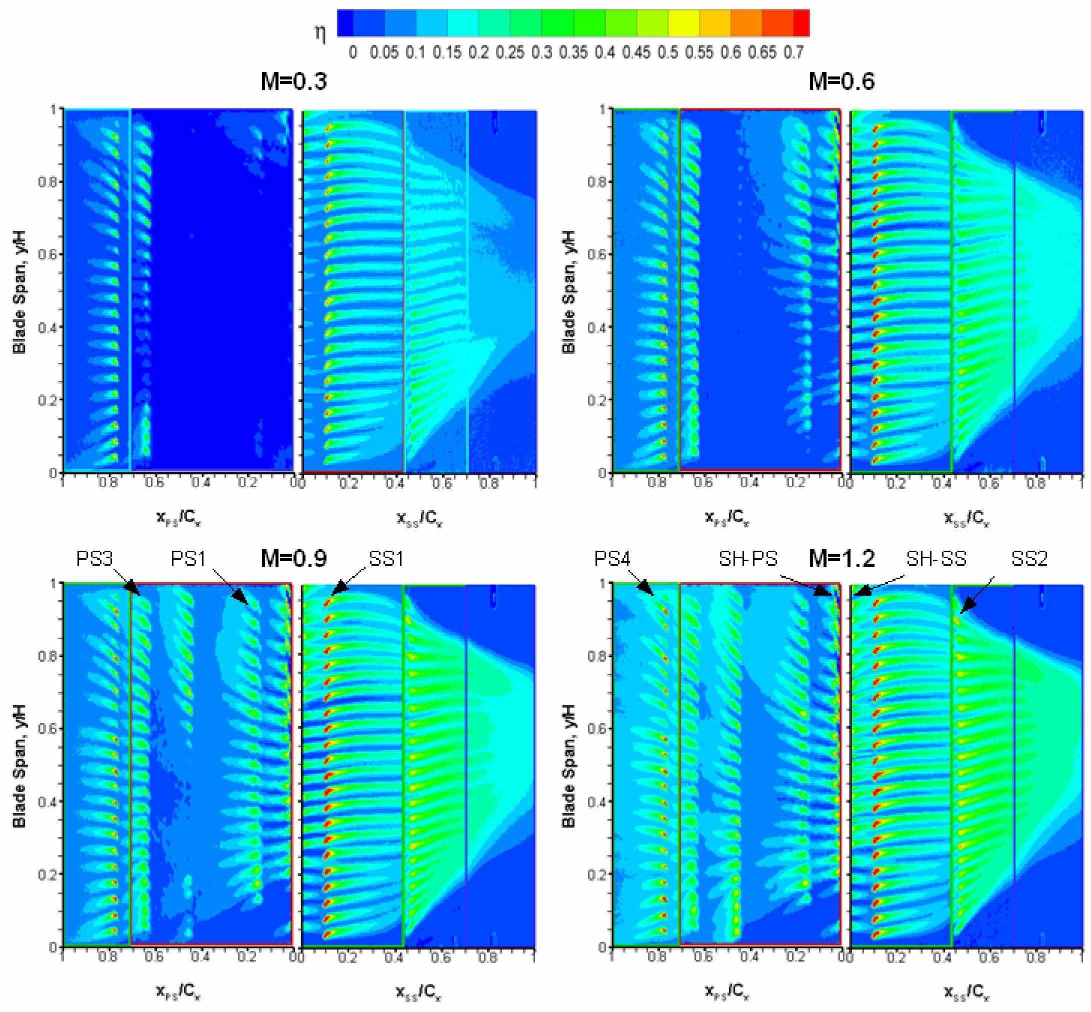

Fig. 3.7 Contour plots of film cooling effectiveness distribution without wake

to escape, giving a reasonably even distribution of coolant trace across the span. On the suction surface downstream of the rows SS1 and SS2, the coolant traces were longer and distinct. Strong mainstream flow acceleration and greater amount of coolant flow from the suction side holes were responsible for this distribution. According to Goldstein et al [1], one possible reason for improved performance by shaped holes is the ‘Coanda effect’ that causes the jet to hug the surface. This effect, predominantly observed on a convex surface, produces higher effectiveness values on the suction side. The pressure side coolant traces, on the other hand, were much shorter in comparison. This could be attributed to relatively low pressure ratios (Fig. 3.6) leading to less coolant ejection and susceptibility of the ejected jet to lift-off owing to blade curvature. The traces begin to lengthen towards the trailing edge where the blade surface was flatter. Mhetras et al [17] also found similar coolant trace distribution with compound cylindrical cooling holes. However, a comparison of their effectiveness contours with the current study suggested that the higher momentum jet from cylindrical holes were more robust than shaped holes when enveloped by passage and tip leakage vortices. As a result, coolant emanating from compound cylindrical holes was maintained through a longer distance on the blade surface.

It is well known that the passage vortex drifts from the pressure-side leading edge towards the suction-side trailing edge of the adjacent blade and climbs on to the suction surface with an upwash motion [61, 62]. The tip leakage vortex, on the other hand, is a consequence of the interaction between the leakage flow and the suction-side wall flow and growing into a vortex as it exits the tip. Both the secondary vortices severely alter the coolant distribution on the blade surface. On the suction side of the blade, starting at $x/C_x \approx 0.3$, the spiraling motion of the passage and the tip leakage vortex carried the coolant towards the midspan, leaving the upper and lower corners of the blade aft unprotected. On the pressure surface, the corner vortices along the hub-blade interface created a downwash motion on the coolant whereas the coolant traces near the tip followed the tip leakage flow direction. Garg’s [10] computational results on a heavily film-cooled blade showed similar coolant streamline distribution on the suction and pressure sides.

The lateral expansion of 10^o on either side of the cooling hole helped spread the coolant out, as seen from the close spacing between traces in Fig. 3.7. The staggered arrangement of cooling holes also contributed partly to the close spacing between the coolant traces. Provision of 10^o forward expansion further helped the coolant to sit back on the surface. A prior study involving cylindrical holes (Mhetras et al. [53]) produced thinner coolant traces, suggesting that when everything else remains same, mixing losses are higher with cylindrical holes than with shaped holes.

Figure 3.8 is a plot of spanwise-averaged effectiveness versus normalized axial chord length for the pressure side (negative x-axis) and suction side (positive x axis) surfaces. The effect of average blowing ratio was studied for the no-wake case. The sharp peaks in the plot correspond to hole row positions. As seen, the effectiveness values kept increasing with blowing ratio on the pressure side. On the suction side, effectiveness increase began to stagnate at and above average blowing ratios of 0.9 suggesting that the higher coolant-to-mainstream pressure ratio for M=0.9 and 1.2 facilitated coolant lift-off and mixing with the mainstream. The pressure ratio on the pressure side was lower by 8% near cavity 1 and by 16% near cavity 2 (Fig. 3.6). Therefore, the effectiveness levels did not stagnate at higher blowing ratios. Overall, the effectiveness levels were higher on the suction side compared to that on the pressure side for the same average blowing ratio.

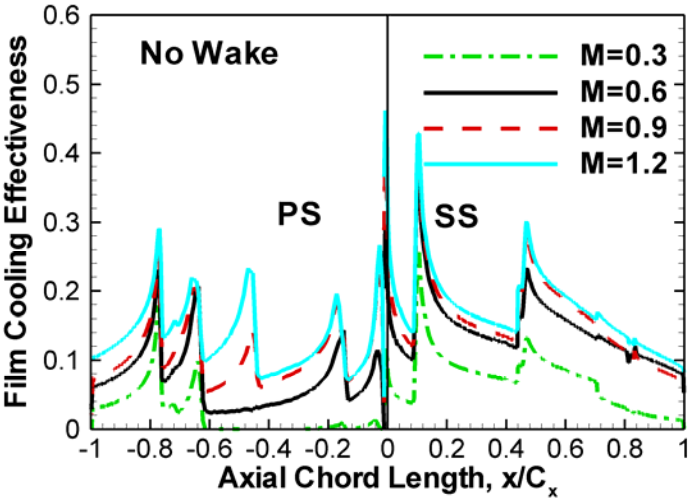

Fig. 3.8 Spanwise averaged film-cooling effectiveness distribution with no wake

The nature of influence exerted by the wake rod phase positions on effectiveness is shown in the contour plots presented in Fig. 3.9. As expected from the conceptual wake path diagram, 0% and 25% phase positions exhibited the highest degree of influence on film-cooling effectiveness. Vortex shedding from the wake rods brought additional turbulence in the mainstream, thereby thinning and shortening the coolant trace and in some cases producing spanwise non-uniformity (M=0.3). As seen from the plots, the rod induced turbulence could leave a good portion of the pressure side unprotected (PS1 and PS2 rows at M= 0.3, and PS2 row at M=0.6). Out of these two, 0% case produced more degradation of coolant trace on the pressure side. The downstream

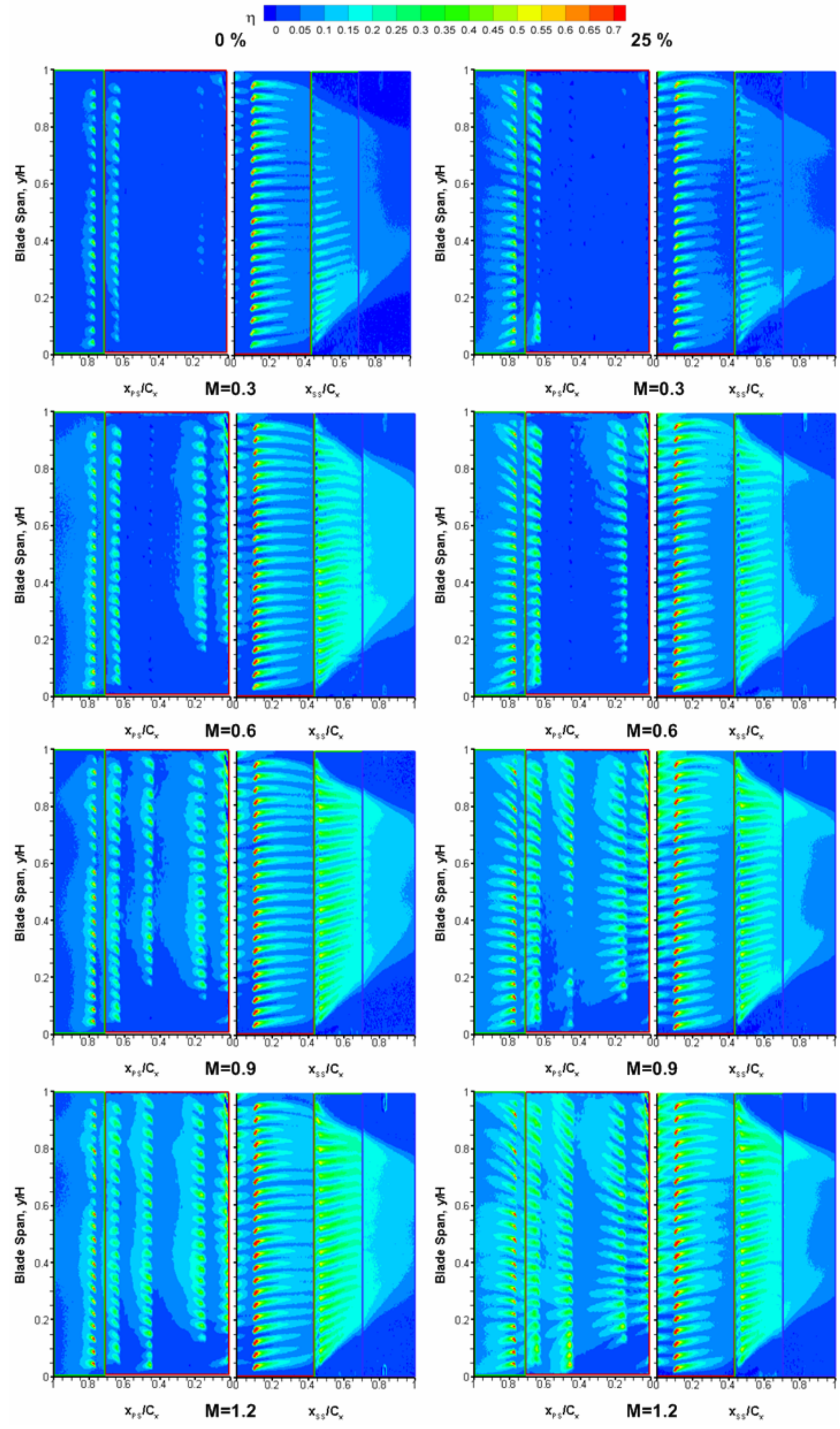

Fig. 3.9 Contour plots of film-cooling effectiveness distribution for two wake rod phases (0% and 25%) and all four average blowing ratios

propagation of the wake was evident from the short coolant traces near the PS4 row holes. On the suction side, the 25% phase position appeared to have relatively higher influence. Once again, the wake propagation along the suction surface could be gauged by the coolant trace degradation near the trailing edge, even at higher blowing ratios. Another notable observation could be made by looking at the suction side effectiveness contours at almost all blowing ratios for the 25% case. It appears that the secondary vortices shielded the coolant (SS2 row holes) to some extent from the incoming mainstream, as a result of which the coolant traces close to the tip and hub regions were able to propagate downstream in comparison to those near the midspan.

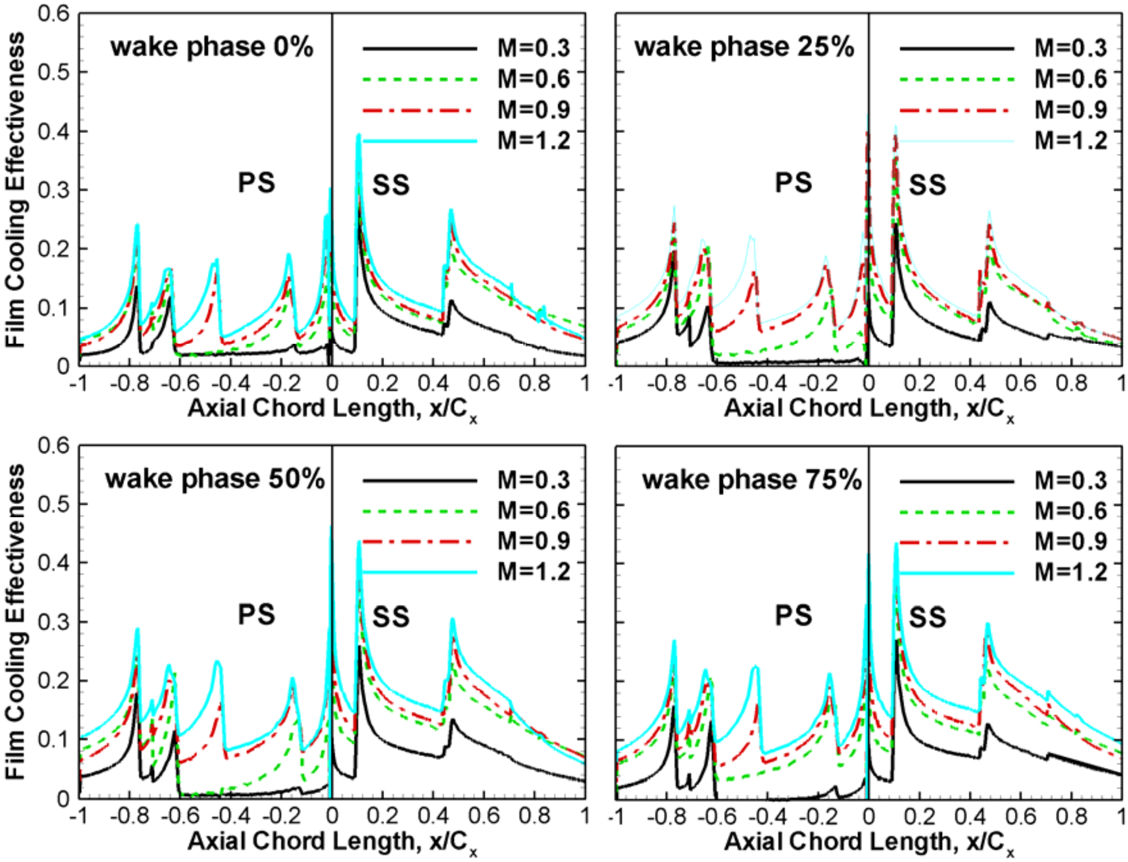

Fig. 3.10 Effect of blowing ratio on spanwise averaged film-cooling effectiveness

Figure 3.10 show the variation of spanwise-averaged film-cooling effectiveness with average blowing ratio at each of the four phase positions. The effectiveness trend was similar to the one for the no-wake case. There was a marked increase in effectiveness on the suction side as the blowing ratio was raised from 0.3 to 0.6, but the increase became steady thereafter. The pressure side effectiveness increase did not show such sign of saturation, however. At the lowest average blowing ratio, M=0.3, the pressure side effectiveness throughout 60% of the axial chord distance from the leading edge stayed close to zero in all four cases on account of higher surface pressure. The blade curvature and therefore the pressure were highest near the PS2 row. No coolant appeared from this row at M=0.3 and 0.6. At M=0.9, the appearance of peak in the PS2 row suggested that the cavity pressure was high enough to force the coolant out. The effectiveness peaks grew higher at the trailing edge row where the blade had the least curvature This was true for all average blowing ratios and phase positions. The suction side effectiveness peaks were always higher at the SS1 row than at the SS2 row for every blowing ratio and phase position. This was due to coolant accumulation on top of SS1 row from showerhead row (SH-SS) ejection. It is also likely that upstream ejection from SS-SH and SS1 rows was causing the mainstream

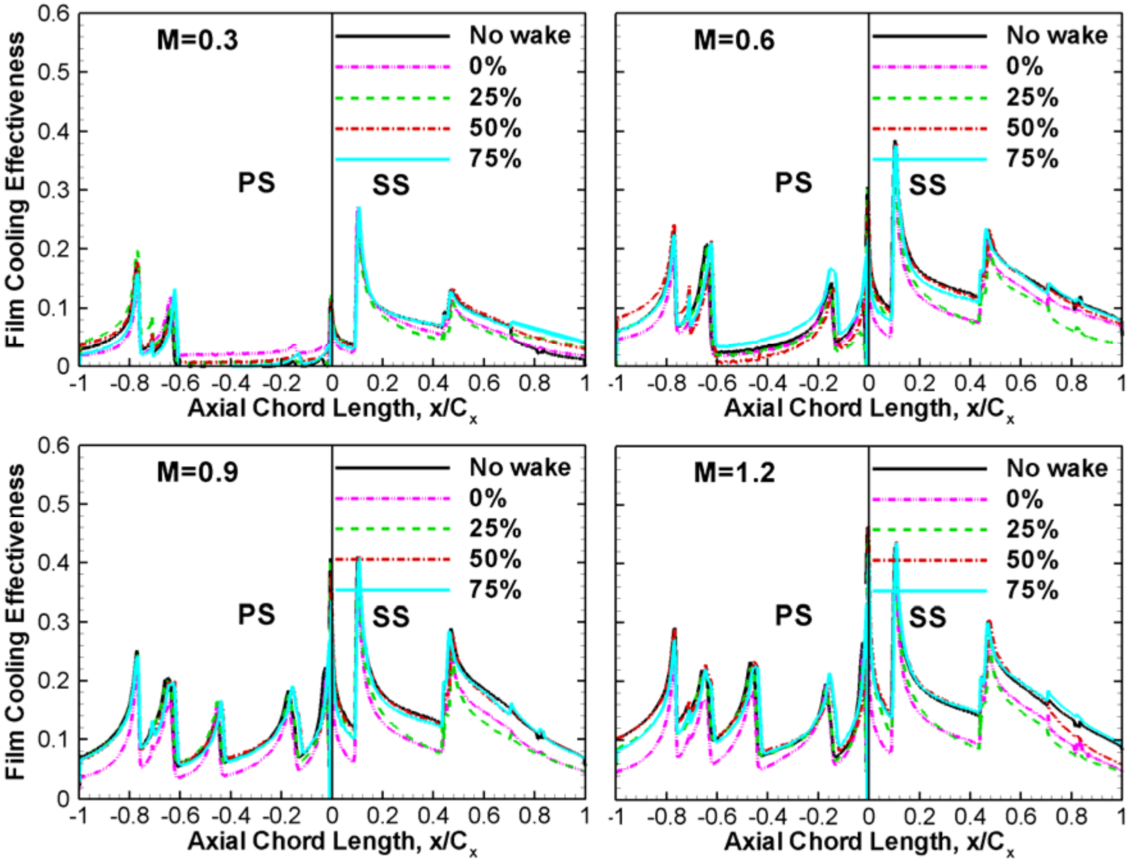

Fig. 3.11 Effect of wake rod phase positions on spanwise averaged film-cooling effectiveness

boundary layer to trip ahead of its natural transition, thereby diluting the coolant from the SS2 row holes. One other observation is that the effectiveness levels in the region between SS1 and SS2 rows at 0% phase position were bunched together compared to other phase positions, which shows that the wakes from 0% phase position had the greatest influence on effectiveness near the suction side leading edge, even at higher blowing ratios.

The spanwise-averaged effectiveness plots in Fig. 3.11 compare the effect of different phase positions. Except at M=0.3, the 0% case showed higher detrimental effect on the pressure side. Interestingly, the higher blowing ratios (M=0.9 and 1.2) showed higher degradation in effectiveness from the no-wake baseline case. On the other hand, on the suction side, both 0% and 25% produced equal reduction in effectiveness. This could be attributed to the relatively higher turbulent mainstream-coolant jet interaction. It may be pointed out that the wake rod effects in Fig. 3.11 nearly reflected the wake rod effects on the pressure ratio distribution shown

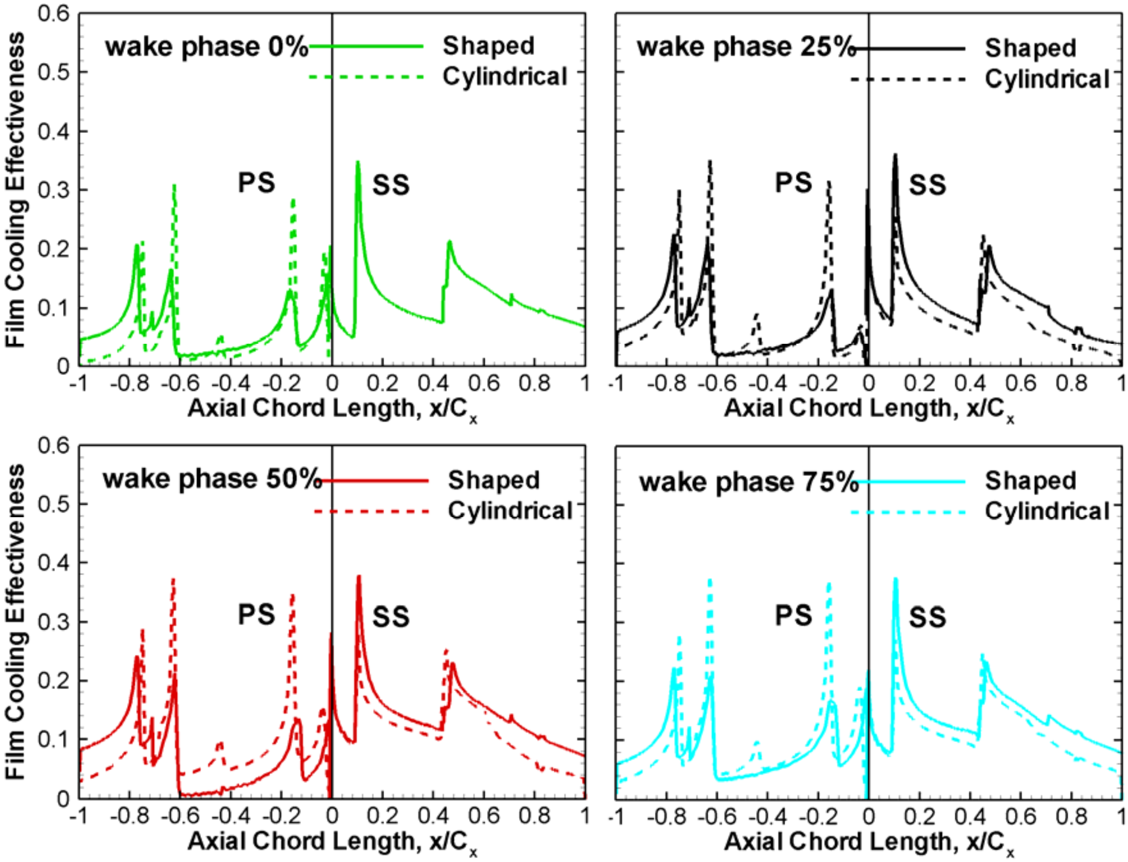

Fig. 3.12 Comparison of spanwise averaged film-cooling effectiveness distribution between compound angle shaped holes and compound angle cylindrical holes at M=0.6

earlier in Fig. 3.6.

A direct comparison of spanwise-averaged effectiveness distribution between the compound angle cylindrical hole blade examined by Mhetras et al. [53] and the compound angle shaped hole blade under study is made in Fig. 3.12 for all four wake rod phase positions. An average blowing ratio of 0.6 was used. Shaped holes clearly displayed higher film-cooling effectiveness than cylindrical holes along the entire suction side surface. On the pressure side, the results varied depending on the blade location – in the blade aft portion, where the surface is flatter, shaped holes performed better, whereas in the curved portion, the cylindrical holes fared marginally better than shaped holes.

4. TURBINE BLADE TIP FILM-COOLING

4.1 Introduction

Due to the pressure difference between the blade pressure and suction side, hot gas leaks through the gap between the blade tip and the shroud. This flow, called leakage flow, creates a thin boundary layer and consequently high heat transfer coefficient on the blade tip. The tip leakage flow is one of the major causes of blade tip failure. To reduce leakage flow and heat transfer on the tip, the modern gas turbines blades possess a recessed cavity on the tip with uniform cavity wall thickness. The cavity wall acts as a labyrinth seal that increases flow resistance and reduces the leakage.

Recently, many experimental studies for the squealer tip blade have been conducted in a cascade environment. Azad et al. [58, 59] studied the heat transfer on the first stage blade tip of an aircraft engine turbine (GE-E^3). They presented the effects of tip gap clearance and free-stream turbulence intensity level on the detailed heat transfer coefficient distributions for both plane and squealer tips under engine representative flow conditions. Azad et al. [60] also studied the effect of squealer geometry arrangement on gas turbine blade tip heat transfer and found that the location of the squealer rim could change the leakage flow and result in different heat loads to the blade tip. They also found that the suction side squealer provided best sealing to leakage flow among all the cases they studied. Kwak and Han [61, 62] presented heat transfer coefficients on the tip and near tip regions of both plane and squealer tip blades. They showed that the squealer tip could reduce heat transfer coefficients on the tip and near tip regions. Kwak and Han [63, 64] also studied heat transfer and film cooling effectiveness on both plane and squealer tip blades. Their results showed that the film cooling effectiveness on the squealer tip was much higher than that on the plane tip. Dunn and Haldeman [65] measured time averaged heat flux at a recessed blade tip for a full-scale rotating turbine stage at transonic vane exit conditions. Their results showed that the heat transfer coefficient (Nusselt number) at the mid and rear portion of the cavity floor is on the same order as the blade leading edge value. Yang and Diller [66] studied local heat transfer coefficients at several locations on a turbine blade tip model with a recessed cavity (squealer tip) in a stationary linear cascade. Papa et al. [67] measured average and local mass transfer coefficients on a squealer tip and winglet-squealer tip using the naphthalene sublimation technique. They also presented the flow visualization on the tip surface using an oil dot technique. Metzger et al. [68] and Chyu et al. [69] investigated heat transfer in a rectangular grooved tip model. They showed that the heat transfer in the upstream end of the cavity was greatly reduced compared to the flat tip, however, at the downstream of the cavity, the heat transfer levels for the grooved tip were higher due to flow reattachment inside the cavity. They also showed that the effect of the shroud velocity on the heat transfer coefficient was very small. Heyes et al. [70] studied tip leakage flow on plane and squealer tips in a linear cascade and concluded that the use of a squealer tip, especially a suction-side squealer tip, was more beneficial than a flat tip. Kim et al. [71] and Kim and Metzger [72] studied heat transfer and film cooling effectiveness using a 2-D rectangular tip model.

Researchers have also studied heat transfer on the plane tip blade. Mayle and Metzger [73], Metzger and Rued [74], Rued and Metzger [75] performed heat transfer studies using a simplified tip-simulated model. Metzger et al. [76] measured local heat flux using heat flux sensors in a rotating turbine rig with two different tip gaps. Bunker et al. [77] investigated the detailed heat transfer coefficient distribution on the blade tip surface using hue detection based liquid crystal technique. They measured the heat transfer coefficient at three tip gaps and two free-stream turbulence levels with both sharp and rounded edges. Bunker and Bailey [78] studied the effect of squealer cavity depth and oxidation on turbine blade tip heat transfer. They showed that the effect of cavity depth is not uniform over the entire tip cavity surface, but generally, a deeper cavity produced lower heat transfer coefficients. Their results also showed that blade tip heat transfer had low sensitivity to clearance gap magnitude. Teng et al. [79] measured the heat transfer coefficients and static pressure distributions of a turbine blade tip region in a large-scale low-speed wind tunnel facility using a transient liquid crystals technique. Rhee et al. [80] studied the local heat/mass transfer on the stationary shroud with blade tip clearances for flat tip geometry. They used the naphthalene sublimation method and concluded that the heat/mass transfer characteristics changed significantly with the gap clearance. Jin and Goldstein [81, 82] measured local mass transfer on a simulated high pressure turbine blade and near tip surfaces. They showed that the averaged mass transfer rate on the tip surface was much higher than that on the suction and the pressure surface.

Numerical studies to investigate blade tip heat transfer also have been conducted. Ameri and Steinthorsson [83, 84] predicted heat transfer on the tip of the SSME (Space Shuttle Main Engine) rotor blade. Ameri et al. [85] also predicted the effects of tip gap clearance and casing recess on heat transfer and stage efficiency for several squealer blade tip geometries. Ameri and Bunker [86] performed a computational study to investigate the detailed heat transfer distributions on blade tip surfaces for a large power generation turbine and compared the result with the experimental data of Bunker et al. [77]. Ameri and Rigby [87] also calculated heat transfer and film-cooling effectiveness on film cooled turbine blade models. Ameri [88] predicted heat transfer and flow on the blade tip of a gas turbine equipped with a mean-camber line strip. Numerical studies to investigate the heat transfer on the squealer tip blade also have been conducted by Ameri et al [89] and Yang et al. [90, 91].

Most of the above referenced studies focused on the heat transfer coefficient on the blade tip surface only. The present study applies a hue detection based transient liquid crystals technique to obtain the heat transfer coefficient on the tip surface, shroud, and near tip region of the blade pressure and suction side of the blade with a single or double squealer. This study provides comprehensive information about the heat transfer coefficient on the tip and near the tip regions with the single or double squealer blade tip. The effect of the squealer rim arrangement on the heat transfer coefficient is also presented. The results are compared with the plane tip and the double squealer tip results (Kwak and Han [61, 62]).

4.2 Experimental Facility

The blow-down facility, shown in Fig. 4.1, could maintain steady flow in the cascade for about 30 seconds. Compressed air stored in tanks entered a high flow pneumatic control valve, which could maintain steady flow by receiving downstream pressure feedback. The control valve could maintain a velocity within (3% of desired value. The cascade consisted of three blades with the center blade acting as the test blade, Fig. 4.2. The adjustment of adjustable sidewalls at the inlet and the exit allowed us to attain the design pressure distribution at the cascade inlet, on the three blades, and at the cascade exit. At the inlet side, the far-side wall (facing the blade suction side) was rotated outwards by few degrees for the mainstream to bleed into a half-passage in order to produce the design flow distribution on the guide and the test blade. Little or no adjustment of the near-side sidewall (facing the blade pressure side) was needed although a small bleed between the leading edge of the guide blade and the end of the sidewall was kept that ensured formation of fresh boundary layer on the guide blade. At the exit, the far-side wall was completely removed to obtain the downstream flow periodicity and the flow level required by the design. The other exit wall more or less followed the trailing edge direction of the guide blade. During the blow-down test, the cascade inlet and exit Mach numbers were 0.29 and 0.75, respectively. Overall pressure ratio (P_t/P) was 1.49 (where P_t is inlet total pressure and P is exit static pressure). Two pitot-tube probes were used- one was stationed $0.5C_{ax}$ upstream of the blade leading edge to determine the inlet Mach number and another at $0.5C_{ax}$ downstream of the blade trailing edge to determine the exit Mach number. To ensure flow periodicity at the inlet, 19 wall pressure taps (1mm dia., 12.7mm apart) were machined on the top cover of the cascade at a

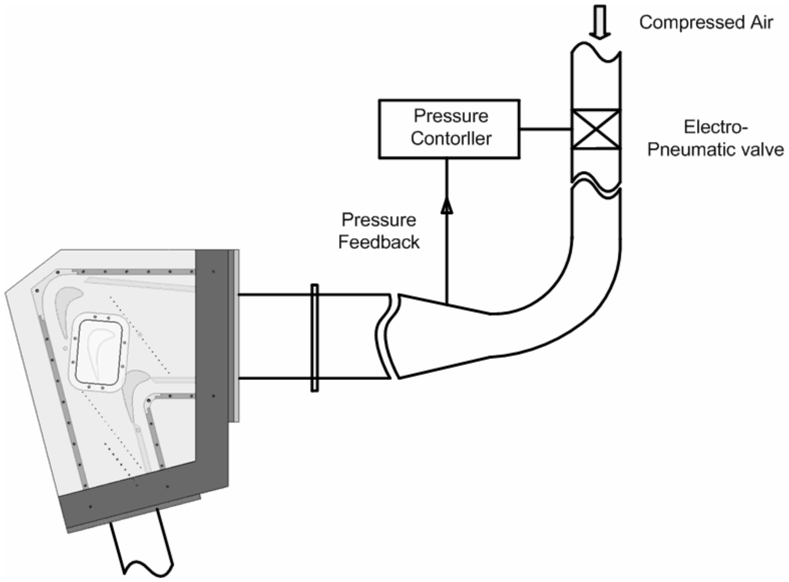

Fig. 4.1 Schematic of the blow-down facility with the test section

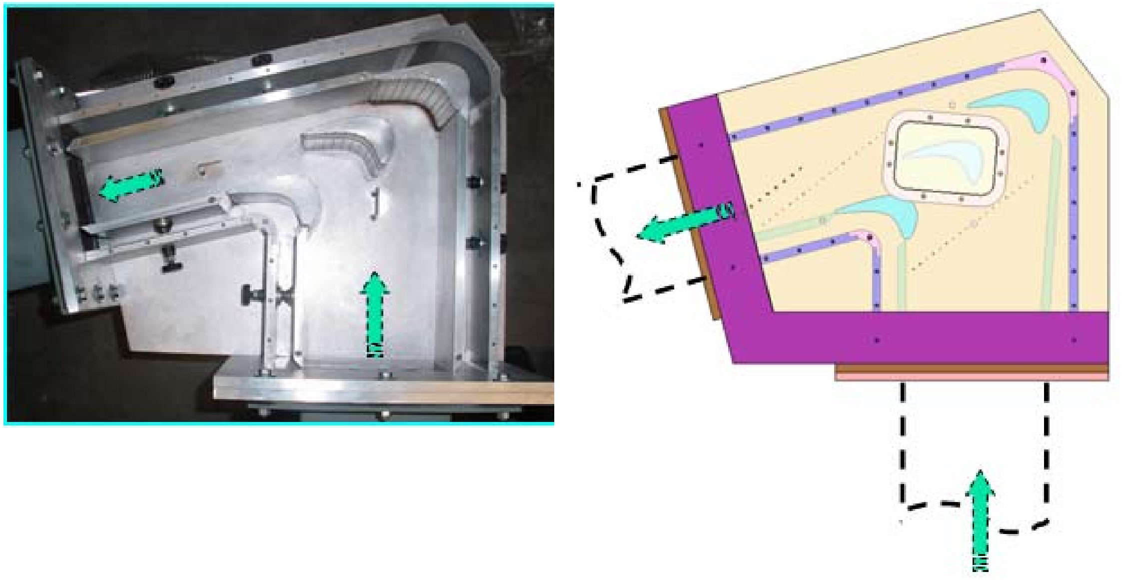

Fig. 4.2 Schematic of the test section

distance 0.5C_{ax} upstream of the blade leading edge along the blade row. Equal number of taps was machined 0.5C_{ax} downstream of the blade trailing edge to ascertain flow periodicity at the exit. Further, the test blade and the guide blades were also equipped with wall pressure taps at three span heights- 50%, 75%, and 95%. The periodicity obtained at the inlet and exit of the blade row is shown in Fig. 4.3. For the test blade, there were 29 pressure taps covering the entire pressure side, leading edge, and suction side at each of the three spans. For the far-side guide

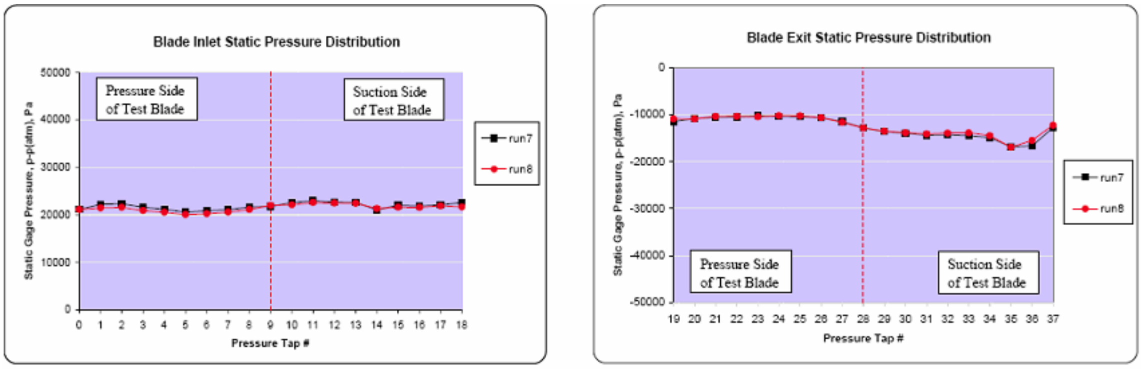

(a) (b)

Fig. 4.3 Flow periodicity in neighboring passages of the test blade (a) inlet (b) exit

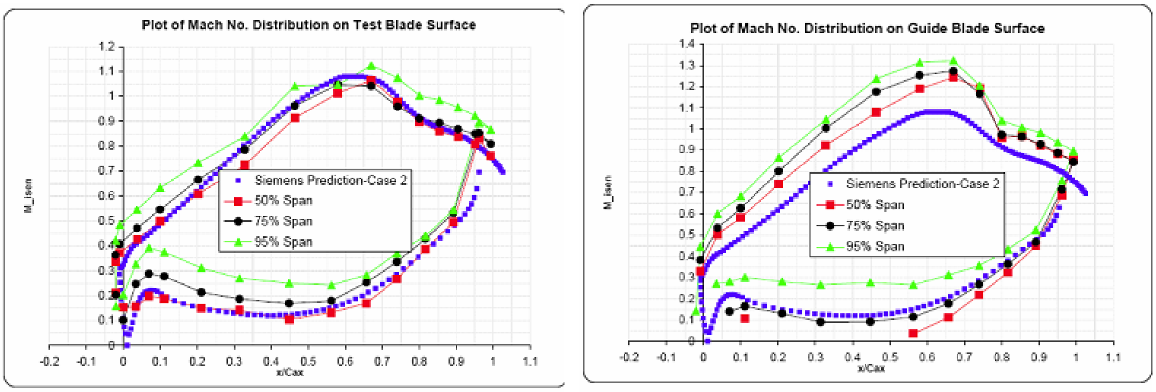

(a) (b)

Fig. 4.4 Mach number distribution around the blade surface (a) test blade (b) guide blades

blade, 16 taps covered the leading edge and pressure side at each of the three spans and for the near-side guide blade, 12 taps covered the leading edge and suction side, also at each of the three span locations. The test and guide blade pressure distributions are shown in Fig. 4.4.

In the combustor of a turbine engine, mixing between the mainstream air and the fuel produce high swirl and turbulence in the exiting mainstream air. The turbine stages, particularly those in the proximity of the combustor, encounter highly turbulent mainstream flow. To account for this effect, a turbulence generating grid was installed at a distance of 276.8mm from the leading edge of the test blade, Fig. 4.5. The turbulence grid was built out of 12.7mm thick aluminum by punching out 25.4mmx25.4mm square pieces in a 2-D array fashion, maintaining a distance of

Fig. 4.5 Turbulence generating grid at the inlet of the test section

12.7mm between the resulting square holes. A hot-film was placed at a distance of 220mm from the grid, which was roughly equivalent to 17 times the thickness of the grid, to measure the blade, shown in Fig. 4.6(a), had a span of 13.80cm and an axial chord length of 9.53cm. Since turbulence intensity. The test and the two guide blades were machined out of aluminum. The test the blades were placed in a linear cascade, they were machined for a constant cross-section for its entire span. The blade tip, Fig. 4.6(b), featured a 0.20cm thick and 0.25cm high rim around the edge except at the pressure side near the trailing edge. This particular type of rim design is called cut-back squealer rim. The cut-back feature allows trapped air to escape. This blade without any film-cooling holes was used as a baseline blade for comparison against the blade tip design that

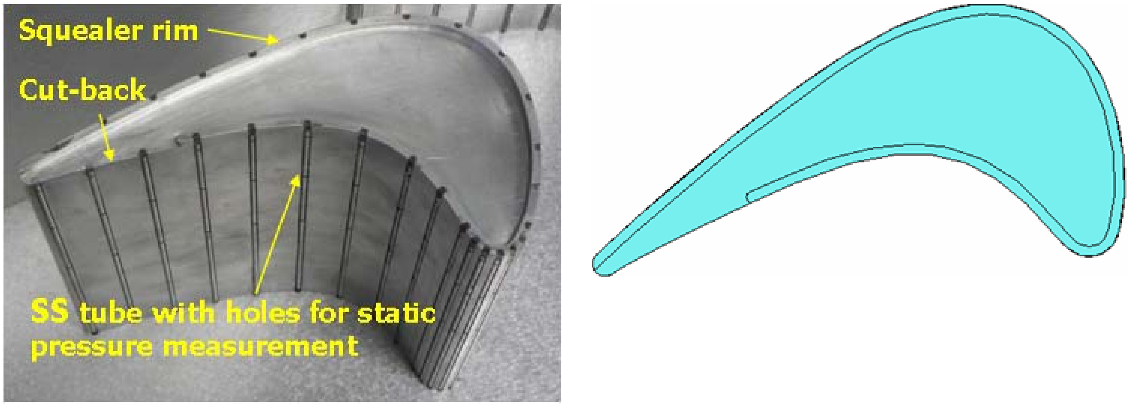

Fig. 4.6 (a) Test blade with surface pressure taps (b) Squealer rim blade tip

had film-cooling holes. A separate blade was designed that had a concept tip (suction side rail) and film-cooling holes. This blade was constructed using SLA (stereo lithography) technique because of complex internal coolant passages and film-cooling holes. The blade span was same as that of the baseline blade. The concept blade tip had a distinctly different rim design. The rim was tapered in shape, 0.35cm at the top and 0.17cm at the bottom. The bottom of the rim was offset from the edge by 0.25cm. The most notable difference was that the rim did not cover the pressure side of the tip surface except for a small portion at the leading edge. 30 shaped film-cooling holes tightly followed the rim on its inner side starting at about $0.3C_{ax}$ from the blade leading edge. 24 holes were provided on the pressure side near the tip, 6 on the suction side near the tip and close to the leading edge and 3 holes on the leading edge surface. As shown in Fig. 4.7, the blade was constructed in two parts- a core body that contained the coolant passages and the coolant plenum, and a removable top shell that contained the rim and the cooling holes. The coolant entered the blade from a single cylindrical passage of about 0.95cm diameter. The coolant after traveling half-way into the core body trifurcates into smaller cylindrical passages that ends up in the coolant plenum. Two sets of experiments were performed- one with all cooling holes open and

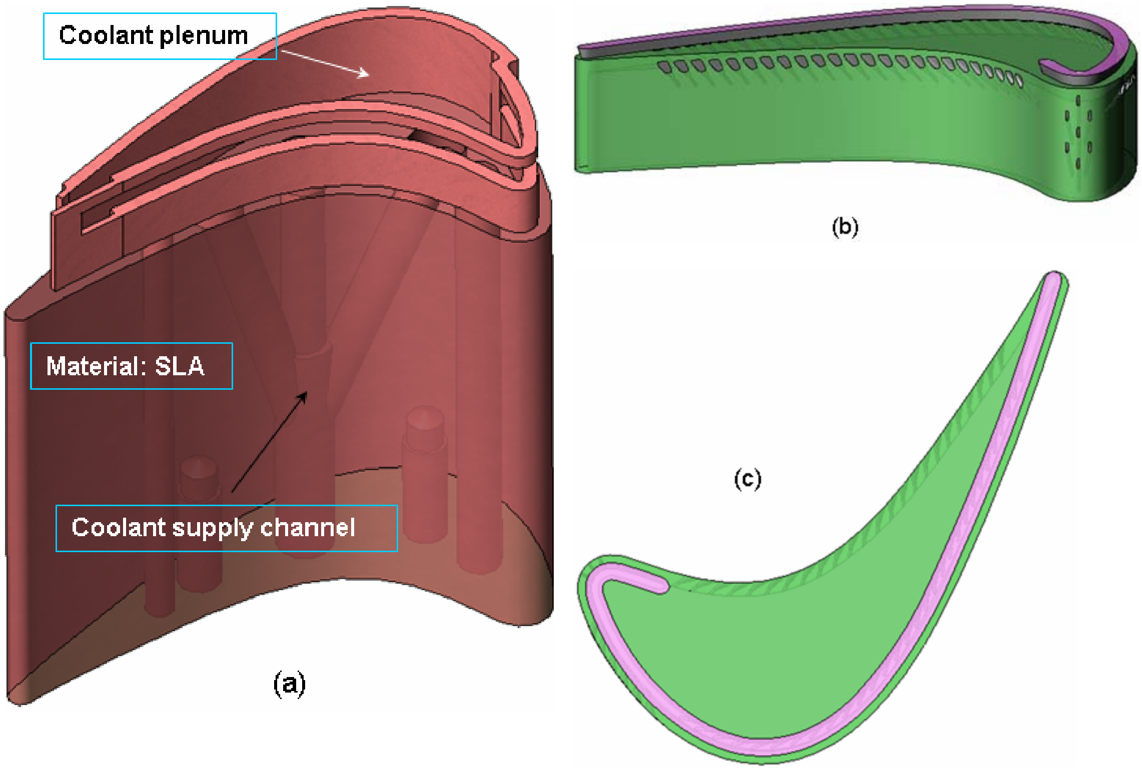

Fig. 4.7 (a) Test blade with surface pressure taps (b,c) Squealer rim blade tip shell

another with all the leading edge holes and 72% pressure side holes open. Experiments were performed with four different average blowing ratios (M) of 0.5, 1.0,1.5, and 2.0.

The film-cooling blade was used for heat transfer coefficient test as well. Near the top of the core body, a recess is made on the inside sidewall where a silicone heater in the shape of the blade tip could sit and heat the tip surface. The heater and its arrangement on the core body is shown in Fig. 4.8. The 0.5mm thick etched foil heater having a watt density of 35W/sq. inch

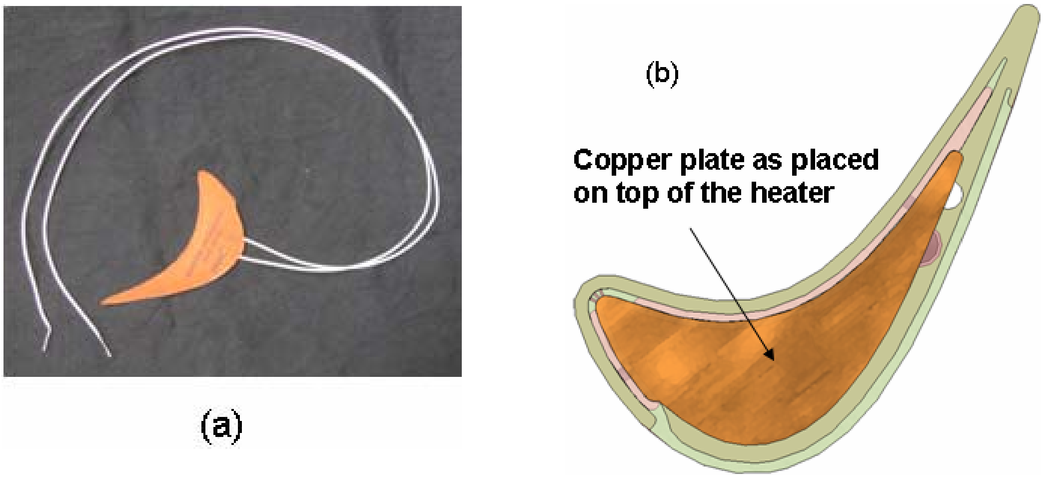

Fig. 4.8(a) Silicone Heater (b) Copper plate seating on top of the silicone heater

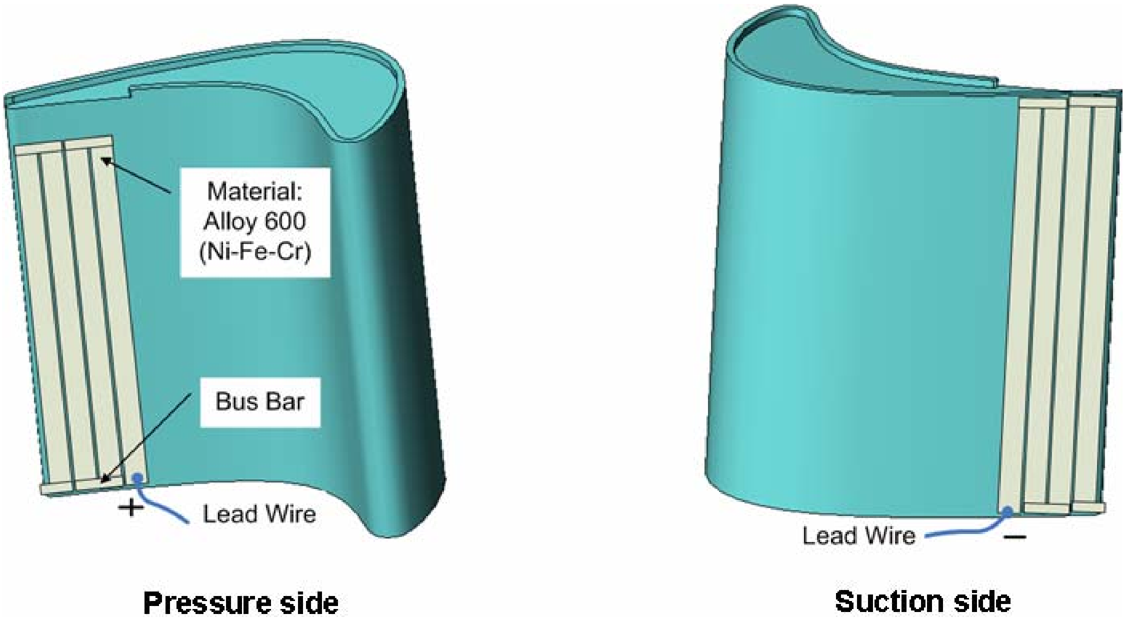

Fig. 4.9 Trailing edge thin foil heater

covered most of the tip except for the region close to the trailing edge. A copper plate also in the shape of the heater is attached between the heater and the underside of the tip surface for uniform heat distribution. To heat the trailing edge tip surface, a thin-foil heater (0.05mm thick Alloy 600) was attached on the span of the pressure and suction sides. There was in total eight foil strips of width 6.35mm and length almost the size of the blade span. The neighboring strips were serially attached by bus bars made of the same foil material, Fig. 4.9. Both the heaters were powered by individual variacs (120V, 3Amps, 0.4KVA max., Staco Energy, Type 291).

4.3 Pressure Loss

After adjusting the sidewalls to satisfy the design flow conditions at the blade inlet, exit, around the test and guide blades, and ensuring flow periodicity at the inlet and exit of the blade row, the first task was to carry out the pressure loss measurement for both the blade designs. The pressure loss was defined as:

$$\pi = \frac{P_{t,in} - P_{t,out}}{P_{t,in} - P_{s,out}} \tag{4}$$

The pressure loss could happen either due to wall friction or due to flow mixing between the secondary and the mainstream flow. From past studies, it is clear that the mainstream flow on the pressure side enters the clearance between the tip and the shroud and exits the other side developing a complex vortex system upon mixing with the mainstream flow. The amount of leakage across the clearance and the nature and strength of vortex formation is determined to a large extent by the blade tip design and the tip clearance itself. Therefore, both the tip designs were tested for three different tip gaps. Fig. 4.10 shows the comparison of the pressure loss maps. It must be pointed out that the near-side guide blade was not provided with any tip clearance because there was no flow on the pressure side of the blade to leak into the suction side. In the plot legend, higher the value, higher is the pressure loss. The upper three plots are for the baseline blade tip in the increasing order of tip gap. The dense color at the top of each plot confirms the fact that the losses are generated by the flow leaking through the tip clearance. The losses are also skewed towards the left half of the plots suggesting that the leakage vortex on the suction side of the blade growing bigger and bigger as it travels downstream. The highest loss region, as expected, is at the top left corner with values as high as 0.3. When the tip gap is increased, common sense would suggest that the tip leakage increases thereby producing increased losses. This happens when the tip clearance increases from 1.2mm to 2.2mm but stays more or less the

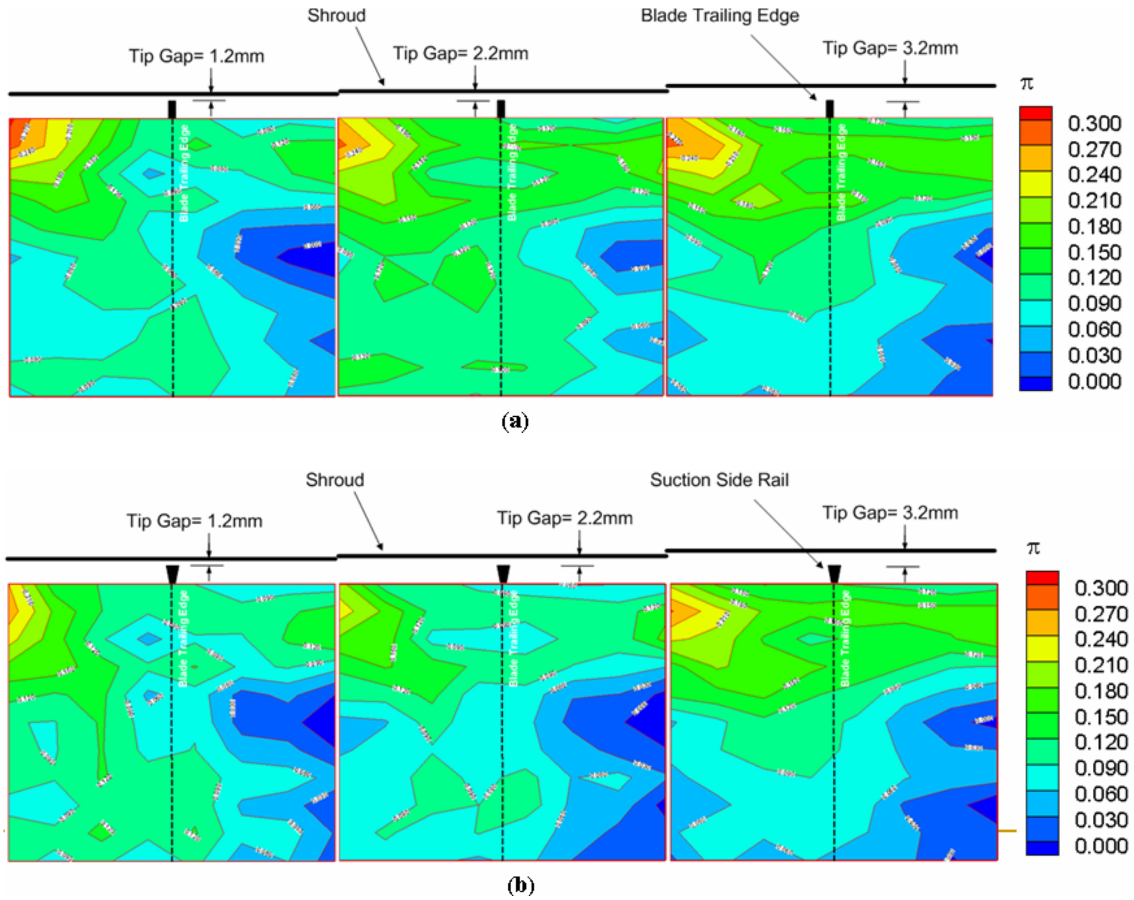

(a)

(b)

Fig. 4.10 Mainstream pressure loss at three different tip gaps (a) cut-back squealer tip (b) suction side rail tip

same when it is increased to 3.2mm. Looking at the bottom three plots for the concept tip blade, the lighter colors suggest lesser losses when compared with the upper plots. The suction side rail configuration can be said to be acting as a better seal against the leakage flow, which therefore creates lesser losses. However, it is not very clear what effect the tip clearance is having on the losses. It is possible on one hand to have a small-sized leakage vortex with a very strong core and on the other, a large-sized vortex but with depleted core strength, making it harder to access the effect of tip gap on pressure loss. One way is to area-average the losses for each tip gap and do a comparison. This is shown in Fig. 4.11. There is still no clear trend that can be seen except for the fact that the concept tip blade has lesser losses in comparison to the baseline blade for all three tip gaps. The area-averaged line plots show that there is almost no difference in losses at the lowest and highest tip gaps, but a significant difference exist for the middle tip gap.

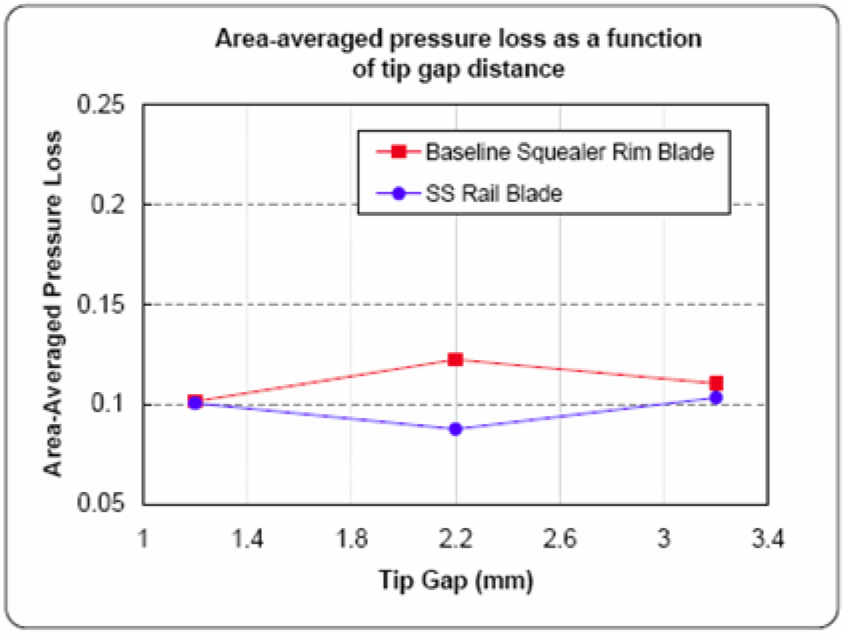

Fig. 4.11 Area-averaged pressure los as a function of tip gap for both tip configurations

4.4 Tip Pressure Distribution

The pressure distribution is plotted as the ratio of inlet total pressure normalized with the surface static pressure. The inlet total pressure is measured by a pitot probe positioned $0.5C_{ax}$ upstream of the test blade. The surface static pressure is obtained from PSP measurement in the absence of coolant flow. This ratio, in a way, is more representative of the flow velocity rather than the pressure, since higher value suggests higher velocity. Fig. 4.12 shows the pressure distribution for both blades and three tip gaps. Looking at the baseline blade, the lowest pressure is observed on the entire rim surface except on the leading one-third length of the suction side. The range of p_t/p value is between 2.5 and 3.0. With increase in tip clearance, there is increase in the cross-flow over the tip. Consequently, the cavity floor region, mainly in the vicinity of the pressure side rim, sees an increase in p_t/p ratio or a decrease in pressure. On the other hand, the highest pressure region for all three tip gaps is recorded in the cavity floor near the suction side rim close to the leading edge. This high pressure region is believed to be caused by a recirculating bubble that forms when mainstream flow passes over the leading edge and over to the suction side and gains strength with tip clearance. The concept blade tip also displays high ratio of low pressure on the rail, mainly on the downstream two-third length. In contrast to the baseline blade tip, the range of p_t/p lies between 2.0 and 4.0. On the tip floor, the high pressure zone from the

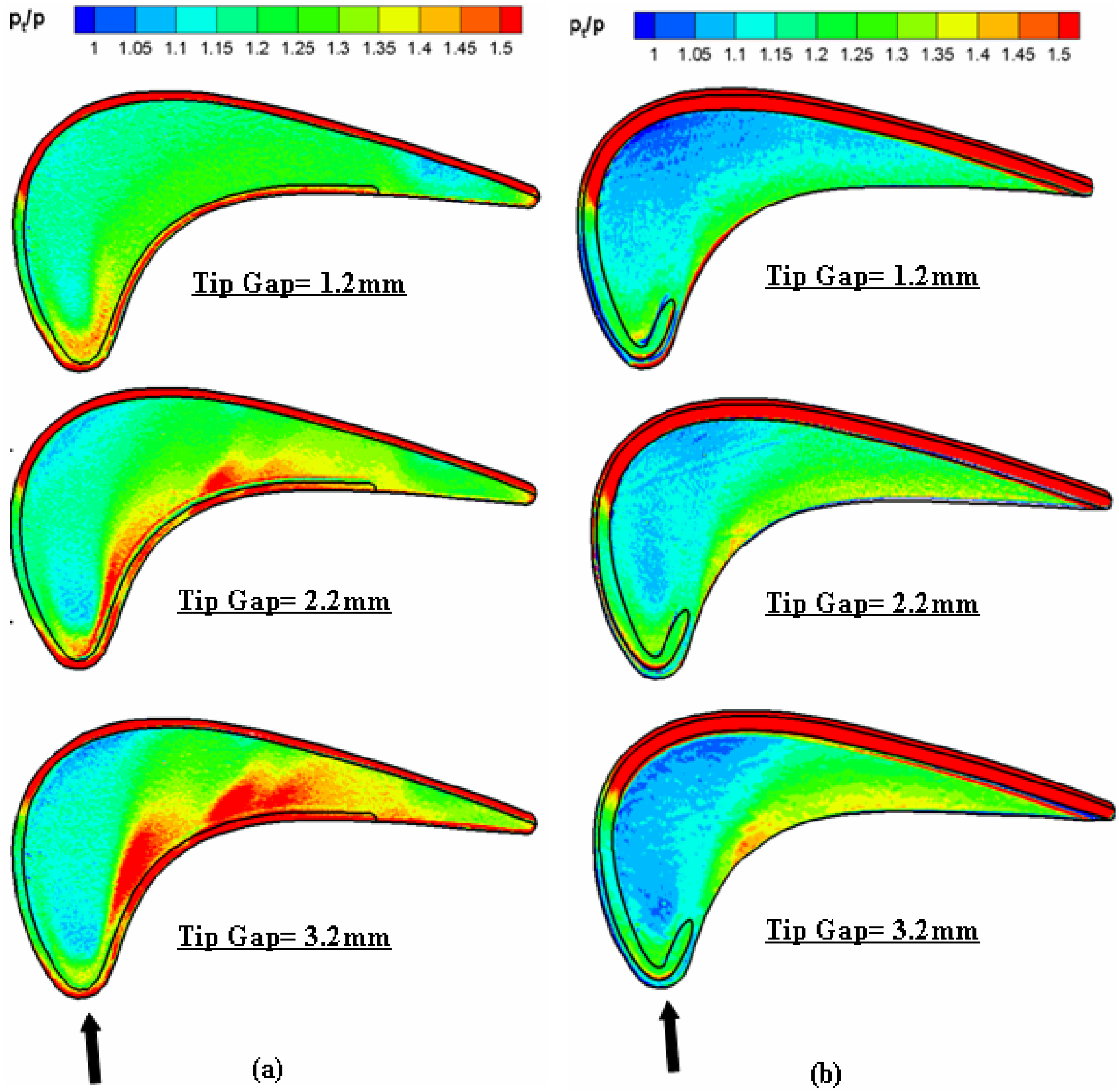

Fig. 4.12 Pressure ratio contours on the blade tip at three different tip gaps (a) cut-back squealer tip (b) suction side rail tip

bubble is larger and extends from the leading edge upto the trailing edge, but shifts towards the leading edge at increased tip clearances. Overall, the concept blade tip shows lower p_t/p ratio or higher pressure on the floor than the baseline blade tip.

The corresponding shroud pressure was measured by spraying PSP on the inside surface of the plexiglass window. The resultant plots are shown in Fig. 4.13. Unlike the tip surface, the flatter shroud surface allows the development of a thin boundary layer that creates less sharper pressure contours. However some prominent features seen earlier on the tip surface are observed

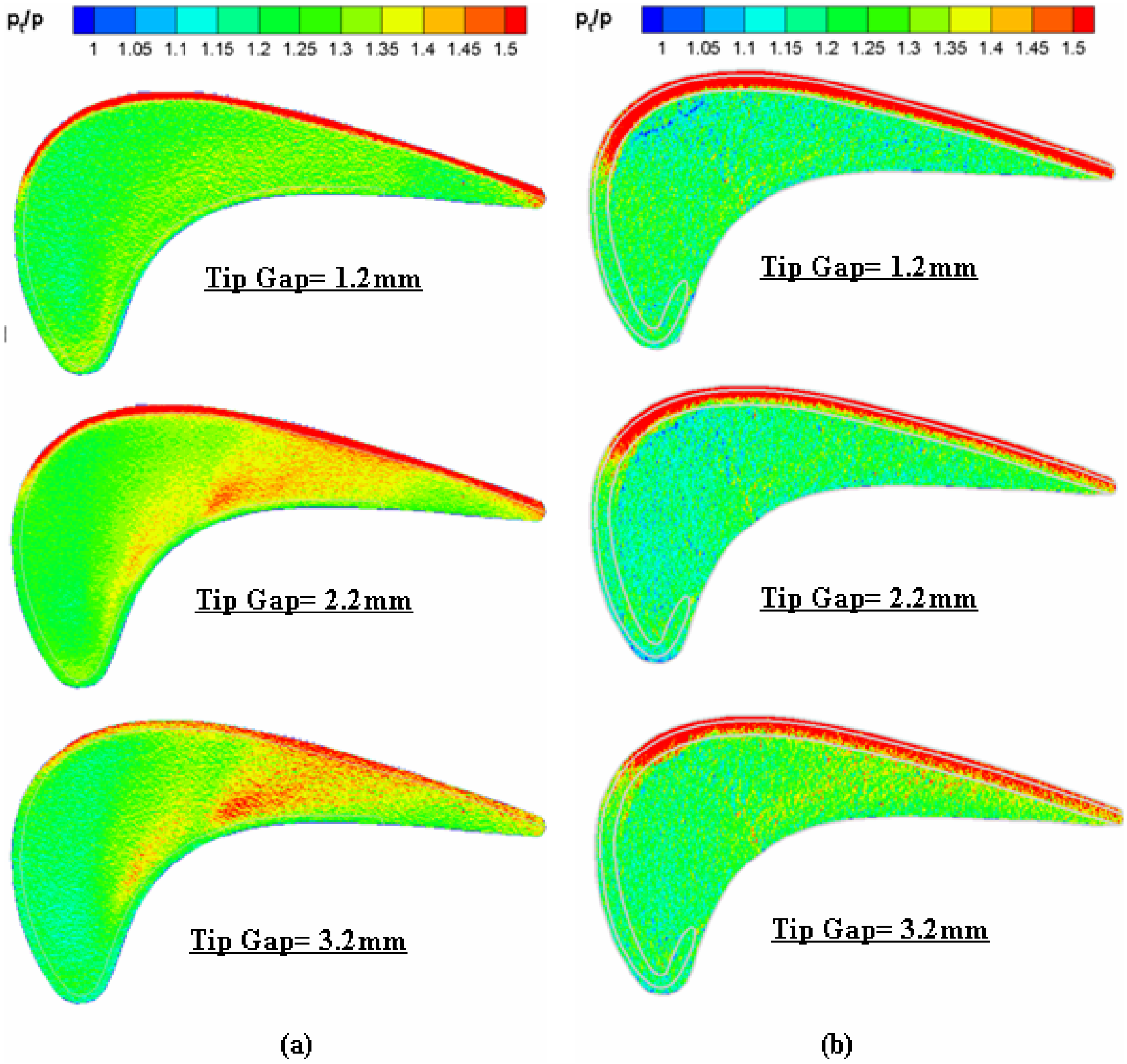

Fig. 4.13 Pressure ratio contours on the shroud at three different tip gaps (a) cut-back squealer tip (b) suction side rail tip

on the shroud as well. For example, the high p_t/p ratios on the rim for both tip designs stand out and so does the low pt/p ratio in the recirculation zones. For the baseline tip, some high p_t/p ratios are observed on the cavity floor as well.

4.5 Film-Cooling Effectiveness

Figure 4.14 shows the results of film-cooling effectiveness measurements on the tip surface with coolant delivery from all the cooling holes. Higher the value in the legend, higher is the degree of cooling. Note again that film-cooling study is done for the concept blade tip only.

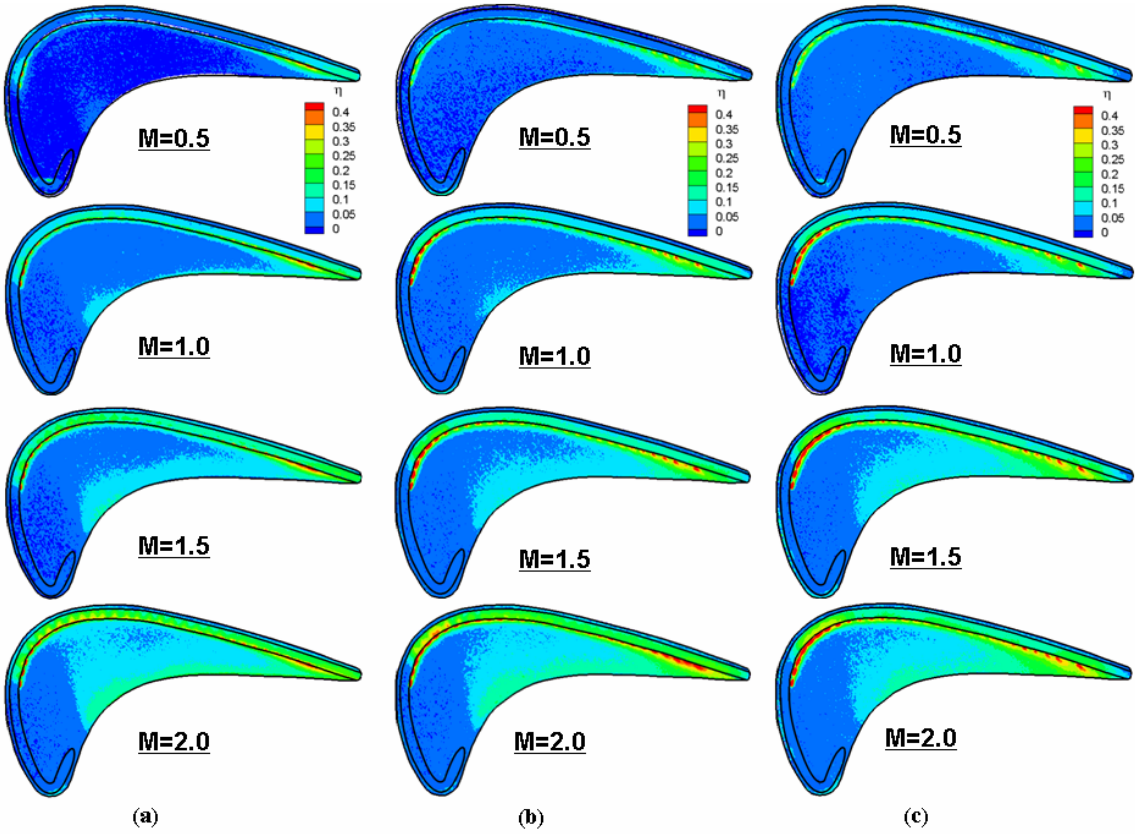

Fig. 4.14 Film-cooling effectiveness on the suction side rail blade tip with all cooling holes open

Starting with the tip gap of 1.2mm, it can be seen that the coolant coverage increases with the blowing ratio. The cooling holes tucked under the suction side rail are carried over the rail surface by the mainstream leakage flow. Barring the lowest blowing ratio, others show quite good film coverage. At higher blowing ratios, the carried over coolant do provide some coverage to the floor of the suction side downstream. The portion of the rail not covered by coolant does not have cooling holes underneath it and so remain bare. Recall that the pressure contours also displayed very low p_t/p ratios or low high velocities in that region of the rail (which should mean lower heating) and therefore the current layout of cooling holes under the rail seem reasonable. These cooling holes, however, do not seem to be helping in covering the cavity floor region, even in its immediate vicinity. This is mainly due to the fact that the coolant emanating from the cooling holes, located right near the root of the rail, is pushed over the top of the rail by the leakage flow on to the suction side of the blade. Coolant coverage from the pressure side holes can also be seen to be getting larger and larger with blowing ratio. At the lower two blowing ratios, coolant is hardly seen on the cavity floor. As the blowing ratio becomes higher, the mainstream leakage flow pushes the coolant on to the cavity floor and further downstream. The level of effectiveness which is highest at about 0.2 near the pressure side edge dies down to about 0.05 as it reaches the suction side rail. A big portion of the cavity floor close to the leading edge still remains uncovered. The suction side and leading edge cooling holes did not show much benefit in terms of cooling this portion since only a small amount of coolant can be seen on the leading edge rail and that too at the highest blowing ratio. There appears to be an accumulation of coolant from the tip and the pressure side holes near the trailing edge and hence a region of high effectiveness, with effectiveness getting higher with blowing ratio. All these features are observed for the other two tip clearances of 2.2 and 3.2mm. However, the film coverage shows marginal improvement as the tip clearance is increased.

When coolant is supplied from a common plenum, the coolant exit from the cooling holes is determined by the external mainstream flow around the cooling holes. Thus more coolant exits from tip holes compared to pressure side holes because of higher pressure exerted by the mainstream flow on the latter holes. To eliminate this bias, separate plenums can be constructed for cooling different regions of the blade. For instance, one plenum can supply coolant to leading edge holes, another to pressure side holes, yet another to suction side holes, and so on. In this study, 17 holes on the pressure side and all holes on the leading edge were kept open and rest all holes were sealed off. Thus, in the absence of the other holes, the pressure side holes were fed by a single plenum. This allows us to observe the film-coverage from the pressure side and leading edge holes only. The results are shown in Fig. 4.15. For all the tip clearances, there is an increase in film coverage with pressure ratio. The level of effectiveness is highest at the edge of the pressure side which gradually drops as the coolant is transported down towards the suction side rail. The effect of tip clearance is to decrease the coolant coverage and the level of effectiveness due to increased leakage flow.

4.6 Tip Leakage

The percentage of mainstream flow entering the passage that leaks through the tiny tip clearance is a function of the tip clearance, besides many other factors. To quantify this leakage, a simple model based on orifice flow has been developed. The mass flow through an orifice is given as:

$$\dot{m}_{\mathrm{hole}} = C_D\left(\frac{\pi}{4}d^2\right)\left(P_{t,\mathrm{cavity}}\left(\frac{P_{\mathrm{blade}}}{P_{t,\mathrm{cavity}}}\right)^{(\gamma+1)/2\gamma}\right)\sqrt{\frac{2\gamma}{(\gamma-1)RT_c}\left(\left(\frac{P_{t,\mathrm{cavity}}}{P_{\mathrm{blade}}}\right)^{(\gamma-1)/\gamma}-1\right)} \tag{5}$$

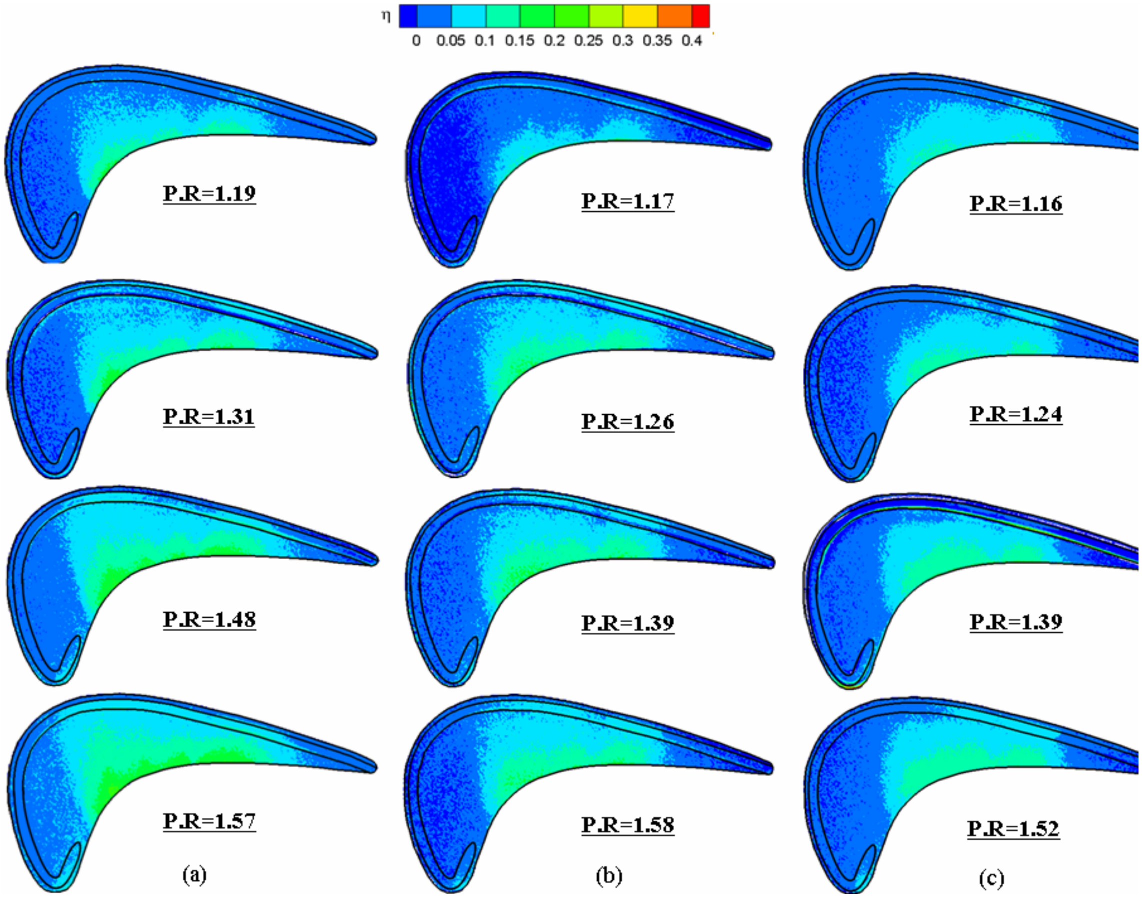

Fig. 4.15 Film-cooling effectiveness on the suction side rail blade tip with only zone I cooling holes open

The tiny clearance of the tip together with the sharp entrance region of the pressure side edge is assumed to behave like an orifice. Making this assumption, a differential of Eq. 5 is taken on both sides leading to the equation for leakage flow.

$$d(\dot{m}_{hole}) = C_D[dA]\left(P_{t,inlet}\left(\frac{P_{blade}}{P_{t,inlet}}\right)^{(\gamma+1)/2\gamma}\right)\sqrt{\frac{2\gamma}{(\gamma-1)RT_c}\left(\left(\frac{P_{t,,inlet}}{P_{blade}}\right)^{(\gamma-1)/\gamma}-1\right)}$$

$$\dot{m}_{hole} = \int_0^{C_{AX}}\left\langle C_D h_{gap}\left(P_{t,inlet}\left(\frac{P_{blade}}{P_{t,inlet}}\right)^{(\gamma+1)/2\gamma}\right)\sqrt{\frac{2\gamma}{(\gamma-1)RT_c}\left(\left(\frac{P_{t,inlet}}{P_{blade}}\right)^{(\gamma-1)/\gamma}-1\right)}\bullet dX\right\rangle$$

$$\dot{m}_{hole} = \int_0^{C_{AX}}\left\langle R(X)\bullet dX\right\rangle \tag{6}$$

In the above equation, C_D is the discharge coefficient h_{gap} is the tip gap, $p_{t,inlet}$ is the total pressure at the blade inlet, and $p_{s,inlet}$ is the tip static pressure. The value of $p_{t,inlet}$ remains constant irrespective of the tip clearance while $p_{s,inle}$ is extracted from the pressure side rim with the blade axial chord lined up in the x-direction. Fig. 4.16 shows the results of the tip leakage as a function of tip clearance for both blades. The tip gap is measured from the rim top to the shroud. The baseline blade tip shows a monotonic increase in tip leakage with tip clearance. The concept blade tip in absence of cooling also shows a similar monotonic increase with tip clearance but lower in comparison to the baseline blade tip case. With film-cooling, the leakage is lower than both no film-cooling cases at tip gaps 1.2mm and 2.2mm and lie in between the two blade tips at tip gap of 3.2mm. At the smallest and largest tip gaps, there is no apparent effect of blowing ratio on leakage. However at tip gap=2.2mm, the blowing ratio did show some effect although the trend is not very clear.

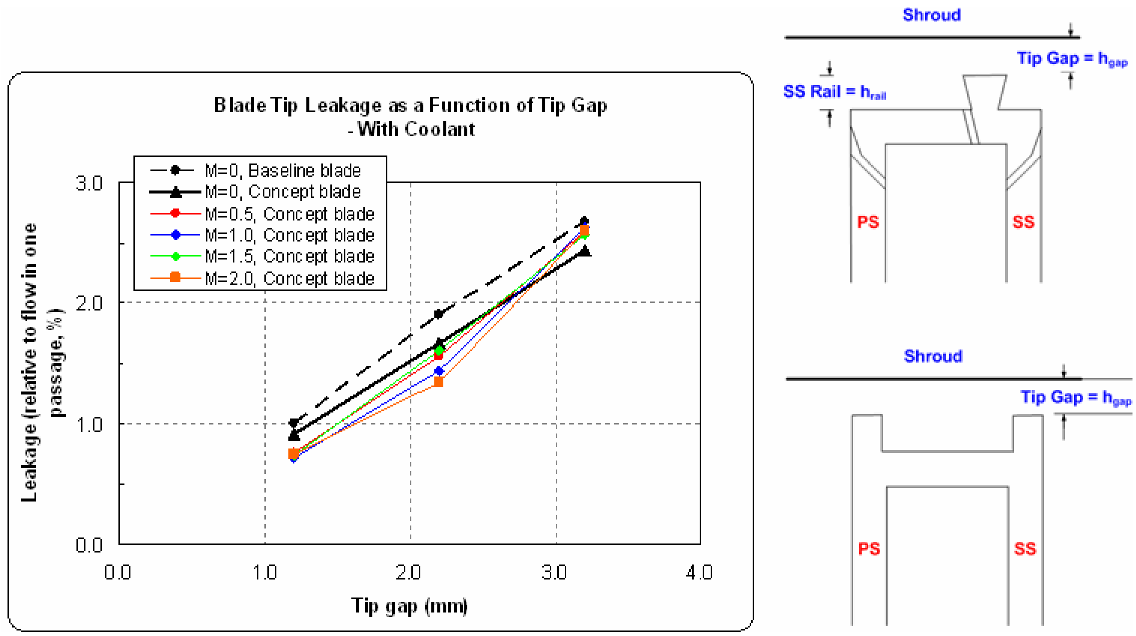

Fig. 4.16 Tip leakage as a function of tip gap

4.7 Heat Transfer Coefficient on the Blade Tip

TSP method also served as the tool for measuring the tip surface temperature that was used to deduce the heat transfer coefficient. Note that the blade tip material (polycarbonate) has a low thermal conductivity of 0.47W/m K. The test duration is smaller (10-30 sec) than the time required for the temperature to penetrate the full thickness of the blade tip material. Thus a 1-D transition, semi-infinite solid assumption is valid throughout the surface, except near the tip edges. The local heat transfer coefficient over a TSP coated surface can be obtained using a 1-dimensional semi-infinite solid assumption with convective boundary condition at the test surface.

$$k\frac{\partial^2 T}{\partial x^2} = \rho c_p \frac{\partial T}{\partial x} \tag{7}$$

$$\text{at } t = 0, T = T_i \tag{8}$$

$$\text{at } x = 0, -k\frac{\partial T}{\partial x} = h(T_W - T_m); \text{ as } x \to \infty, T = T_i \tag{9}$$

The solution for the above 1-D transient conduction equation at the surface (x=0) is:

$$\frac{T_W - T_i}{T_m - T_i} = 1 - \exp\left(\frac{h^2 \alpha t}{k^2}\right)\operatorname{erfc}\left(\frac{h\sqrt{\alpha t}}{k}\right) \tag{10}$$

By knowing the initial temperature (T_i) of the test surface, the mainstream (recovery) temperature (T_m) at the cascade inlet and the color change temperature (T_w) at time t, the local heat transfer coefficient (h) can be calculated from Equation (9).

The blade tip was heated slowly until the blade tip temperature was in the range of 60°C-70°C. Two thermocouples-one mounted below the SLA heater support plate and another mounted outside the tip on the pressure side- served as guides when heating up the blade tip. The initial tip temperature (T_i) is shown in Fig. 4.17. As soon as the blade reached the pre-set thermocouple temperatures, the heaters were switched off and the mainstream air was let in. The flow pressure history recorded just upstream of the blades is shown in Fig. 4.18. The initial rise time of the flow is around 3 seconds, thereafter the flow is stable. This is not a true step change in flow that is desirable for a transient heat transfer experiment. Therefore, a correction was made by deducting 3 seconds from the time each pixel on the tip took to reach the pre-set value of T_w. The mainstream temperature was kept at a constant value of 20°C although the true representative of mainstream flow temperature is the adiabatic surface temperature. The changing nature of the

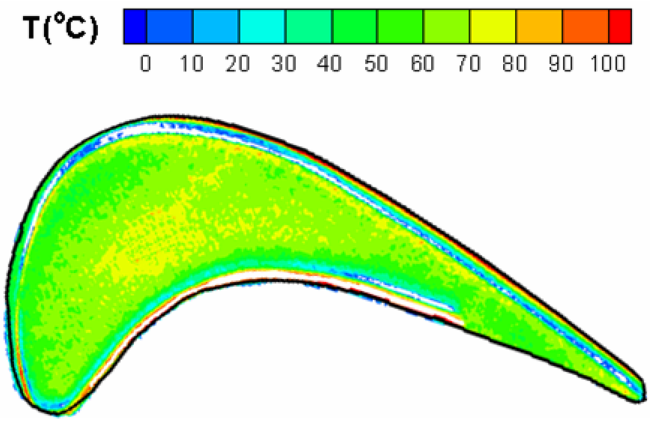

Fig. 4.17 Tip initial temperature before mainstream entry

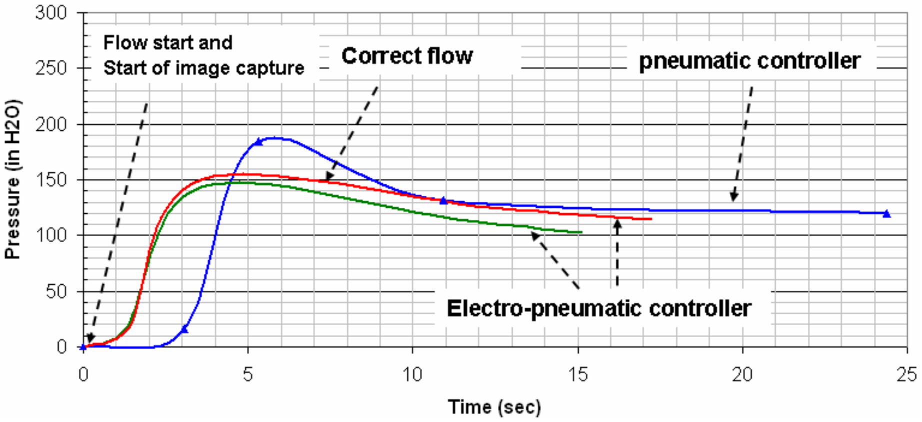

Fig. 4.18 Flow history in the cascade

surface temperature would also call for a transient value of thermal conductivity of the tip material while calculating the heat transfer coefficient. However, in the present calculations, this scenario was not accounted for and a constant thermal conductivity of 0.47 W/m-K (20°C) was used. Figure 4.19 (a) shows the heat transfer coefficient contour plot on the cut-back squealer rim blade tip obtained from experiment. Figure 4.19 (b) shows the numerical result obtained from CFD for the same blade tip and flow conditions. Both plots show region of high heat transfer in the region close to the leading edge pressure side. Whereas the CFD plot show a distinct elliptical region of high heat transfer, the experiments did not reveal such a clear region of high heat transfer. The occurrence of high heat transfer region near the leading edge is due to flow impinging on the tip after detaching from the leading edge rim. Two additional regions of high

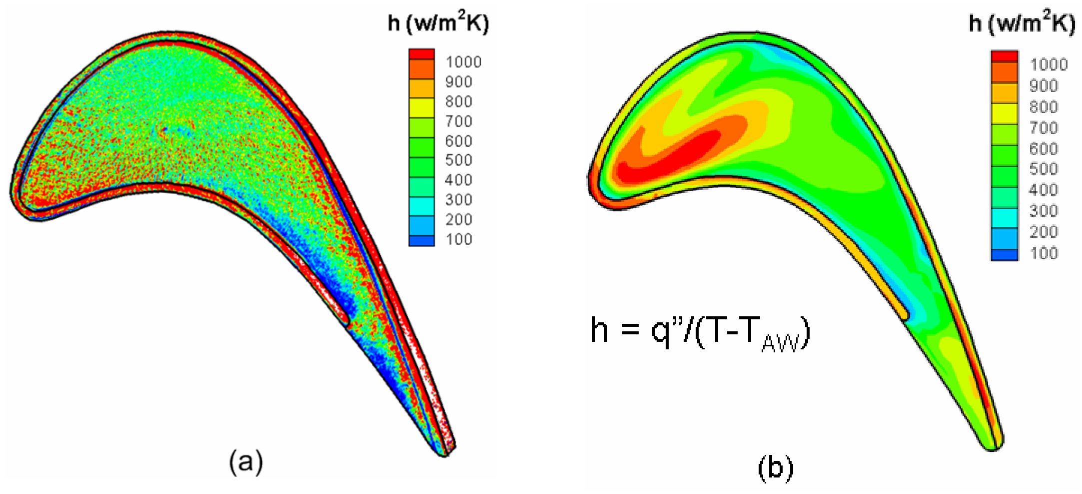

Fig. 4.19 Heat transfer coefficient on the blade tip (a) experiment (b) CFD

heat transfer were also observed near the trailing edge but only one in the case of CFD. Two low heat transfer regions were observed both in experiment and CFD. One of them was near the suction side rim at the highest curvature region and another just beside the end of the pressure side rim. One additional low heat transfer spot opposite to the second low heat transfer region in CFD, however, did not appear in the experiment. The low heat transfer regions are due to flow recirculation bubbles that are generated close to the rim edges. The overall levels of heat transfer coefficient measured were less than that of CFD by around 20%.

5. SUMMARY

Blade Platform Film-Cooling Effectiveness

1) The platform was effectively cooled with stator-rotor purge flow combined with the downstream discrete-hole cooling.
2) The shaped holes produced wider film coverage and higher effectiveness levels than the cylindrical holes. The effectiveness for the shaped holes increases with increase of the average blowing ratio (M=0.5~2.0), whereas an optimal blowing ratio of 1.0 exists for the cylindrical holes.
3) The two-row or four-row layout didn't show much difference in laterally-averaged effectiveness. However, the local effectiveness distribution, which determines the thermal stress and hotspots etc, varied with the layout.
4) The shaped holes also exhibit lower aerodynamic loss.
5) Higher the freestream turbulence, lower was the effectiveness.
6) The effect of increasing the purge flow rate was to increase the coolant coverage downstream of the slot. There was a significant improvement in effectiveness when the purge flow rate was increased from 0.25% to 0.5%, beyond that the improvement was little.
7) With coolant-to-mainstream density ratio of 1.8, an optimum blowing ratio of 1.5 was obtained for discrete film holes. Note that with a low coolant-to-mainstream density ratio of 1.0, the optimum blowing ratio was 1.0.
8) Higher coolant-to-mainstream density ratio resulted in higher effectiveness levels from the cooling holes. However, for the purge flow, the effect was reversed in the region between the slot and the blade leading edge.

Blade Span Film-Cooling Effectiveness

1) The compound angle, laidback fan-shaped holes produced uniform, wide, and close-spaced coolant coverage on the blade surface.
2) At any given blowing ratio, the suction side showed better coolant coverage than the pressure side even though the former had two fewer rows of holes.
3) Film-cooling effectiveness increased with blowing ratio on both side of the blade. Whereas the pressure side effectiveness continued to increase with blowing ratio, the increase in suction side effectiveness slowed down at higher blowing ratios (M=0.9 and 1.2).

4) At low average blowing ratios (M=0.3 and 0.6), the suction side effectiveness was much higher than that on the pressure side. At higher average blowing ratios (M=0.9 and 1.2), this difference became narrow.
5) Pressure sensitive paint (PSP) technique enabled us to clearly visualize the passage and tip-leakage vortex induced coolant trace distribution over the blade surface.
6) Upstream wake had a detrimental effect on film coverage. 0% and 25% wake phase positions significantly decreased film-cooling effectiveness magnitude. Wakes from 50% and 75% phase positions did not adhere to the blade surface and hence did not impact film-cooling effectiveness as much.
7) Comparison between the compound shaped hole and the compound cylindrical hole design showed higher effectiveness values for shaped holes on the suction side. The cylindrical holes performed marginally better in the curved portion of the pressure side.

Blade Tip Film-Cooling Effectiveness

1) Film coverage on the blade tip increased with blowing ratio and tip gap
2) The current cooling hole design did not provide any significant coverage on the leading portion of the tip floor and the rim
3) For the baseline tip, zones of high heat transfer were seen near the LE and TE
4) The area-averaged mainstream pressure loss was higher for the baseline blade tip by over 40% at tip gap of 2.2mm
5) The tip leakage was higher from the concept tip than from the baseline tip. Cooled concept tip lowered the leakage further except at tip gap of 3.2mm

REFERENCES

[1] Langston, L.S., 2001, "Secondary Flows in Axial Turbines – A Review," Annals of the New York Academy of Sciences, **934**, pp. 11-26.

[2] Langston, L.S., Nice, L.M., and Hooper, R.M., 1976, "Three-Dimensional Flow Within a Turbine Cascade Passage," ASME Paper No. 76-GT-50.

[3] Langston, L.S., 1980, "Crossflows in a Turbine Cascade Passage," ASME J. Engineering for Power, **102**, pp. 866-874.

[4] Chyu, M.K., 2001, "Heat Transfer Near Turbine Nozzle Endwall," Annals of the New York Academy of Sciences, **934**, pp. 27-36.

[5] Simon, T.W., and Piggush, J.D., 2006, "Turbine Endwall Aerodynamics and Heat Transfer," AIAA J. Propulsion and Power, **22**, pp. 310-312.

[6] Takeishi, K., Matsuura, M., Aoki, S., and Sato, T., 1990, "An Experimental Study of Heat Transfer and Film Cooling on Low Aspect Ratio Turbine Nozzles," ASME J. Turbomachinery, **112**, pp. 488-496.

[7] Harasgama, S.P., and Burton, C.S., 1992, "Film Cooling Research on the Endwall of a Turbine Nozzle Guide Vane in a Short Duration Annular Cascade: Part 1 – Experimental Technique and Results," ASME J. Turbomachinery, **114**, pp. 734-740.

[8] Jabbari, M.Y., Marston, K.C., Eckert, E.R.G., and Goldstein, R.J., 1996, "Film Cooling of the Gas Turbine Endwall by Discrete-Hole Injection," ASME J. Turbomachinery, **118**, pp. 278-284.

[9] Friedrichs, S., Hodson, H.P., and Dawes, W.N., 1996, "Distribution of Film-Cooling Effectiveness on a Turbine Endwall Measured Using the Ammonia and Diazo Technique," ASME J. Turbomachinery, **118**, pp. 613-621.

[10] Friedrichs, S., Hodson, H.P., and Dawes, W.N., 1997, "Aerodynamic Aspects of Endwall Film Cooling," ASME J. Turbomachinery, **119**, pp. 786-793.

[11] Friedrichs, S., Hodson, H.P., and Dawes, W.N., 1998, "The Design of an Improved Endwall Film Cooling Configuration," ASME Paper No. 98-GT-483.

[12] Blair, M.F., 1974, "An Experimental Study of Heat Transfer and Film Cooling on Large-Scale Turbine Endwall," ASME J. Heat Transfer, **96**, pp. 524-529.

[13] Granser, D., and Schulenberg, T., 1990, "Prediction and Measurement of Film Cooling Effectiveness for a First-Stage Turbine Vane Shroud," ASME Paper No. 90-GT-95.

[14] Roy, R.P., Squires, K.D., Gerendas, M., Song, S., Howe, W.J., and Ansari, A., 2000, “Flow and Heat Transfer at the Hub Endwall of Inlet Vane Passages – Experiments and Simulations,” ASME Paper No. 2000-GT-198.

[15] Burd, S.W., Satterness, C.J., and Simon, T.J., 2000, “Effects of Slot Bleed Injection over a Contoured End Wall on Nozzle Guide Vane Cooling Performance: Part II – Thermal Measurements,” ASME Paper No. 2000-GT-200.

[16] Oke, R., Simon, T., Shih, T., Zhu, B., Lin, Y.L., and Chyu, M., 2001, “Measurements Over a Film-Cooled Contoured Endwall with Various Coolant Injection Rates,” ASME Paper No. 2001- GT-0140.

[17] Oke, R.A., and Simon, T.W., 2002, “Film Cooling Experiments with Flow Introduced Upstream of a First Stage Nozzle Guide Vane through Slots of Various Geometries,” ASME Paper No. GT-2002-30169.

[18] Zhang, L.J., and Jaiswal, R.S., 2001, “Turbine Nozzle Endwall Film Cooling Study Using Pressure-Sensitive Paint,” ASME J. Turbomachinery, **123**, pp. 730-735.

[19] Zhang, L.J., and Moon, H.K., 2003, “Turbine Nozzle Endwall Inlet Film Cooling – The Effect of a Backward Facing Step,” ASME Paper No. GT2003-38319.

[20] Wright, L.M., Blake, S., Rhee, D. H., and Han, J.C., 2007, “Effect of Upstream Wake with Vortex on Turbine Blade Platform Film Cooling with Simulated Stator-Rotor Purge Flow,” ASME Paper No. GT2007-27092.

[21] Gao, Z., Narzary, D., Mhetras, S., and Han, J.C., 2007, “Upstream Vortex Effect on Turbine Blade Platform Film Cooling with Typical Stator-Rotor Purge Flow,” ASME Paper No. IMECE2007-41717.

[22] Suryanarayanan, A., Ozturk, B., Schobeiri, M. T., and Han, J. C., 2007, “Film Cooling Effectiveness on a Rotating Turbine Platform Using Pressure Sensitive Paint Technique,” ASME Paper No. GT2007-27122.

[23] Nicklas, M., 2001, “Film-Cooled Turbine Endwall in a Transonic Flow Field: Part II – Heat Transfer and Film Cooling Effectiveness,” ASME J. Turbomachinery, **123**, pp. 720-729.

[24] Wright, L.M., Gao, Z., Yang, H., and Han, J.C., 2006, “Film Cooling Effectiveness Distribution on a Gas Turbine Blade Platform with Inclined Slot Leakage and Discrete Film Hole Flows,” ASME Paper No. GT2006-90375.

[25] Gao, Z., Narzary, D., and Han, J.C., 2008, “Turbine Blade Platform Film-Cooling with Typical Stator-Rotor Purge Flow and Discrete-Hole Film Cooling,” ASME Paper No. GT2008-50286.

[26] Suryanarayanan, A., Mhetras, S.P., Schobeiri, M.T., and Han, J.C., 2006, "Film Cooling Effectiveness on a Rotating Blade Platform," ASME Paper No. GT2006-90034

[27] Pederson, D. R., Eckert, E. R. G., and Goldstein, R.J., 1988, "Film Cooling with Large Density Differences between the Mainstream and the Secondary Fluid Measued by the Heat-Mass Transfer Analogy," ASME Journal of Heat Transfer, **99**, pp. 620-627.

[28] Sinha, A. K., Bogard, D. G., and Crawford, M. E., 1991, "Film Cooling Effectiveness Downstream of a Single Row of Holes with Variable Density Ratio," ASME J. Turbomachinery, **113**, pp. 442-449.

[29] Ethridge, M. I., Cutbirth, J. M., and Bogard, D. G., 2001, "Scaling of Performance for Varying Density Ratio Coolants on an Airfoil with Strong Curvature and Pressure Gradient Effects," ASME J. Turbomachinery, **123**, pp. 231-237.

[30] Ekkad, S. V., Mehendale, A. B., Dr. Han, J.C., and Lee, C. P., 1997, "Combined Effect of Grid Turbulence and Unsteady Wake on Film Effectiveness and Heat Transfer Coefficient of a Gas Turbine Blade with Air and CO_2 Film Injection," ASME J. Turbomachinery, **119**, pp. 594-600.

[31] Kadotani, K., and Goldstein, R.J., 1979, "On the Nature of Jets Entering a Turbulent Flow Part A–Jet-Mainstream Interaction," ASME J. Turbomachinery, **101**, pp. 459-465.

[32] Jumper, G. W., Elrod, W. C., and Rivir, R.B., 1991, "Film Cooling Effectiveness in High-Turbulence Flow," ASME J. Turbomachinery, **113**, pp. 479-483.

[33] Bons, J. P., MacArthur, C. D., and Rivir, R.B., 1996, "The Effect of High Freestream Turbulence on Film Cooling Effectiveness," ASME J. Turbomachinery, **118**, pp. 814-825.

[34] Schmidt, D. L., and Bogard, D. G., 1996, "Effects of Freestream Turbulence and Surface Roughness on Film Cooling," ASME Paper No. , 96-GT-462.

[35] Burd, S. W., Kaszeta, R. W., Simon, T. W., 1998, "Measurements in Film Cooling Flows: Hole L/D and Turbulence Intensity Effects," ASME J. Turbomachinery, **120**, pp. 791-798.

[36] Saumweber, C., Kaszeta, Achulz, A., and Wittig, S., 2003, "Free-stream Turbulence Effects on Film Cooling with Shaped Holes," ASME J. Turbomachinery, **125**, pp. 65-73.

[37] Goldstein, R. J., Eckert, E. R. G., and Burggraf, F., 1974, ''Effects of Hole Geometry and Density on Three- Dimensional Film Cooling,'' Int. J. Heat Mass Transfer, **17**, pp. 595–607.

[38] Thole, K., Gritsch, M., Schulz, A., and Wittig, S., 1996, ''Flowfield Measurements for Film Cooling Holes With Expanded Exits,'' IGTI Turbo Expo, Birmingham, UK, Paper 96-GT-174.

[39] Gritsch, M., Schulz, A., and Wittig, S., 1997, ''Adiabatic Wall Effectiveness Measurements of Film-Cooling Holes With Expanded Exits,'' ASME Paper No. 97-GT-164.

[40] Yu, Y., Yen, C.-H., Shih, T. I.-P., Chyu, M. K., and Gogineni, S., 1999, ‘‘Film Cooling Effectiveness and Heat Transfer Coefficient Distributions around Diffusion Shaped Holes,’’ ASME Paper No. 99-GT-34.

[41] Schmidt, D. L., Sen, B., and Bogard, D. G., 1994, ‘‘Film Cooling with Compound Angle Holes: Adiabatic Effectiveness,’’ ASME Paper No. 94-GT-312.

[42] Dittmar, J., Schulz, A., and Wittig, S., 2002, ‘‘Assessment of Various Film Cooling Configurations Including Shaped and Compound Angle Holes Based on Large Scale Experiments,’’ ASME Paper No.GT-2002-30176.

[43] Chen, P. H., Hung, M. S., and Ding, P. P., 2001, ‘‘Film Cooling Performance on Curved Walls with Compound Angle Hole Configuration,’’ Ann. N.Y. Acad. Sci., **934**, pp. 353–360.

[44] Teng, S., and Han, J.C., “Effect of Film-Hole Shape on Turbine-Blade Film-Cooling Performance,” Journal of Thermophysics and Heat Transfer, **15(3)**, pp. 257-265.

[45] Mhetras, S., Narzary, D., Gao, Z., and Han, J.C., 2006, “Effect of a Cutback Squealer and Cavity Depth on Film-Cooling Effectiveness on a Gas Turbine Blade Tip,” AIAA Paper No. AIAA-2006-3404.

[46] Garg, V. K., 2000, “Heat Transfer on a Film-Cooled Rotating Blade,” International Journal of Heat and Fluid Flow, **21**, pp. 134-145.

[47] Teng, S., Sohn, D.K., and Han, J.C., 2000, “Unsteady Wake Effect on Film Temperature and Effectiveness Distributions for a Gas Turbine Blade,” ASME J. of Turbomachinery, **122**, pp. 340-347.

[48] Ou, S., Han, J. C., Mehendale, A. G., and Lee, C. P., 1994, ‘‘Unsteady Wake over a Linear Turbine Blade Cascade with Air and CO2 Film Injection: Part I—Effect on Heat Transfer Coefficients,’’ ASME J. Turbomachinery, **116**, pp. 721–729.

[49] Mehendale, A. B., Han, J. C., Ou, S., and Lee, C. P., 1994, ‘‘Unsteady Wake over a Linear Turbine Blade Cascade with Air and CO2 Film Injection: Part II-Effect on Film Effectiveness and Heat Transfer Distributions,’’ ASME J. Turbomachinery, **116**, pp. 730–737.

[50] Du, H., Ekkad, S. V., and Han, J. C., 1999, ‘‘Effect of Unsteady Wake with Trailing Edge Ejection on Film Cooling Performance for a Gas Turbine Blade,’’ ASME J. Turbomachinery, **121**, pp. 448–455.

[51] Rigby, M. J., Johnson, A. B., and Oldfield, M. L. G., 1990, ‘‘Gas Turbine Rotor Blade Film Cooling with and without Simulated NGV Shock Waves and Wakes,’’ ASME Paper No. 90-GT-78.

[52] Heidmann, J.D, Lucci, B.L., and Reshotko, E., 2001, "An Experimental Study of the Effect of Wake Passing on Turbine Blade Film Cooling," ASME J. of Turbomachinery, **123**, pp. 214-221.

[53] Mhetras, S., and Han, J.C., 2006, "Effect of Unsteady Wake on Full Coverage Film-Cooling Effectiveness for a Gas Turbine Blade," AIAA Paper No. AIAA-2006-3404

[54] Han, J.C., Dutta, S., and Ekkad, S. V., 2001, *Gas Turbine Heat Transfer and Cooling Technology*, Taylor & Francis, New York, 2001, Chapter 6.

[55] Wright, L.M., Gao, Z., Varvel, T.A., and Han, J.C., 2005, "Assessment of Steady State PSP, TSP and IR Measurement Techniques for Flat Plate Film Cooling," ASME HT-2005-72363.

[56] Gao, Z., Wright, L.M., and Han, J.C., 2005, "Assessment of Steady State PSP and Transient IR Measurement Techniques for Leading Edge Film Cooling," ASME Paper No. IMECE-2005-80146.

[57] Wright, L. M., Gao, Z., Yang, H., and Han, J.C., 2006, "Film Cooling Effectiveness Distribution on a Gas Turbine Blade Platform with Inclined Slot Leakage and Discrete Film Hole Flows," ASME Paper No. GT2006- 90375.

[58] Ahn J., Mhetras S.P., and J.C. Han, 2004, "Film-Cooling Effectiveness on a Gas Turbine Blade Tip," ASME Paper No. GT-2004-53249.

[59] McLachlan, B., and Bell, J., 1995, "Pressure-Sensitive Paint in Aerodynamic Testing," Exp. Therm. Fluid Sci., **10**, pp. 470–485.

[60] Coleman, H.W., and Steele, W.G., 1989, *Experimentation and Uncertainty Analysis for Engineers*, John Wiley & Sons, New York, 1989, Chaps. 3, 4.

[61] Langston, L.S., 1980, "Crossflows in a Turbine Cascade Passage." ASME Journal of Engineering for Power, **102**, pp. 866-874.

[62] Wang, H., Olson, S.J., Goldstein, R.J., and Eckert, E.R.G., 1997, "Flow Visualization in a Linear Turbine Cascade of High Performance Turbine Blades." ASME J. of Turbomachinery, **119**, pp. 36-42.

[63] McLachlan, B., and Bell, J., 1995, "Pressure-Sensitive Paint in Aerodynamic Testing," Exp. Therm. Fluid Sci., **10**, pp. 470–485.

APPENDIX A

PRESSURE SENSITIVE PAINT

PRESSURE SENSITIVE PAINT TECHNIQUE

PSP is a photo-luminescent material that emits light when excited, with the emitted light intensity inversely proportional to the partial pressure of oxygen. This emitted light intensity was recorded using a CCD camera. Details of using PSP for pressure measurements are given in McLachlan and Bell [63]. The image intensity (I) recorded in the presence of mainstream air and coolant (wind-on condition) was normalized with a reference image intensity (I_{ref}) taken under no-flow condition (wind-off condition). Background noise in the camera was removed by subtracting both these image intensities with the image intensity (I_{blk}) obtained under no-flow condition and without light excitation. The resulting intensity ratio was converted to pressure ratio using a pre-determined calibration curve and expressed as:

$$\frac{\mathrm{I_{ref}} - \mathrm{I_{blk}}}{\mathrm{I} - \mathrm{I_{blk}}} = \mathrm{f}\left(\frac{\left(\mathrm{P_{O_2}}\right)_{\mathrm{air}}}{\left(\mathrm{P_{O_2}}\right)_{\mathrm{ref}}}\right) = \mathrm{f}\left(\mathrm{P_{ratio}}\right) \tag{A1}$$

where I denotes the intensity obtained for each pixel and f ($\mathrm{P_{ratio}}$) is the relationship between intensity ratio and pressure ratio obtained after calibration.

Calibration of PSP system was performed at several known pressures varying from 0 to 1.8atm. The calibration curves are shown in Figs. A1(a) and A1(b). The same optical setup that was used during experiments was chosen for calibration. PSP is sensitive to temperature as well with higher temperatures resulting in lower light emission. The paint was therefore calibrated at different temperatures. It was however observed that if the emitted light intensity (I) recorded at a certain temperature was normalized with the reference image intensity (I_{ref}) taken at the same temperature (equation 3), the temperature sensitivity could be minimized to a great extent. Hence, during experiments, the reference (I_{ref}) and black (I_{blk}) images were acquired immediately after stopping the mainstream flow when the temperature of the blade surface did not change appreciably from the wind-on case.

To obtain film cooling effectiveness, air and nitrogen were used alternately as coolant. Nitrogen which has nearly the same molecular weight as that of air displaces the oxygen molecules on the surface causing a change in the emitted light intensity from PSP. By noting the difference in partial pressure between the air and nitrogen injection cases, the film cooling effectiveness was determined using the following equation.

$$\eta = \frac{C_{mix} - C_{air}}{C_{N_2} - C_{air}} = \frac{C_{air} - C_{mix}}{C_{air}} = \frac{(P_{O_2})_{air} - (P_{O_2})_{mix}}{(P_{O_2})_{air}} \tag{A2}$$

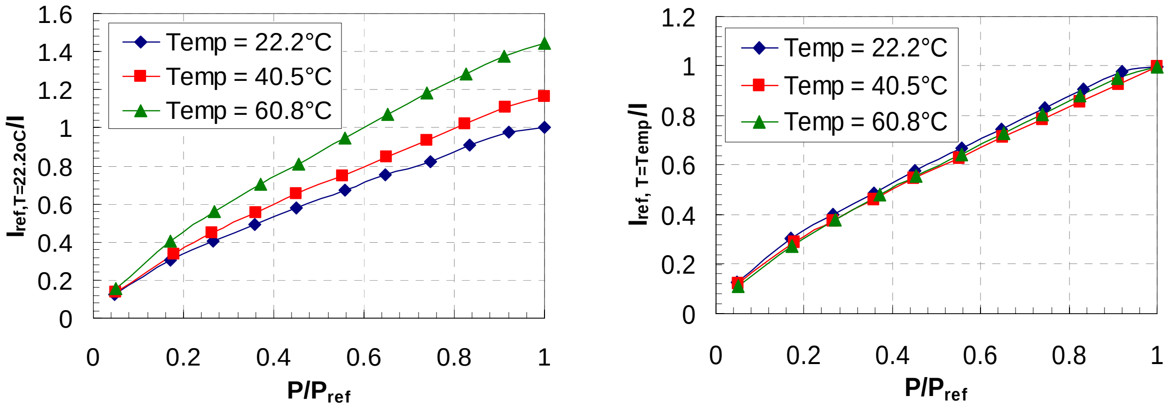

(a) (b)

Fig. A1(a) PSP calibration at single reference temperature (b) PSP calibration at corresponding reference temperature

where C_{air}, C_{mix} and C_{N2} are the oxygen concentrations of mainstream air, air/nitrogen mixture and nitrogen on the test surface, respectively. The definition of film effectiveness as given in Eq. (2) is derived based on the heat-mass transfer analogy with the corresponding equation in terms of temperature being

$$\eta = \frac{T_{mix} - T_m}{T_c - T_m} \tag{A3}$$

The accuracy of the PSP technique for measuring film-cooling effectiveness has been compared by Wright et al. [55] on a flat plate with compound angle ejection holes using steady-state Infra-Red (IR) technique and steady-state Temperature Sensitive Paint (TSP) technique. Results were obtained for a range of blowing ratios and showed an agreement within 15% of each other. Larger uncertainties for heat transfer techniques such as IR and TSP methods were due to lateral heat conduction in the flat plate as corrections for heat conduction were not included in the presented results.

APPENDIX B

TEMPERATURE SENSITIVE PAINT

TEMPERATURE SENSITIVE PAINT TECHNIQUE

In this technique, the test surface is sprayed with a layer of special paint. This paint is composed of luminescent molecules and a polymer binder, both dissolved in a solvent. The basis of the TSP method is the sensitivity of the luminophors to temperature. A light of proper wavelength is used to excite the luminophors. The luminophors return to their ground state by emitting luminescent light of longer wavelength through a process called fluorescence. By using appropriate filters for excitation and emission, the emitted light intensity can be captured by a photo-detector. As the temperature of the luminescent molecules increase, the molecules return to their ground state by a radiationless process known as thermal quenching, rather than fluorescence. As such, the emission intensity from molecules at elevated temperatures is lower than the intensity at relatively lower temperatures.

In practical applications, the paint layer may have non-uniform illumination, paint thickness, and luminophor concentration. In order to eliminate these spatial variations, TSP calibrations are based on a ratio between the luminescent intensity of the paint at an unknown test condition (wind-on) and the luminescent intensity of the paint at a known test condition (wind-off). Further, a ‘black image’ to eliminate background noise from the optical components is recorded and subtracted from these two intensities. The final calibration relation between the luminescent intensity and temperature is written as:

$$\frac{\mathrm{I}(\mathrm{T})-\mathrm{I}_\mathrm{b}}{\mathrm{I}(\mathrm{T})_\mathrm{ref}-\mathrm{I}_\mathrm{b}}=\mathrm{f}(\mathrm{T}) \tag{B1}$$

For calibration, a small block of copper, with a thin foil heater attached on one side and a paint of TSP on the other was used. The same batch of paint, illumination source, camera, and data acquisition system, which were later used for the experiments, were used for calibration. A T-type thermocouple was mounted on the TSP coated side to record the temperature. The copper block was heated from room temperature up to 344K in gradual steps. At each step, the emission intensity was recorded and finally a relationship between the intensity and temperature was established. Figure B.1 shows the calibration curve developed for this TSP with 323K used as the reference temperature.

The film-cooling effectiveness is subsequently computed using the following equation:

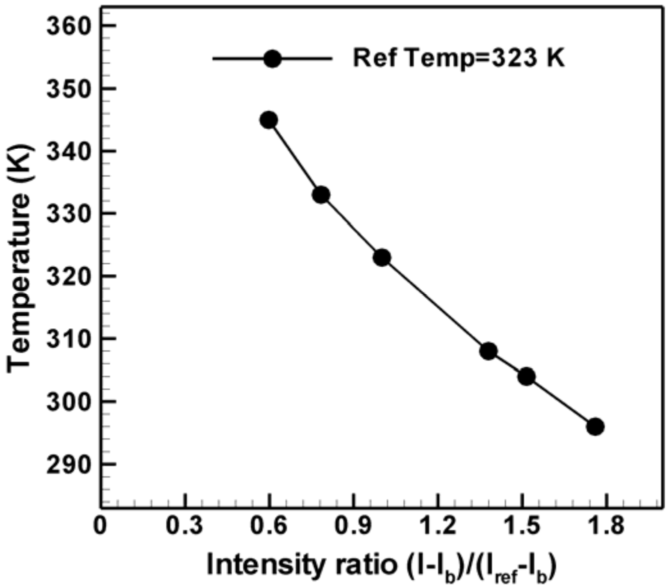

Fig. B.1 TSP calibration curve

$$\eta = \frac{T_{mix} - T_{adia}}{T_c - T_{adia}} \tag{B2}$$

The platform surface temperature recorded with both coolant and mainstream supply is herein referred to as T_{mix}. The surface temperature recorded with mainstream flow only, but no coolant, is referred to as T_{adia}. T_{adia} was used in the equation in place of the more common, $T_{\infty,}$ to eliminate surface temperature gradients caused by aerodynamic heating. Except for one case, all measurements were made when mainstream and coolant reached steady-state temperatures of 333K and 293K, respectively. The experiment with the low turbulence intensity was run with mainstream temperature of 313K and coolant temperature of 288K. As the mainstream temperature was high, the cascade - with the blade and the platform made from soft SLA material and the shroud made from plexiglass - could not be operated for a long duration of time. For this reason, T_{mix} and T_{adia} were run in two separate stages. Care was taken such that the data for the two tests were recorded at exactly the same mainstream inlet temperature.

VITA

Diganta Prakash Narzary received his B.Tech. specializing in Mechanical Engineering from the Indian Institute of Technology, Mumbai, India in 2002. He received his M.S. degree from Arizona State University in August 2005. He entered the Ph.D. program in the Department of Mechanical Engineering at Texas A&M University in August 2005 and received his Ph.D. degree in August 2009.

Diganta may be reached at EPB 100, Mechanical Engineering Dept., Texas A&M University, College Station 77843-3123. His email address is: diganta.narzary@yahoo.com